CHARACTERIZATION AND THERMAL MODELING OF LASER FORMED TI-6AL-4V

by

Shawn M. Kelly

Thesis submitted to the Faculty of the
Virginia Polytechnic Institute and State University
in partial fulfillment of the requirements for the degree of

MASTER OF SCIENCE
in
Materials Science and Engineering

Committee:
Professor Stephen L. Kampe, Chairman
Professor Alex O. Aning
Professor William T. Reynolds, Jr.

9 May 2002
Blacksburg, Virginia

Characterization and Thermal Modeling of Laser Formed Ti-6Al-4V

Shawn M. Kelly

(ABSTRACT)

The current work focuses on three aspects of laser formed Ti-6Al-4V: an evaluation of the as-deposited and heat treated macro and microstructures and preliminary results obtained from a model developed to calculate the temperature profile resultant of the laser forming process. A "solution treat and age" heat treatment with a variable cooling rate was performed on the Laser Formed Ti-6Al-4V single line builds. Increasing the cooling rate decreases the acicular α grain size in the basketweave Widmanstätten α plus untransformed β microstructure. Distinct features of the as-deposited macrostructure include: large columnar prior-β grains that have grown epitaxially through multiple deposited layers; a well defined heat affected zone in the substrate; and the presence of "layer bands," a macroscopic banding present at the top of every layer except for the last three layers to be deposited. The nominal microstructure between the layer bands consists of acicular basketweave Widmanstätten α outlined in untransformed β. The α grain width is smaller just above a layer band and larger just below a layer band. The microstructure of the layer band consists of larger colonies of acicular α outlined in untransformed β. The gradient in the α grain size and presence of the layer band is due to thermal cycling as opposed to segregation effects which were ruled out using quantitative compositional analyses. Through analysis of the microstructural results the gradient in the nominal microstructure and formation of the layer band in layer *n* was caused by the deposition of layer *n+2*, and *n+3*, respectively.

A thermal model has been developed to assist in the prediction and interpretation of the as-processed microstructure. The model is used to explain that the microstructural evolution of the layer bands and gradient microstructure in layer *n* is due to the deposition of layer *n+2*. The difference in the two analyses of microstructural evolution based on microstructural observations and thermal model results are due to differences in the parameter sets used to build and model the deposit.

Acknowledgements

I would like to thank my advisor, Dr. Stephen L. Kampe for his advice, guidance, and assistance in helping me complete this thesis. I would also like to thank Dr. Alex Aning and Dr. Bill Reynolds for serving as committee members and commenting on the thesis. I would also like to acknowledge, Dr. Steven Fishman of ONR, Dr. Kevin Slattery of Boeing, and Dr. Frank Arcella of AeroMet, for providing the opportunity to work on this project. Funding was provided under ONR contracts N00014-98-3-0022 and N00014-00-1-0579.

I would like to thank my lab mates, Keith, Ben, Adam, Jen, and Jeff for, at the very least, making the lab environment an interesting place to work and for providing assistance and discussion on various topics. I am indebted to David Berry, whom has saved me countless hours of time repairing equipment through his technical assistance.

I would also like to thank my parents, Tim and Charlene, my brothers, Brian and Stephen, my Grandparents, Nicholas and Madge Notarange, the rest of my family, and my Wife's family for their support and encouragement while I delayed gainful employment for a few years as I pursued my graduate education.

Last, but not least, I am grateful for my wife, Chandale, who has supported, encouraged, and most importantly, has loved me unconditionally during a time of late-night trips to the lab and sleepless nights spent writing my thesis.

Table of Contents

List of Figures

List of Tables

Executive Summary

This thesis examines the Laser Forming of the titanium alloy, Ti-6Al-4V, through microstructural evaluation of the as-deposited material, a heat treatment study, and thermal modeling of the Laser Forming process. The introduction reviews topics pertinent to the experiments and results obtained. First, titanium alloy physical metallurgy is reviewed in order to gain an understanding of possible changes in microstructure that may evolve as a result of the Laser Forming process and the underlying structure property relationships. Second, Rapid Manufacturing will be reviewed with an emphasis on Direct Metal Deposition processes, one of which is the Laser Forming process. Lastly, numerical methods used to develop a thermal model of the Laser Forming process are reviewed.

In Rapid Manufacturing (RM) processes, a CAD file is used to generate laser scan paths (trajectories) for a two dimensional layer and the part is built layer by layer by stepping the focal length of the laser a required layer distance. Laser Forming is a Rapid Manufacturing process developed by AeroMet Corporation to fabricate near-net shape metal parts without molds or dies. The Laser Forming process deposits material at a rate of approximately 4.5 $kg \cdot hr^{-1}$. At these high deposition rates, a near-net shape part is produced that requires some post forming machining; however, the machining requirements are often 50% less than those of forgings. The Laser Forming process is well suited for short production runs, eliminating the need for expensive molds or dies and reducing the time needed to produce a part by 50 to 75%. In addition to building structural components for the aerospace, defense and chemical industries, the additive nature of the Laser Forming process allows for the addition of features such as lugs or extensions to forgings, castings, or extrusions, thereby reducing the complexity of conventional processing operations. Also, damaged components such as tool dies can be repaired using the Laser Forming process.

The research to be presented arose from a need to "qualify" Ti-6Al-4V Laser Formed structural parts for the aerospace industry. As part of this qualification process, a heat treatment study was required. Laser Formed Ti-6Al-4V parts containing 18 layers of material deposited on a rolled and mill-annealed Ti-6Al-4V substrate were fabricated by AeroMet sent to Virginia Tech by Boeing for a heat treatment study. The parts were single line builds and the parameters (laser speed, power, material flow rate, base preheat) used to build the parts were unknown for

proprietary reasons. A solution treat and age heat treatment was performed on the material as follows: (1) a 2-hour solution treatment at 913°C, (2) a furnace-controlled cool down to 315°C at rates ranging from 0.3°C/min to 500°C/min, and (3) a 4-hour aging treatment at 538°C followed by a furnace cool. The heat treated microstructure was observed using optical microscopy to have a basketweave Widmanstätten α morphology where the Burger's oriented α grains are outlined in untransformed β phase. It was determined that increasing the cooling rate resulted in a finer α grain size in the material.

A thorough examination of the as-deposited (pre heat-treated) material was performed in order to compare the effect of heat treatment with the starting microstructure. Interesting macro and microstructural features were observed in the as-deposited material. In the macrostructure, large columnar prior beta grains that have grown across multiple deposited layers, a well-defined heat affected zone in the substrate, and a macroscopic banding that appeared at every deposited layer except for the last three layers to be deposited. The columnar prior beta grains are a result of epitaxial growth from previously deposited material. The substrate heat affected zone is a result of the thermal cycling experienced due to the deposition of multiple layers of material. The presence of the layer band could not be described solely on the basis of macrostructure.

The microstructural features that were observed in the deposit include a nominal microstructure between each layer band consisting of a basketweave Widmanstätten α morphology where a gradient in the acicular α grain size was observed. The layer band consisted of a colony α morphology where several acicular α grains are aligned parallel to one another. It was theorized that the layer band and gradient α morphologies could be a result of segregation in the melt pool or thermal cycling effects. It was also proposed that the layer band could be a result of oxidation occurring during the deposition process. It was determined through quantitative electron microprobe analyses that there was no systematic difference in composition across a layer or across a layer band. Hardness measurements revealed that the layer band was no harder than the surrounding material. Thus it was concluded that segregation and oxidation effects were not the cause of the gradient or layer band morphologies, with the most likely cause for their presence being thermal cycling effects.

An attempt was made to understand the microstructural evolution of the gradient α and layer band morphologies through clues present in the last four layers deposited. It was

determined that the gradient α and layer band morphologies form in layer *n* due to the deposition of layer *n+2*, and layer *n+3*, respectively.

In order to better understand the thermal cycling that occurs as a part is being built a thermal model was developed utilizing a finite difference approximation to a nonlinear transient heat conduction equation. The temperature as a function of position and time were examined in two dimensions, with the plane being perpendicular to the direction of laser motion. Estimated input parameters such as laser speed, dwell time of the laser, and laser superheat, were utilized since the parameter set AeroMet used was unavailable for proprietary reasons. The resulting temperature versus time data illustrated that depending on the dwell time of the laser (energy input to the deposit) excursions into the liquid, liquid+beta, beta, and alpha plus beta phase fields will be experienced. There is also a residual heating that occurring in layer *n* due to the deposition of layers *n+4* and greater. The residual heating will result in aging of any untransformed β in the deposit, leading to coarsening of the α phase, and possible relief of any residual thermal stresses that arise during the deposition process. In examining the temperature versus build height data, the most interesting result obtained was that in different regions of the part heating and cooling are occurring simultaneously as thermal wave produced by the deposition of a new layer propagates through a part.

A theory for microstructural evolution based on thermal model results was proposed. It was concluded that both the layer band and gradient α morphologies form in layer *n* as a result of the deposition of layer *n+2*. This is different than the theory for microstructural evolution based on the microstructural results. The difference is most likely due to the processing parameters used in the thermal model are different than the actual parameters used in the build.

Chapter 1:

Background

Titanium Alloys

In 1790, the element titanium was discovered in the parish of Menaccan, six miles south of Falmouth, in Cornwall, England by the Reverend William Gregor. From this time until 1795, little interest was shown in the black magnetic sand known as menaccanite. In 1795, M.H. Klaproth of Germany, applied the temporary name “titanium” to the new element, stating "Wherefore no name can be found for a new fossil (element) which indicates its peculiar and characteristic properties, in which position I find myself at present, I think it is best to chose such a denomination as means nothing of itself and thus can give no rise to erroneous ideas…I shall borrow the name for this metallic substance from mythology, and in particular from the Titans, the first sons of the earth. I therefore call this metallic genus, titanium[1]."

Titanium is the ninth most abundant element of the earth’s crust, accounting for 0.63% of the total. It is superceded by oxygen, silicon, aluminum, iron, magnesium, calcium, sodium, and potassium. It is found in greater abundance than zinc, copper, and lead, combined. An analysis by Dunnington[2] of many soils throughout the world found that Virginia is home to 1.57% of the total titanium worldwide, with most of the deposits being found in Amherst, Nelson, and Roanoke counties.[3] Titanium has also been discovered in the stars, in interstellar dust, and in meteorites.

The following sections and subsection will look at titanium production, physical metallurgy, alloy classification, general alloy properties, and the microstructural constituents and morphologies observed in titanium alloys.

Production

Though there are several minerals in which the element titanium is found, rutile and ilemnite are the primary starting points for the production of titanium. First, the titanium dioxide (TiO_2) in the ore is mixed with carbon and chlorinated, producing titanium tetrachloride gas, $TiCl_4$. In the Kroll process, $TiCl_4$ is reacted with liquid Mg producing pure titanium and $MgCl_2$. The Hunter process is an alternative method of extracting pure titanium from $TiCl_4$. The energy required to produce a ton of sponge titanium from its ore is 16 times that needed to produce a ton of steel, 3.7 times that needed for ferrochrome, 1.7 times that needed for aluminum production, and slightly greater than that needed to produce magnesium.

The first commercial titanium mill products were produced by the Titanium Metals Company of America (TMCA) around 1950. Titanium was introduced to the aerospace industry in the 1950's in response to the need for aircraft materials with a better strength to weight ratio. In addition to the strength to weight ratio, titanium alloys have excellent high temperature resistance to 550° C and excellent corrosion resistance in oxidizing acids and seawater. Thus titanium can be found in a wide range of non-aerospace applications such as hip implants, bicycle frames, hydrogen-storage media, high-current/high field superconductors, condenser tubing for nuclear and fossil-fuel power generation, off-shore oil drilling, desalination plants, pulp and paper industries, and the chemical and petrochemical industries. This diversified industry base has helped the titanium industry weather the cyclical nature of the defense industry and allowed production to steadily increase at a rate of 8% per year.

Physical Metallurgy

The physical metallurgy of titanium alloys has been reviewed in several sources.[4, 5, 6, 7, 8, 9] This section serves to highlight important aspects of titanium alloy physical metallurgy including, the basis for and characteristics of different titanium alloy classes, phase transformations and their respective morphologies, and lastly, structure-property relationships existent in titanium alloys.

Upon heating, elemental titanium undergoes an allotropic phase transformation from the hexagonal closed packed (HCP) α phase to the body centered cubic (BCC) β phase at 882.5°C (β transus) and melts at 1668°C. Upon alloying, the β transus will either be raised or lowered, depending on the alloying element. A two phase α+β region will also form. Alloying elements that produce little change in, or raise the β transus, stabilize the α phase. While those elements that lower the β transus, stabilize the β phase. Alpha-stabilizing elements tend to be simple metals such as Al, Ga, Ge, and Sn (substitutional) and O, C, N (interstitial). Transition, refractory, and noble metals are β-stabilizers.[10, 11] Tin and zirconium have extensive solid solubility in titanium; however, they do not effectively stabilize the α or β phase. The electronic and thermodynamic theories for α and β phase stabilization have been summarized by Collings.[12] Binary α and β stabilized systems can be further subcategorized into α-peritectic, α-peritectoid, β-isomorphous, and β-eutectoid systems by their phase diagrams as shown in Figure 1. Figure 1 also serves to summarize the various α and β-stabilizing elements.

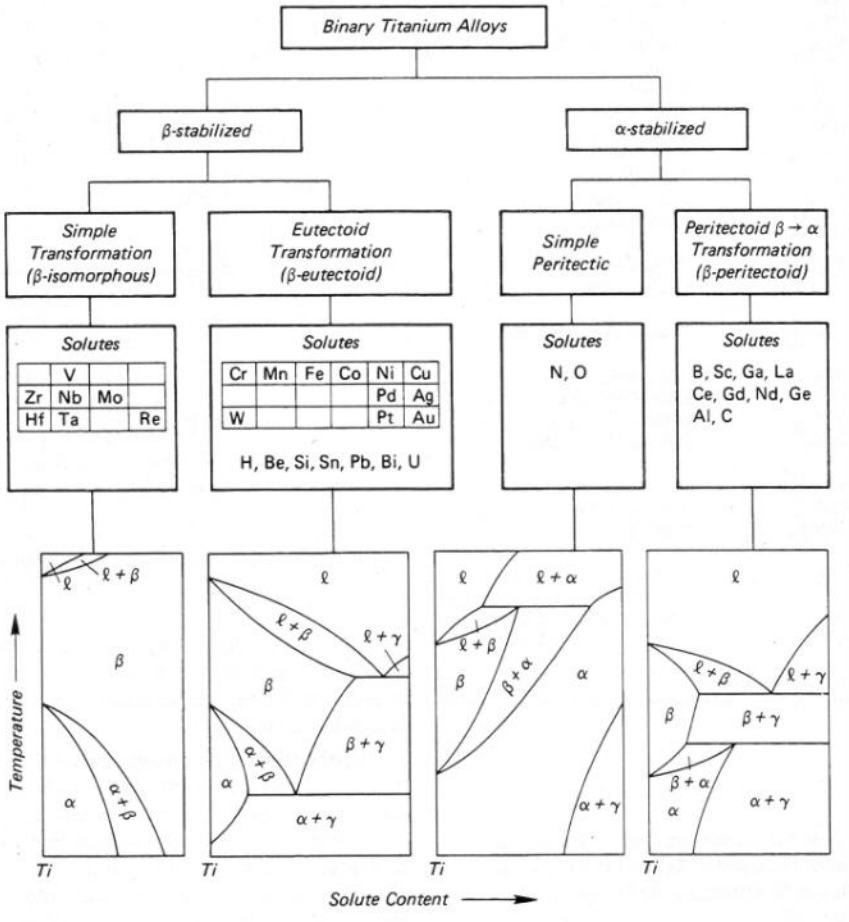

Figure 1: Classification scheme for binary titanium alloy phase diagrams. α and β are HCP and BCC solid-solution alloys and γ represents an intermetallic compound. From [13], after [14].

Titanium Alloy Classification

Technical[†] titanium alloys are generally composed of mixtures of α and β stabilizing elements, the combination of which may produce α, α+β, and β equilibrium phases at room temperature. Thus, the designation of titanium alloys can fall into one of three broad categories: α, α+β, and β alloys. In some cases the alloy composition may lie near the α↔α+β or β↔α+β transi at room temperature, leading to the sub-classification "near-α" and "near-β" alloys, respectively. Flower[15] gives an excellent summary of these classification schemes, where his important points have been repeated below. The classification of some technical titanium alloys based on their β-stabilizer content is shown schematically on the pseudobinary β-isomorphous

[†] Ternary and higher order alloy systems

phase diagram in Figure 2. Figure 3 shows a similar phase diagram to Figure 2 with a more realistic martensite start and finish curve (M_s / M_f) and α+β phase field width. The martensitic transformation will be discussed further in later sections. Table I lists several titanium alloys, their specific class, and typical applications.

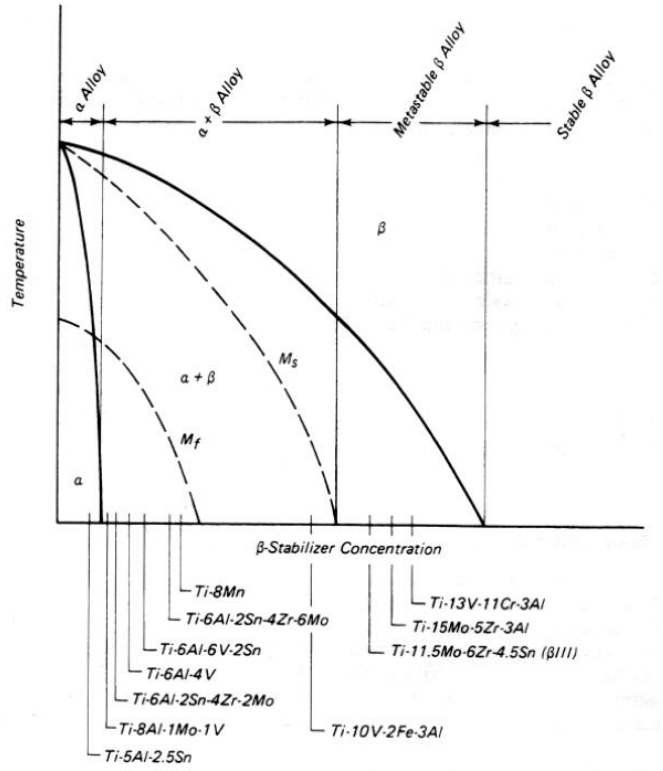

Figure 2: Composition and classification of U.S. technical titanium alloys mapped onto a pseudobinary isomorphous phase diagram. From [16], after [17].

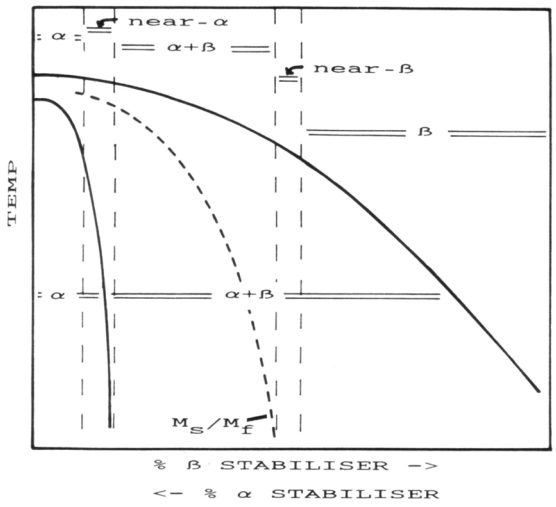

Figure 3: Psuedobinary isomorphous phase diagram showing a more realistic martensite start/finish **(M_s/M_f)** curve and width of the α+β phase field. From [15].

α Alloys

Alpha titanium alloys have a composition such that upon cooling at any rate from above the α ↔ α+β transus to room temperature, only the HCP α phase is present. Satisfactory strength, notch toughness, creep resistance at high temperatures and weldability are characteristic of α titanium alloys such as Ti-5Al-2.5Sn. In addition α titanium alloys are not heat-treatable and do not exhibit a ductile to brittle transition, with the latter making them suitable choices for cryogenic applications. Aluminum is the most important α alloying addition as it solid solution strengthens titanium and reduces the alloy density.

Commercially Pure (CP) titanium is often considered an α-alloy due to the presence of interstitial impurities O, C, N, and H and the substitutional impurity, Fe. CP Ti is lower in strength, but offers a higher level of corrosion resistance at a lower cost than other titanium alloys. Oxygen is always present to some extent in titanium sponge; however, the oxygen content as well as nitrogen and to a lesser extent, C, can be adjusted to control strength, thus, different grades of CP Ti can be thought of as "alloys."[19] Small additions of the interstitial elements O, N, and C, increase strength while decreasing the ductility and toughness of CP Ti. Collings[20] has explained the interstitial strengthening mechanism of O, C, and N to be a result of covalent bonding between the interstitial atom and matrix. Hydrogen is undesirable as it embrittles CP Ti. Extra-Low-Interstitial (ELI) grades of CP Ti are available when toughness becomes important as in cryogenic applications.

Table I: Classes, Compositions, and Applications for Selected Titanium Alloys [a]

Class	Composition (wt.%)	Application
α	CP Grade 2 (99.2% Ti)	Airframes, aircraft Engines, marine and chemical environments
	Ti-5Al-2.5Sn (IMI 317, VT-5-1)	Aircraft compressor blades; steam turbine blades; ELI version for cryogenic service
Near-α	Ti-8Al-1Mo-1V	Airframe and jet engine parts; good creep, toughness, and weldability
	Ti-6Al-2Sn-4Zr-2Mo	Parts and cases for jet engines; airframe skin
α+β	Ti-3Al-2.5V	Hydraulic tubing, biomedical, sports equipment (bicycle frames, golf club shafts, etc.)
	Ti-6Al-4V (IMI 318, VT-6)	Aircraft gas turbine disks and blades, airframe structural forgings and fasteners, pressure vessels.
	Ti-6Al-6V-2Sn	Same as Ti-6Al-4V
Near-β	Ti-10V-2Fe-3Al	Thick bar, plate and forged sections
β	Ti-13V-11Cr-3Al	Fasteners, foils for honeycomb panels
	Ti-3Al-8V-6Cr-4Mo-4Zr (Beta C)	Fasteners, springs, torsion bars, foils for honeycomb panels

[a] From References 6 and 18

Near-α Alloys

Near-α alloys differ from α alloys in that they contain small concentrations of β stabilizing elements as a result of alloying additions or impurities, thus they are able to retain small amounts of metastable β phase at room temperature. They exhibit mechanical properties similar to α alloys (creep resistance at elevated temperatures, weldability) and microstructural morphologies similar to α+β alloys (α outlined in retained β).

α + β Alloys

α+β alloys contain sufficient amounts of β stabilizing elements allowing the β phase to be present at room temperature, resulting in an α+β microstructure that may be strengthened by heat treatment. The β phase may be present in quantities ranging from 10 to 50% at room temperature. Since the addition of β stabilizing elements broadens and extends the α+β phase field to room temperature, a variety of microstructures may be produced by varying processing conditions. α+β alloys have the ability to form martensite under sufficiently fast cooling rates. Flower[15] states that the martensite start and finish curves (M_s ,M_f) are much closer than is often reported (Compare Figure 2 with Figure 3) resulting in a narrow compositional range where the $\beta \rightarrow \alpha^m$ martensitic transformation can take place. Furthermore, local[‡] transformation of the β phase is either completely martensitic, or completely metastable β, not a mixture of both. Microstructure and mechanical properties are highly dependent on both thermal and thermomechanical processing conditions, the effect of which will be discussed for the quintessential titanium alloy Ti-6Al-4V in a subsequent section.

In general, α+β alloys exhibit formability, high room temperature strength, and moderate elevated temperature strength; however, they are not easily through-hardenable and cannot be welded if greater than 20% β phase is present.

Near β Alloys

Near β alloys differ from α+β alloys in that they contain sufficient amounts of β stabilizing elements to suppress the martensitic $\beta \rightarrow \alpha^m$ transformation to below room

[‡] Since cooling rates typically vary in a global sense (entire sample, part), it is possible for the martensitic transformation to take be complete in one location and not in another.

temperature (Figure 2, Figure 3). Also, near-β alloys can be processed in the β field at lower temperatures (~800°C) as compared to α+β alloys (~1000°C). The near-β alloys have the highest strengths of titanium alloys, are easily forged and welded, and exhibit good hardenability and toughness.

β Alloys

β alloys are able to retain the metastable BCC β phase upon cooling to room temperature, and thus have properties inherent to BCC metals such as excellent formability and a ductile-to-brittle transformation. β and near-β alloys exhibit high strength, toughness, and through hardenability, but suffer from low ductility in the high strength condition. Though no commercially available β alloy exists with a thermodynamically stable β phase at room temperature, the amount of β stabilizing elements is large enough to allow the β phase to be present in a weak metastable state, such that decomposition of β to α will not take place with common thermomechanical treatments.[15] An all metastable-β alloy such as Ti-13V-11Cr-3Al can be aged to decompose the metastable β into solute rich (β_2) and solute lean (β_1) phases. The decomposition of the metastable β phase may proceed further by nucleating the α phase at β_2 precipitates, thereby producing an α+β structure.

Titanium Aluminides

Alloying titanium with large amounts, ~10-50at%, of α stabilizers, namely aluminum will lead to precipitation of the intermetallic α_2 (Ti_3Al) and or γ (TiAl). Termed titanium aluminides, these alloys may have lower densities, increased stiffness, creep and oxidation temperatures, and lower ductilities than conventional titanium alloys. Though this class of titanium alloys is has been the subject of much research in the 80's and 90's, it will not be greatly discussed here as it does not conform to the scope of this paper.

Phase Transformations and Morphologies

The purpose of this subsection is to introduce the equilibrium and non-equilibrium phase transformations that occur and there respective morphologies. In particular, the following transformations will be discussed: allotropic β→α, nucleation and growth of α phase, the

martensitic transformation of $\beta \rightarrow \alpha'$ and $\beta \rightarrow \alpha''$, ordering reactions α_2 and γ, decomposition of metastable β phase by formation of athermal and isothermal ω and phase splitting $\beta \rightarrow \beta_{rich} + \beta'$, and lastly the controversial formation of the α/β interfacial phase and Types 1 and 2α. This will serve as a basis to discuss structure property relationships in the next subsection. The information presented below has been primarily been extracted from several review articles on titanium phase transformations, written by the likes of M.K. McQuillan,[21] Blackburn,[22] Williams,[23,24 25] Hammond and Nutting,[9] Collings,[4,5] Murakami,[26] and Welsch and Boyer.[27]

Allotropic $\alpha \leftrightarrow \beta$ Transformation

Pure metals such as iron, titanium, and tin are allotropic, meaning they can have different crystal structures over different temperature ranges. Specifically for pure titanium, the HCP α phase transforms to the BCC β phase at the allotropic transformation temperature of 882.5°C. Allotropy is a result of thermodynamically competing crystal structures. Generally, the phase with the close packed crystal structure (FCC, HCP) is stable below the allotropic transformation temperature, while the stable phase above the allotropic transformation temperature has a more open crystal lattice (BCC). From a thermodynamic standpoint, closed-packed crystal structures have a lower internal energy and consequently, lower enthalpy, due to the tight binding of the atoms in the lattice. Conversely, the more open crystal structure has a higher vibrational entropy. The competition of the free energy for the α and β phase in a metal that exhibits an allotropic transformation is shown in Figure 4. At absolute zero, the entropy term, $-T\Delta S$, in the equation for the change in free energy: $\Delta G = \Delta H - T\Delta S$, is zero by definition. Consequently, the α phase is stable because it has the lower enthalpy and free energy. The lower enthalpy of the α phase continues to dominate as the temperature rises, while the free energy difference between the two phases, ΔG, continues to decrease with increasing temperature. At the allotropic transformation temperature $T_{\alpha \leftrightarrow \beta}$, $\Delta H = T\Delta S$ and $\Delta G = 0$. Above $T_{\alpha \leftrightarrow \beta}$, the β phase becomes stable as a result of the vibrational entropy of the β phase increasing sufficiently to lower the free energy below that of the α phase. Stated differently, the enthalpy of the closed packed phase competes with the entropy of the "loose" packed phase as the temperature rises. When these quantities become equal, provided the low-temperature-stable phase has not melted, the allotropic phase transformation takes place, typically with the closed packed phase transforming to a "loose"

packed phase. Allotropic phase transformations of the closed to "open" packed nature are observed in pure Li, Na, Ca, Sr, Zr, Hf, and Tl.

The allotropic transformation of the β phase to the α phase in pure titanium occurs easily and cannot be suppressed by rapid quenching; therefore, it is widely accepted that the α↔β transformation is a diffusionless shear transformation of the martensitic type or a massive transformation. The athermal martensitic transformation in titanium alloys will be discussed later. First we will concern our discussion with nucleation and growth processes that occur in titanium alloys.

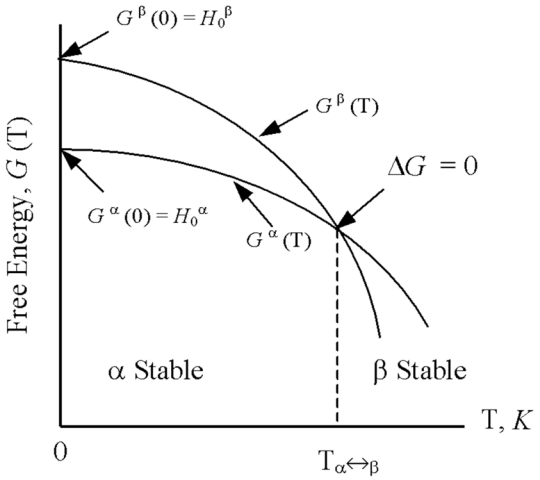

Figure 4: Schematic free energy as a function of temperature curves for illustrating and allotropic phase transformation where α is the low-temperature-stable phase.

Nucleation and Growth of the α Phase

In general, cooling from the β phase field at moderate rates will result in nucleation and growth of the α phase. Alpha that has been formed as a result of cooling from the β phase field is defined[27,28] as *primary alpha* and can have a lamellar, equiaxed, or mixed morphology. *Secondary alpha* or *transformed beta* refers to the local or continuous structures that arise from sub-beta transus (α or α+β phase field) heating, resulting in the nucleation and growth of α from previously retained martensite or metastable β regions. The only way to distinguish these two forms is with knowledge of the prior thermal treatment of the part, i.e., primary and secondary alpha are morphologically and compositionally indifferent.

The α phase nucleates and grows[23,29] such that the basal plane of the α phase, $\{0001\}_{\alpha}$, is parallel to (||) the $\{110\}_{\beta}$ plane of the β phase and the $<\bar{1}11>_{\beta} \parallel <11\bar{2}0>_{\alpha}$. This is known as the Burger's orientation relationship.[30] As a result, the α phase assumes a needle, lath, lamellar, or plate morphology often referred to as *acicular alpha*.* If the alloy contains a sufficient amount of β stabilizers, the α plates will be separated by retained β. The retained β or "β matrix"

* In the current discussion, "α plates" or "α platelets" will refer to acicular α.

outlining the α platelets becomes enriched in β-stabilizing elements as a result of rapid diffusion of these elements ahead of the migrating interface.[9]

The α platelet forms such that *c* axis (<0001> direction) is parallel to the α/β interface and the α/β interfaces are on or close to the $\{10\bar{1}0\}_\alpha$ prismatic planes. Since the Prior Beta Grain (PBG)[**] has six sets of non-parallel $\{110\}_\beta$ planes and each plane has 2 <111> directions, the α platelets are related to the PBG by 1 of 12 Burgers orientation variants.[30] When the nucleating phase forms as needles or plates and exhibits a crystallographic relationship to the matrix, the result is the *Widmanstätten* morphology. Formation of the Widmanstätten α phase in the α+β alloy Ti-6Al-6V is illustrated in Figure 5 using an approximate isopleth for a titanium alloy containing 6 weight percent aluminum.

The Widmanstätten α platelets may be arranged in packets of similarly aligned α platelets called *colonies* (Figure 6a) or aligned in a *basketweave structure* (Figure 6b). A basket-weave structure is indicative of faster cooling rates from above the β transus or an increase in the β stabilizer content. The number of Widmanstätten α platelets appearing in each colony will increase with β solution treatment temperature and time and decrease with the amount of β-stabilizing elements, the amount of β work, and the cooling rate.[31,32] Each colony of α grains behaves as a single crystal or grain since the orientation difference between adjacent α grains is very small.[27,33] Therefore, the colony size is often used to describe mechanical properties such as fatigue life and fatigue crack growth. This structure-property relationship will be discussed further in a later section.

[**] The prior β grain (PBG) can be thought of as the parent β grain.

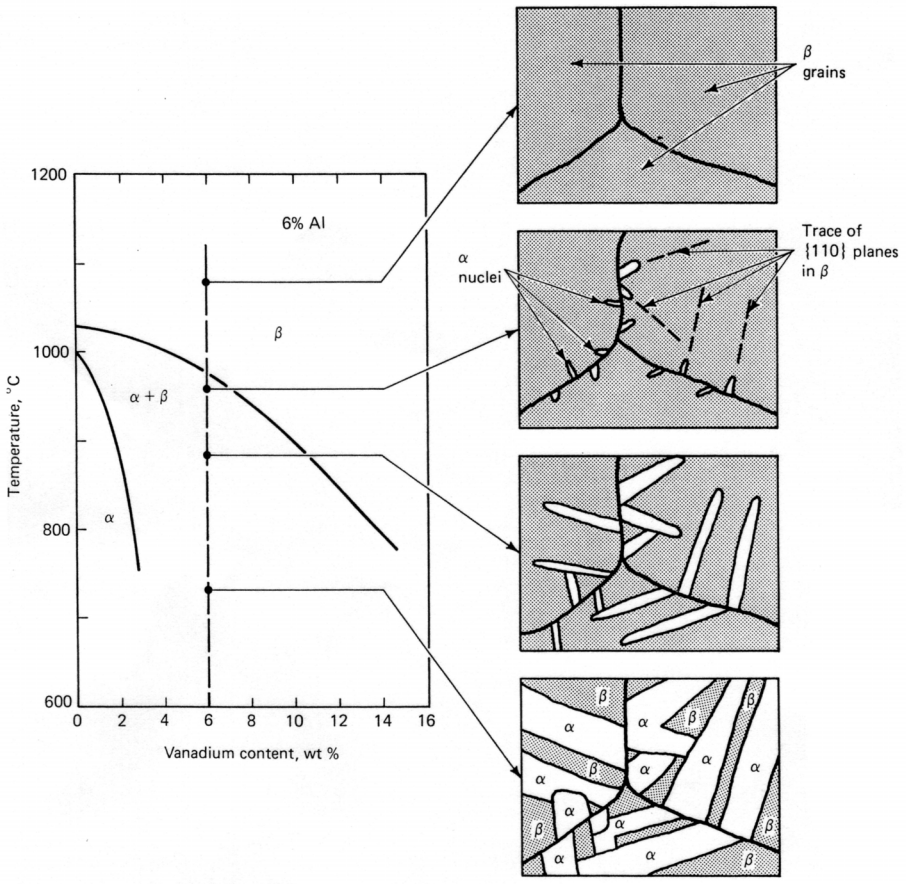

Figure 5: Schematic illustration of Widmanstätten α formation in a Ti-6Al-4V alloy slowly cooled from above the transus using a Ti-6Al isopleth for reference. The final microstructure consists of α plates in a matrix of retained β phase. From [6], p. 364.

If the cooling rate is slow enough, the primary α may also grow along PBG's as shown in Figure 7. This morphology is termed *grain boundary α.* Grain boundary α serves to demarcate PBG's, and, as with the colony size, the PBG size is important determining certain mechanical properties.

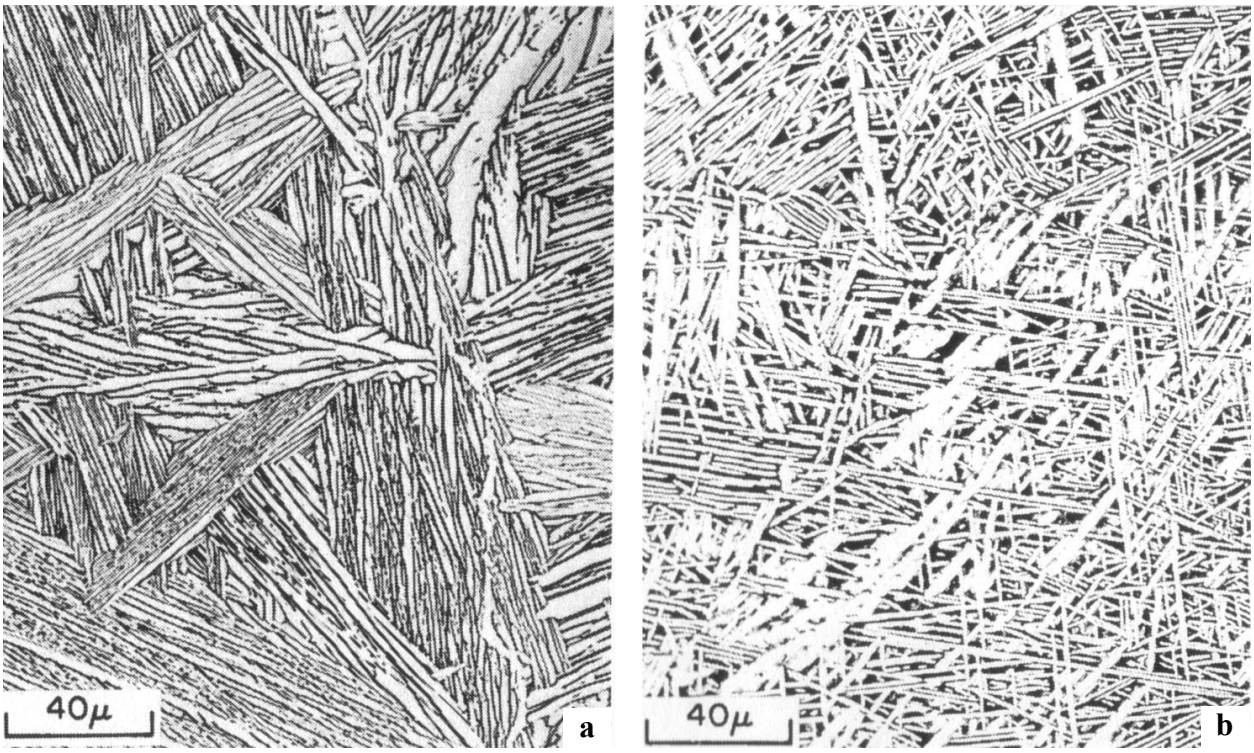

Figure 6: Comparison of Widmanstätten α colonies in a Ti-6Al-4V (a) and a basket-weave Widmanstätten α structure in Ti-6Al-2Sn-4Zr-6Mo (b). Both alloys were β processed. Increasing cooling rate, amount of β stabilizers, amount of β work and decreasing β solution temperature and time will tend to produce the basket-weave morphology. From [**31**], p. 109 (108).

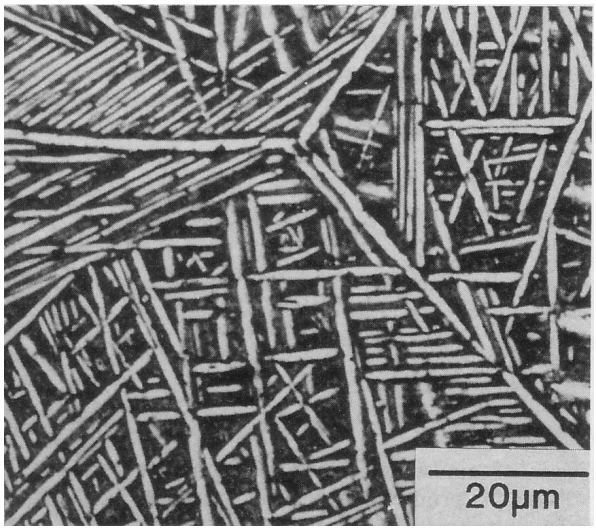

Figure 7: Micrograph of the α+β alloy Ti-4Al-4Mo-2Sn-0.5Si (IMI 550) that was forged above the β transus and furnace cooled to produce a basket-weave Widmanstätten α structure with the Prior Beta Grains (PBG's) outlined in grain boundary α. From [15], p. 1084.

Precipitation of α_2 (Ti_3Al) and γ (TiAl)

Aging titanium with greater than 5-6 wt.% aluminum will produce the coherent long-range-ordered α_2 intermetallic (Ti_3Al), which embrittles Ti-Al alloys. The α_2 phase exhibits the $D0_{19}$ structure[34] – a unit cell composed of four regular HCP cells apparently supported by covalent-like directional bonds connecting the Al and Ti atoms. A partial Ti-Al phase diagram, Figure 8, shows the composition and temperature ranges over which the α_2 phase appears. The α_2 phase may also appear as Ti_3SM, where SM is a "Simple Metal" such as Sn, In, or Ga. In multicomponent alloys of titanium containing aluminum, the following "rule of thumb" is employed to avoid the embrittling effect of excessive α_2:

$$Al^* = Al + \frac{Sn}{3} + \frac{Zr}{6} + 10(0 + C + 2N), \text{ where } Al^*$$

is the aluminum equivalent. From $Al^* \geq 5$, the α_2 phase occurs as fine precipitates that increase in size with an increase in composition and aging temperature and time. Formation of the α_2 phase is similar to the formation of γ' is nickel based superalloys in that they both occur as coherent ordered particles and are sheared by dislocations; however, in titanium alloys, the presence of α_2 is deleterious in that it decreases ductility.[9] Some degree of ductility may be acquired if the α_2 particles coarsen sufficiently to allow for dislocation looping to occur.[35]

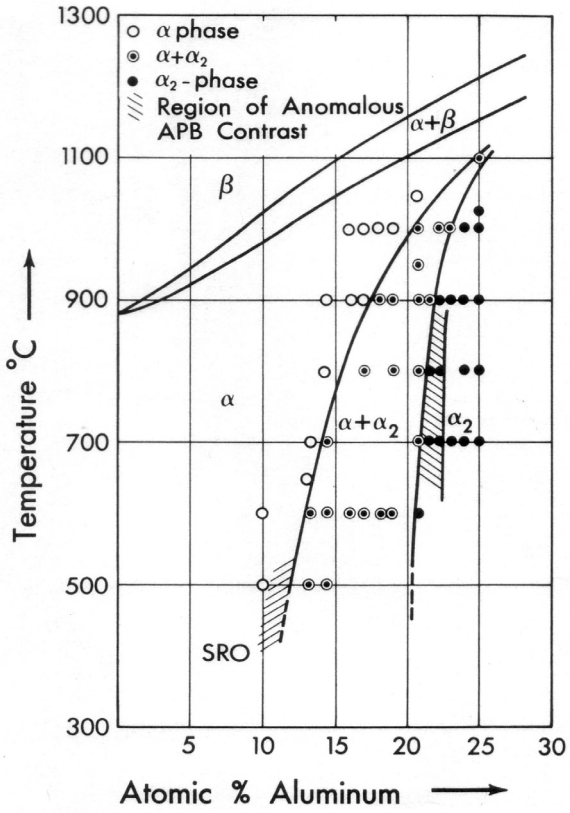

Figure 8: Ti-Al phase diagram for 0 to 25 at.% Al showing the position of the α2 phase field. APB is antiphase domain boundary and SRO is short range order. From Blackburn [34], p.1207.

The ordered stoichiometric γ titanium aluminide (TiAl) phase has the tetragonal $L1_0$ structure. The γ phase Mixtures of α_2 and γ can be obtained upon alloying titanium with ~40 - ~50 at.% aluminum. These alloys are more microstructurally stable than when only α_2 is present, but there is no significant improvement in ductility. This concludes the discussion of

titanium aluminides. For further information, refer to the Proceedings of the 8th World Conference On Titanium, where 25% of the papers dealt with titanium intermetallics.[36]

Martensitic Transformation

Above, it was stated that upon slow to moderate cooling from the β-phase field through the α+β phase field, α will nucleate from the parent β phase producing the Widmanstätten α morphology. Increasing the cooling rate from above a certain temperature (not necessarily above the β transus, but in the α+β phase field), will bring the nucleation and growth processes into competition with diffusionless, martensitic processes. The martensitic transformation begins and ends at compositionally dependent temperatures, termed the martensite start (M_s) and martensite finish (M_f) temperatures, respectively. As shown in Figure 2 and Figure 3, increasing the β stabilizing content will decrease the M_s from near the β transus to well into the α+β phase field.

The martensitic phase transformation in titanium alloys is designated β→α′ or β→α″, depending on whether the product exhibits a HCP or orthorhombic crystal structure. The purely athermal α′ variant is observed in β-isomorphous or β-eutectoid alloys. The α″ variant is observed over certain composition ranges in binary alloys such as Ti-Mo, Ti-Nb and in many commercial alloys such as Ti-6Al-4V. The α″ variant may also form as a result of a stress-induced transformation if the alloy has been quenched into the α+β phase field without intersecting M_s. Face centered orthorhombic (FCO) and face centered cubic (FCC) martensites have also been reported to form in α+β and β alloys.

The morphology of the martensite is composition dependent, ranging from *massive*[*] in pure and lightly alloyed titanium to *acicular* with increasing solute concentration. The morphological dependence on β stabilizer concentration is similar to that discussed above for the Widmanstätten α morphology. The progression from massive martensite to acicular martensite is shown in Figure 9 and Figure 10, respectively.

[*] Also called *packet*, or *lath martensite*

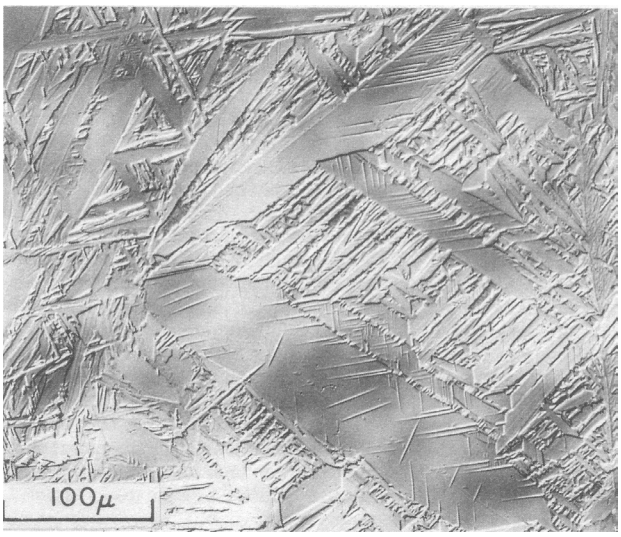

Figure 9: Optical micrograph of massive martensite exhibiting large colonies in a Ti-1.78 wt.% Cu alloy quenched from 900°C. From [23], p. 1436.

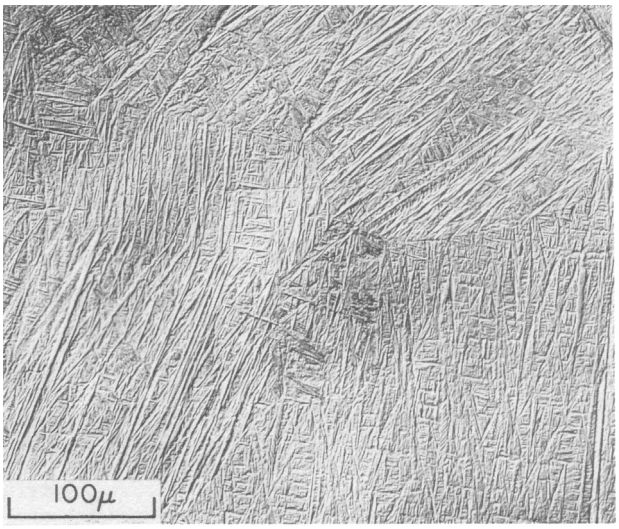

Figure 10: Optical micrograph of acicular martensite exhibiting large colonies in a Ti-12 wt.% V alloy quenched from 900°C. From [23], p. 1438.

Since no parent β phase is retained in massive martensite, difficulties arise in the determination of the habit plane. In acicular martensite, β is retained between the α′ plates allowing determination of the habit plane to be either $\{334\}_\beta$ or $\{344\}_\beta$.[37] The parent to product orientation relation for the β→α′ transformation has also been determined to be that of the characteristic Burger's orientation as was described for nucleation and growth of the α phase: $(110)_\beta \parallel (0001)_{\alpha'}$ and $<\bar{1}11>_\beta \parallel$ to $<11\bar{2}0>_{\alpha'}$.[23,37] For the β→α″ transformation the following orientation relationship is observed: $(110)_\beta \parallel (002)_{\alpha''}$ and $<111>_\beta \parallel <110>_{\alpha''}$.[27] The α′ plates have a transformation substructure of dislocations, while $\{10\bar{1}1\}_{\alpha''}$ twins are observed in the α″ substructure.[38]

Athermal ($\beta\rightarrow\omega_{ath}$) and Isothermal ($\beta\rightarrow\omega_{iso}$) Omega Formation

The metastable β→ω transformation drew much attention in the 1960's and 1970's because of its deleterious[39] effect on ductility in titanium and zirconium – transition metal alloys. The transformation may occur athermally upon quenching or by nucleation and growth processes on aging. The results of either the athermal or isothermal reaction is a coherent, fine (~20-3000 Å) precipitate that has a high particle density; therefore, the ω precipitates are commonly observed and characterized using electron microscopy and x-ray diffraction methods. Since the transformation is metastable, the ω phase will eventually revert to α under the appropriate

conditions. A comprehensive review of this transformation has been presented by Hickman,[40] with general reviews being presented by Williams,[23] Collings,[41] Murakami,[26] and Welsch and Boyer.[27] Important aspects of the athermal and isothermal transformations will now be discussed separately.

The athermal omega (ω_{ath}) phase is a result of very rapidly quenching in titanium-transition metal alloys able to retain the β phase at room temperature. The formation of the ω_{ath} phase occurs over a very narrow composition range[41,43,44] as illustrated in Figure 11. Athermal omega assumes a hexagonal lattice with the basal plane, $<0001>_{\omega}$, oriented parallel to the $<111>_{\beta}$ planes giving four ω variants in one β crystal.[9] Since the $\beta \rightarrow \omega_{ath}$ transformation cannot be suppressed, it was initially thought that the transformation was martensitic[43]; however, the ω_{ath} phase precipitates are extremely small (~20 - 40Å) with a high particle density as shown in Figure 12. Since a habit plane cannot be assigned to such a small particle, the ω_{ath} phase cannot be a product of a martensitic transformation.[23,44] De Fontaine, et. al.[45] proposed that the ω_{ath} transformation is a result of a displacement-controlled transformation.

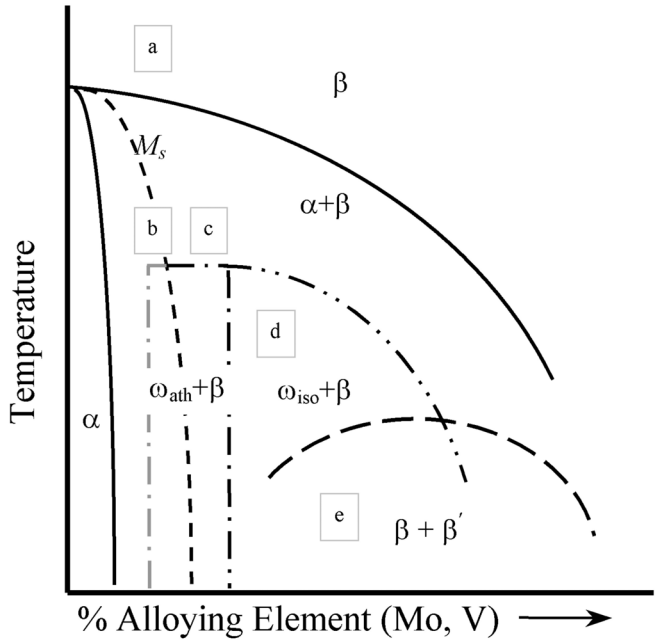

Figure 11: A schematic metastable phase diagram indicating the approximate position of athermal and isothermal omega formation as a result of quenching and aging, respectively. The β→βrich+β′ transformation is also indicated. Metastable phase boundaries are indicated by dashed lines. After: [26], p. 162; [42], p. 2469; [44], p. 1334; and [45], p. 1154.

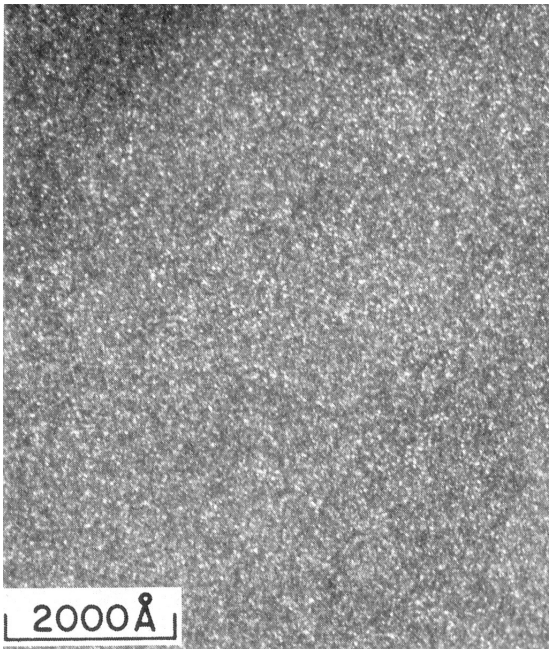

Figure 12: Dark field electron micrograph of fine athermal omega particles (white) in Ti-11.5Mo-4.5Sn-6Zr quenched from 900°C. From [23], p. 1446.

The omega phase may also form isothermally as fine coherent precipitates in moderately β-stabilized alloys during aging at temperatures up to ~550°C, also illustrated in Figure 11. The ω_{iso} precipitates are larger and form less dense than in athermal omega formation and the formation of ω_{iso} is diffusion controlled as opposed to the displacement controlled ω_{ath} formation. The volume fraction of the ω_{iso} phase decreases with increasing α-stabilizer additions and aging temperature. Ellipsoidal and cuboidal ω_{iso} morphologies have been observed as shown in Figure 13 and Figure 14. The morphology of the ω_{iso} precipitate has been shown to depend on the misfit between the precipitate and BCC lattice.[44] The ellipsoidal variety occurs in low misfit alloys such as Ti-Mo, Ti-Ta, and Ti-Nb, with the long axes of the precipitate lying parallel to the $<111>_{\beta}$ direction. Cuboidal precipitates are observed in alloys having high precipitate-lattice misfit such as Ti-V, Ti-Cr, Ti-Ni, and Ti-Mn, with the cube face parallel to $\{100\}_{\beta}$. Decreasing the misfit decreases the elastic strain energy thus minimization of the surface energy of the particle determines the ellipsoidal shape. The cuboidal shape results from the elastic strain energy being minimized.

A discussion of Figure 11 will be useful in understanding the β→ω phase transformation. Quenching from point "a" (composition, temperature) in Figure 11 will lead to formation of α′

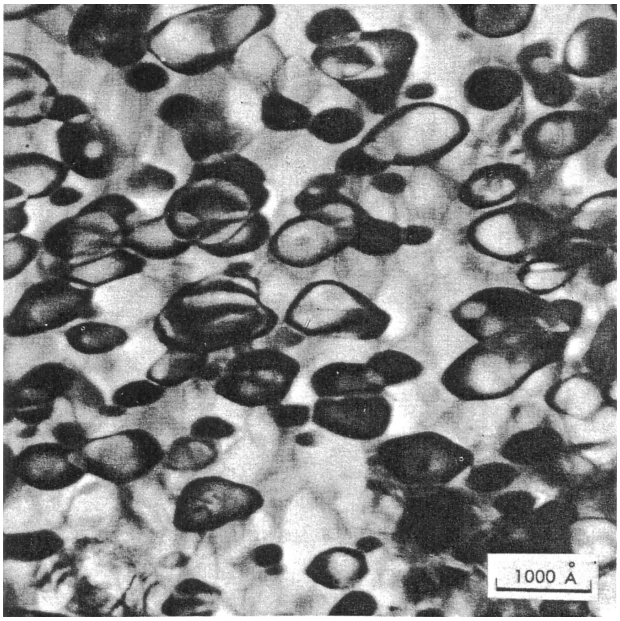

Figure 13: Ellipsoidal ω_{iso} phase particles in a Ti-11.6Mo alloy after aging 1150 hours at 400°C. From [42] p. 2464.

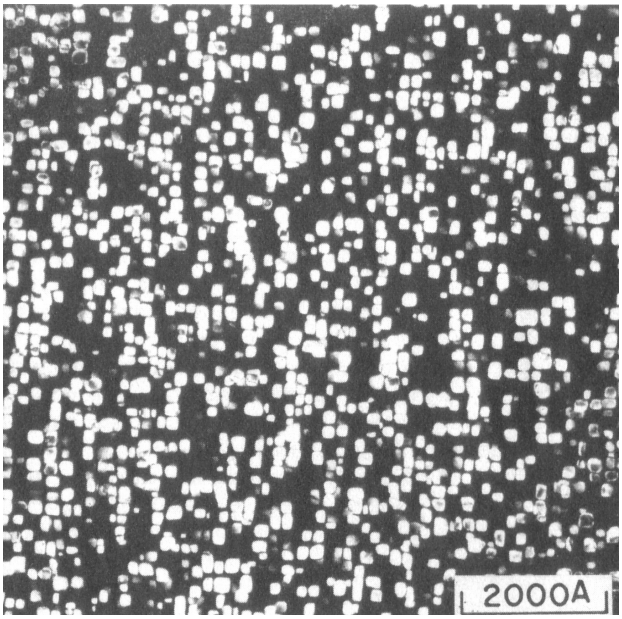

Figure 14: Dark field electron micrograph of cuboidal ω_{iso} phase in Ti-10wt.%Fe. From [23] p. 1452.

because M_s is intersected before ω_{ath}. Quenching from point "b" will result in athermal omega with the possibility that some beta phase may also decompose to martensite. Quenching from above point "c" will result in ω_{ath} formation because M_s will not be intersected. Quenching from any temperature intersecting the composition of point "d" will not produce any of the metastable transformation products discussed; however, aging from point "d" (within the $\omega_{iso}+\beta$ field) will result in isothermal ω formation.

β Phase Splitting ($\beta \rightarrow \beta_{rich} + \beta'$)

Like isothermal omega, in the phase splitting reaction $\beta \rightarrow \beta_{rich} + \beta'$, β' is a transformation product that occurs upon aging, preceding the formation of equilibrium α.[23] This transformation is of interest, not because it adversely effects mechanical properties, but because the β' zones serve as nucleation sites for α, leading to a fine α precipitates. β', which is lean in β solute, forms as uniformly distributed coherent BCC zones in the β matrix and may only be observed with electron microscopy techniques. Morphologies depend on the misfit of the solute rich and lean zones. The reaction occurs in alloys contain sufficient amount of β phase so that the phase splitting reaction precludes the isothermal omega reaction during low temperature aging; however, in theory, the solute lean β' regions have the correct composition to undergo the isothermal ω transformation, though only limited evidence exists for this to occur.[24] Figure 11 shows the approximate position of the $\beta+\beta'$ reaction for a β alloy. Aging at position "e" will lead to the phase splitting reaction.

α/β Interface Phase

A phase of complex[46,47,48] nature exhibiting an FCC or HCP crystal structure is found to occur at the α/β interface in α+β alloys. The presence of what is referred to in the literature as the *interface phase* has been shown to adversely affect mechanical properties. The formation of the interface phase appears to be an artifact[49,50,51] of hydrogen absorption during thin foil preparation, specifically during electropolishing. The interface phase is not observed in commercial alloys as long as hydrogen levels are kept sufficiently low.

Two Types of α (Type 1α and Type 2α)

The decomposition of metastable β to equilibrium α+β may include transition products such as the ω_{iso} and β' phases. Upon sufficient aging times, these transition phases will revert to equilibrium α by nucleation and growth processes. Two types of α phase may form as a result: Type 1α, or Burgers α, observes the Burgers relationship $(110)_\beta \parallel (0001)_\alpha$ and $<111>_\beta \parallel <11\bar{2}0>_\alpha$ and Type 2α which does not obey the Burgers relation, instead it exhibits $(10\bar{1}2)$ $<10\bar{1}1>$ twin orientation to the Burgers relationship.[52] In Ti-14Mo-6Al alloys, Rhodes and Williams[52] observed that Type 1α formed initially at aging temperatures in the range 400-650°C, being replaced by Type 2α after longer aging times. The Type 1α precipitates assume a needle morphology; Type 2α precipitates adopt the needle morphology but eventually colonize into fine fine Type 2α particles. Isaac and Hammond[53] resolved that the Type 2α phase has an FCC structure, was crystallographically similar α/β interface phase and like the interface phase, is an artifact of thin foil preparation.

A Note On the Occurrence of the Interface and Type 2α Phases

There has been some confusion in the literature regarding the interface phase and Type 2α. A final resolution to both the interface phase problem and Type 1 and 2α has been explained by Banerjee, et. al.[51] First, Type 2α has been shown to have an FCC structure similar to that observed in the interface phase, thus, we can assume the FCC interface phase is Type 2α. It is concluded that the FCC (Type 2α) phase is a hydride and both FCC and HCP structure arise from hydrogen-induced transformations brought about by thin foil preparation techniques and would not normally occur in bulk material unless hydrogen levels were sufficient. A recent publication[27] acknowledges the resolution of the interface face by Banerjee[51] but does not report that Type 2α is also a result of thin foil preparation.

Structure/Morphology – Mechanical Property Relationships

In this section, the effect of certain structures and morphologies on mechanical properties is examined. The approach taken is more general than the previous section on phase transformation since mechanical properties are not a main focus of this thesis. As a starting

point for further exploration into the structure property relationships existent in titanium alloys, the reader is referred to the work of Flower[15] and Lütjering[54], from which most of the information below was extracted. Table II gives a qualitative comparison of some important microstructural features in titanium alloys and the mechanical properties they enhance or degrade.

It is obvious that Table II provides little insight as to why, for example, Widmanstätten α increases fracture toughness while decreasing strength. Therefore the following microstructural morphologies will be discussed in reference to how they effect strength, ductility, fatigue, and

Table II: Morphology-Property Relationships in Titanium Alloys [a]

Feature	Enhances	Degrades
Elongated α	Fracture Toughness Notched Fatigue Resistance Fatigue Crack Growth Resistance	Ductility Fatigue Initiation Resistance Low Cycle Fatigue Resistance
Widmanstätten α	Fracture Toughness Notched Fatigue Resistance Fatigue Crack Growth Resistance Creep	Ductility Fatigue Initiation Resistance Low Cycle Fatigue Resistance Strength
Bi-Modal α	Strength Ductility Fatigue Initiation Resistance Low Cycle Fatigue Resistance	Fracture Toughness Fatigue Crack Growth Resistance
Colony α	Fatigue Crack Growth Fracture Toughness Notched Fatigue Resistance	Strength Ductility Fatigue Initiation Resistance Low Cycle Fatigue Resistance
Secondary α	Strength Ductility	Fracture Toughness
Grain Shape (elongated)	Fracture Properties Fatigue Crack Growth Resistance Notched Fatigue Resistance	Fatigue Initiation Resistance
Coarse Prior β Grains	Fracture Toughness Creep	Strength Ductility Low Cycle Fatigue Resistance Fatigue Initiation Resistance
Fine Prior β Grains	Strength Fatigue Initiation Resistance Ductility	Fracture Toughness Notched Fatigue Resistance
Mixed-Mode Grain Size	Strength Fatigue Initiation Resistance	Fracture Toughness
Alpha Films	Fatigue Initiation Resistance Notched Fatigue Resistance	Fatigue Crack Growth Resistance
Grain Boundary α	Fracture Toughness Fatigue Crack Growth Notched Fatigue Resistance	Ductility Fatigue Initiation Resistance Low Cycle Fatigue Resistance

[a] From Reference [27]

Note: These general relationships do not necessarily address specific comparison between microstructural features

fracture toughness: Colony and Basketweave Widmanstätten α, Grain Boundary α, Martensite, and Prior β Grain Size.

Strength and Ductility

The most influential microstructural parameter on the mechanical properties of fully lamellar (no thermomechanical processing) is the α colony size because it determines the effective slip length.[54] The slip length and β grain size has been shown to influence strength using a Hall-Petch relationship.[56,57] A fully lamellar structure is produced in cast structures or by heating into the β phase field for a sufficient period of time. Also, recall that the colony size decreases as cooling rate increases. The influence of α colony size on mechanical properties is schematically shown in Figure 15. Both ductility and yield strength decrease with increasing colony size. This is also illustrated in Figure 16 except the abscissa is the cooling rate from the β phase field. The abrupt increase in the yield strength is a result of the fine α basketweave arrangement produced from the martensitic transformation. The ductility exhibits a maximum for cooling rates in the range of 100 to 1000 °C/min before decreasing. Lütjering, et. al.[55] attributes the increase in ductility to the reduction in α colony size, with the subsequent decrease being attributed to the strength difference between the α+β matrix and softer grain boundary α. The difference in strength allows the grain boundary α to preferentially plastically deform, resulting in a change from transgranular fracture at low

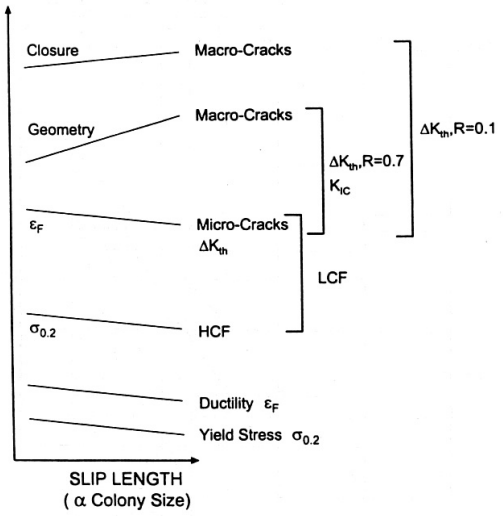

Figure 15: General influence of slip length (α colony size) on mechanical properties. [54], p. 36.

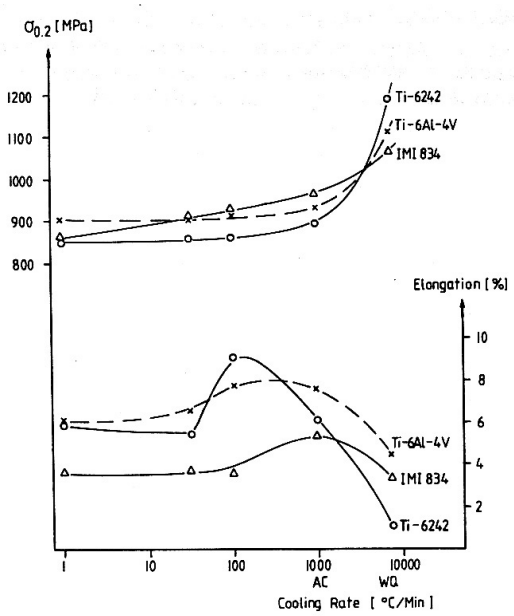

Figure 16: Effect of cooling rate from the β phase field on yield stress and ductility for three alloys having fully lamellar structures. [55], p. 67.

cooling rates to intergranular fracture at fast cooling rates.[55,54] The amount of grain boundary α is related to the prior β grain size, thus, ductility tends to decrease with increasing prior β grain size. Ductility decreases with increasing prior β grain size because of the increased grain boundary area. Also, as the amount of β increases, the strength difference increases resulting in a pronounced effect of grain boundary α on ductility in β alloys.

Fatigue

High cycle fatigue (HCF) depends on the ability of the microstructure to resist crack nucleation; therefore, HCF depends on the colony size in a similar manner to yield strength as illustrated in Figure 15. As the colony size increases, the stress amplitude at failure decreases. The prior β grain size has no effect on the HCF strength.[55]

For Low Cycle Fatigue (LCF), resistance to crack nucleation and propagation of surface cracks (microcracks), both of which depend on slip length, are important. Resistance to propagation of surface cracks is analogous to the dependence of slip length on ductility as illustrated in Figure 15. Both colony boundaries and martensitic plates are obstacles to crack nucleation; therefore, a reduction in the colony size or increased cooling rate will lead to a reduction in the crack propagation rate, *dA/dN*, and an increase in LCF strength.[54] A reduction in the β grains size for slower cooled (colony α) microstructures has been shown to increase the LCF strength,[55] contrary to the effect of prior β grain size on LCF strength shown in Table II. For large cracks (macrocracks), such as that measured using Compact Tensile (CT) specimens with through thickness cracks, crack geometry and the stress ratio, *R*, become important in addition to ductility.[58] At high *R* ratios (no crack closure) geometry (crack front roughness) plays a significant role, with the crack front roughness increasing with the colony size as shown in Figure 15. For α+β titanium alloys, the effect of crack front roughness is generally stronger than ductility, and *da/dN* will decrease with increasing colony size or decreasing cooling rate.[54] For low *R* ratios, crack closure becomes an important factor and further increases the effect of the geometry term. In summary, an increase in α colony size leads to a decrease in *da/dN* for large cracks, but an increase in *da/dN* for microcracks.

Fracture Toughness

The fracture toughness depends on microstructure behaves in a similar manner to advancement of macro-cracks without crack closure (Figure 15). The crack geometry term (rough crack front) dominates the ductility term (resistance to crack propagation), leading to an increase in fracture toughness with a larger colony size.[54] An α platelet morphology such as basketweave Widmanstätten α produces a more tortuous crack path (Figure 17) and as a result fracture toughness is increased. In the basketweave structure an advancing crack is deflected at the α/β interface. In colony Widmanstätten α the colony behaves as a single orientation unit and the crack will not deflect at the α/β interfaces. Instead, the crack will change paths upon encountering a colony of different orientation.[15] The colony size should not be a large fraction of the prior β grain size since crack path changes would be too infrequent to have a positive effect on fracture toughness. A martensitic structure has an adverse effect on fracture toughness, due to the decrease in ductility associated with such a structure.

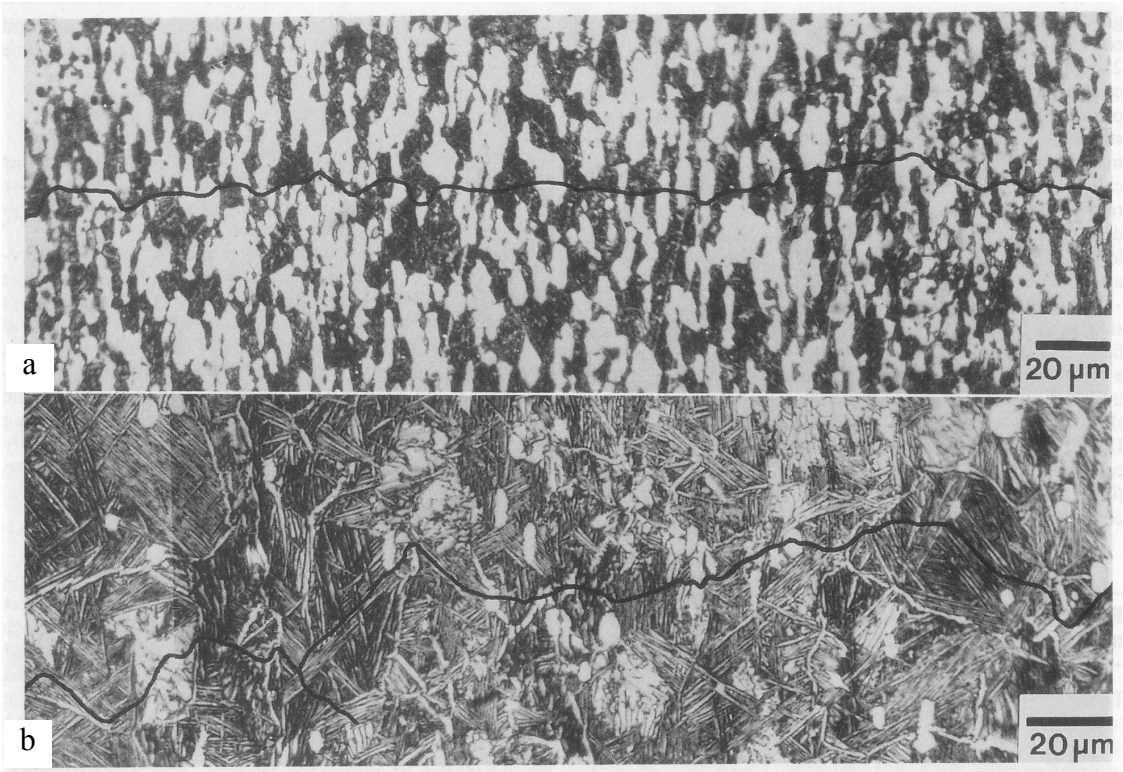

Figure 17: Optical micrographs of plastic replicas stripped from fatigue specimens of IMI 550 (Ti-4Al-4Mo-2Sn-0.5Si), showing the eventual path taken by advancing crack. (a) Represents an equiaxed α+β morphology while (b) contains a small volume fraction of primary and basketweave Widmanstätten. The crack growth rate (*da/dN*) in (b) is lower than in (a). From [15], p. 1086; After [59].

Rapid Manufacturing

Introduction

Rapid manufacturing (RM) processes, also known as Solid Freeform Fabrication (SFF), have drawn much attention in recent years with several conferences, symposia[60], books[61,62,63], and countless papers devoted to the topic. RM is used to produce prototype models or production parts in small quantities quickly, thereby realizing labor, time, material, and ultimately, cost savings over conventional processing routes. Rapid manufacturing is a broad description of processes that have evolved from rapid prototyping (RP). There are four main steps in any RP process: (1) a three dimensional prototype is drawn using CAD software; (2) a software program slices the 3D model into 2D layers; (3) the sliced model is then interpreted by process control software to determine appropriate processing conditions during the build; (4) the physical prototype is built layer by layer. The advantages of the RP process are many:

- Scaled down prototypes can be built without sacrificing detail.
- Since most RP processes are "by wire," model geometry, process parameters, and even materials can be changed on the fly.
- RP machines are such that several different prototypes can be built during the same processing run.
- No jigs or molds are needed; when required, support structures can be built into the model and removed after the part is built.
- Most RP processes are additive, resulting in little or no machining required to attain fine detail and precise tolerances.

The earliest instance of RP is also the most intuitive. Topographical models were fabricated by assembling a series of wax plates having the shape of the contour lines on a topographical map. This layer additive approach as has been advanced through the use of laser power to either cure a resin, sinter, or melt particles to form a three dimensional part from powder. A recent textbook[63] categorizes and defines 21 different methods involving different target material systems, delivery methods, deposition methods, and power sources. There could possibly be three times as more methods, all at different developmental levels in existence today. Four of the more common and technologically important methods will be discussed below in order of increasing detail:

Stereolithography (SL), Selective Laser Sintering (SLS), Laser Engineered Net Shaping (LENS), and Direct Metal Deposition (DMD). The context of the discussion will remain limited to a definition/description of the process, applications and future direction.

Stereolithography (SL)

Stereolithography processes involve the curing of a photosensitive resin or polymer using a laser or ultraviolet light source. As the laser scans a vat of photocurable liquid polymer, a hardened 2 1/2-dimensional† layer is formed. The vat of polymer is stepped down in the *z* direction (away from the focal point of the laser), allowing a layer of resin to cover the previously cured layer. The laser scans the next slice and the process is repeated. Newer SL machines apply a new layer of resin using a blade to spread the resin resulting in better accuracy, smoother surface finish, and elimination of trapped volumes of resin. Once the part is completed, it is removed from the resin vat and the excess resin drained before undergoing a postcure treatment in an ultraviolet oven.

3D Systems' Stereolithography Apparatus (SLA) was the first commercially available layer-additive process for creating physical objects from CAD data. They have designed scan processes and resins to improve dimensional accuracy and green strength, and reduce warping. SLA can maintain dimensional accuracy to ±100μm and produce layers 25μm thick. Disadvantages to the process mainly deal with the material. The resin is costly, toxic, sensitive to light, and difficult to change.

Selective Laser Sintering (SLS)

The SLS process is similar to Stereolithography in most ways except that the material is in powder form and a selectively scanning laser each layer to fuse the areas defined by the geometry cross section and to fuse together the new and underlying layers. Powder particles are fused together in many ways including melting and surface bonding. Sintering aids or polymer coatings can be applied to ceramic or metallic powders to form a green preform which can be later sintered or otherwise infiltrated. A new layer of powder is applied using a rolling cylinder or a scraper. The bed of powder serves as a support structure for overhanging layers.

The SLS process was developed and patented at the University of Texas at Austin. The process was commercialized by DTM Corporation, now a subsidiary of 3D Systems. Unlike the

stereolithography processes the major advantages of the SLS process lie in the materials, as any substance that can be pulverized into a fine powder can be used. Polyamides (nylon), nylon composites, polystyrene, and polycarbonate are typically used in SLS. They are cheaper and more environmentally friendly than resins and may be sintered at lower laser powers (10-20W). Disadvantages of the process are that cooling times can range from 6 to 8 hours, an inert nitrogen atmosphere is needed, the process must be optimized for the material, recycled powders must be sieved, and since the process involves loose powder, it can be messy. Future work with this process includes the development of new materials for SLS.

Direct Metal Deposition (DMD)

Laser Engineered Net Shaping (LENS™)

The LENS process uses a high power laser (750 – 2200 W Nd:YAG) to melt metal powders that are injected into the focal point of the laser beam. Simultaneously, the substrate on which the powder is being deposited moves in the *x* and *y* directions to fabricate the desired cross-sectional area of the particular layer. The laser and powder delivery system are stepped up in the *z* direction and the next layer is deposited, eventually forming a fully dense metal component. This is a truly additive process in that layers are built vertically without preplaced powder for support. The LENS process is capable of producing net shape parts within a tolerance of ±125μm at a deposition rate of around 2500 $mm^3 \cdot hr^{-1}$ (laser speed ≈7 mm/s, layer thickness ≈ 0.25 mm, layer width ≈ 0.4mm)[64] or about 0.045 $kg \cdot hr^{-1}$.[65]

Originally developed at Sandia National Labs and commercialized by Optomec Design Company, virtually any metal can be used in the LENS process, including titanium alloys, tool steel, nickel alloys, stainless steel, and many other alloys used in small batch production applications. The LENS process is suitable for small objects as it has a slow deposition rate as compared to other direct metal deposition processes. The layer-by-layer nature of this process allows for the fabrication of seamless internal geometries such as cooling channels or other hollow features. The powder delivery system allows for the in situ alloying or grading of the material composition to produce different properties in different locations in the build.

Laser Forming

AeroMet Corporation's LasForming™ [66,67,68,69] is a DMD process similar to LENS that is more suited to building larger parts with a deposition rate that is two orders of magnitude larger than the LENS process (0.045 vs. 4.5 $kg \cdot hr^{-1}$)[65]. At these high deposition rates, a near-net shape part is produced that requires some post forming machining; however, the machining requirements are often 50% less than those of forgings. The LasForming process is well suited for short production runs, eliminating the need for expensive molds or dies and reducing the time needed to produce a part by 50 to 75%. A comparison of manufacturing factors for the LasForming conventional processes is shown in

Table **III**. In addition to building structural components for the aerospace, defense and chemical industries, the additive nature of the LasForming process allows for the addition of features such as lugs or extensions to forgings, castings, or extrusions, thereby reducing the complexity of conventional processing operations. Also, damaged components such as tool dies can be repaired using the LasForming process.

Table III: General Comparison of Selected Manufacturing Factors for LasForm Ti-6Al-4V Aerostructures with Similar Products Made By Forging, Machining from Plate, and Casting. From [67].

Comparison	LasForming	Forging	Machining	Casting
Buy/Fly Ratio	1.5/1	10-20/1	10-20/1 and higher	5/1 (includes gates and risers
Feedstock	Plate/Powder	Ingot	Thick Slab	Melt Stock
(Form/Delivery Time)	Weeks	6 Months	6 Months	Weeks
Non-Recurring	Software	Die Sets	Software	Molds/Software
Cost	$1K-$50K	$200K-$1M	$1K-$50K	$50K-$1.5M
Cycle Time	1 week	6 months	1 week	3 months
Forming Operation	DMD	Forge from ingot	Mill from slab	Cast in ceramic mold
Cycle Time	1-2 days	4 months	1-2 months	6-12 months
Recurring Expenses	Argon	Furnace gases, recover flash, repair dies	Cutting tools	Molds, dies, recover gates, risers, sprue
Distortion	Moderate	Heavy	Low	Varies
Post Forming Heat Treatment Time	Less Time (thin walls)	Longer, several times (Thicker),	Linger, 1 time, (thicker)	Longer, one time (thicker)
Alpha Case	No	Yes	Yes	No (after Chem

				Mill)
Response Time to Design Change	1-2 Days (Software Change)	Change Dies (6 Months)	1-2 Days (Software Change)	Change Molds (3 months)
Delivery Time	2 months	12-18 months	6+ months	6 months
Time Cost of Money	Low Exposure	High Exposure	Low Exposure	Moderate Exposure
Mechanical Strength	High	High	High	Moderate
Graded Materials	Yes	No	No	No

AeroMet's LasForming system is shown in Figure 18 with processing features and capabilities as shown in. The LasForming process operates like many other RM processes in that a CAD file is used to generate laser scan paths (trajectories) for a two dimensional layer and the part is built layer by layer by stepping the focal length a required layer distance. Pre-alloyed or blended elemental powder is introduced into the focal point of the laser beam through a high-mass flow rate powder feed system developed by MTS Corporation. A molten puddle is formed as shown in Figure 19; the motion of the CNC base traces out the pattern of the desired shape, forming a fully dense layer of titanium alloy. Layers are added by indexing the focal point and scanning the pattern of the next layer. The final product is a near-net shape part (machining preform) that has a ribbed texture as shown in Figure 20. Since the process is performed in a high purity argon atmosphere containing less than 100 ppm oxygen, Ti-6Al-4V alloys having less than 0.2 wt.% oxygen and ELI grade titanium alloys (< 0.09 wt.% O_2) can be produced. The final part is obtained after post-forming machining, heat treatment (recrystallization anneal and solution aging), and inspection (ultrasonic, dye penetration, and x-ray). Examples of the final

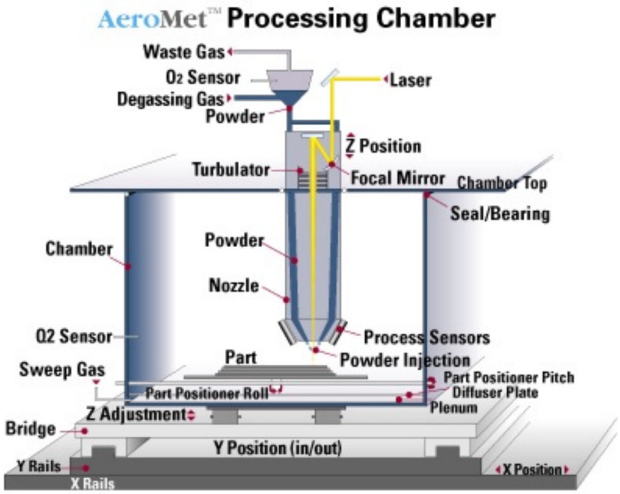

Figure 18: AeroMet Laser Additive Manufacturing Process Chamber. From [69].

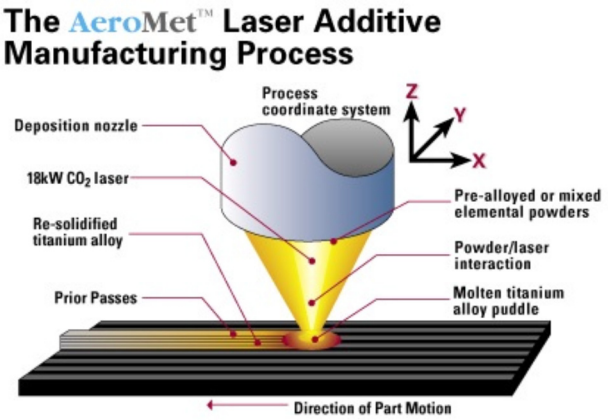

Figure 19: The AeroMet Laser Additive Manufacturing Process. From [69].

parts are shown in Figure 21. Internal geometries such as hollow cones or overhangs angled as much as 60° from vertical can be manufactured. Alloys that AeroMet has used in their process include: Ti-6Al-4V, Ti-5Al-2.5Sn, Ti-6Al-2Sn-4Zr-2Mo-0.1Si and Ti-5Al-2Sn-2Zr-2Cr-2Mo-0.25Si. Future concepts to be explored by AeroMet include, built -up structures (unitized structures eliminating fasteners), functionally graded structures, and structures utilizing other materials including niobium, rhenium, inconel, and stainless steels.[68]

Table IV: Capabilities of LasForm and LENS DMD Processes

Parameter	**LasForm**	**LENS**
Laser	18 kW Continuous CO_2	1-2 kW Nd:YAG
Powder Delivery	High-Mass Rate Powder Feed, single axis	Powder Feed, multi-axis
Chamber Size	$12_l \times 4_w \times 4_h$ ft [$3.7_l \times 1.2_w \times 1.2_h$ m]	$1.5_l \times 1.5_w \times 3.5_h$ ft [$0.46_l \times 0.46_w \times 1.07_h$ m]
Work Table Capacity	20,000 pounds [9 tons]	20,000 pounds [9 tons]
Atmosphere	Dynamically Purged with high purity Argon, (< 150 ppm O_2)	Argon
Deposition Rate	2.0 - 9.9 $lb_m \cdot hr^{-1}$ [0.90 - 4.5 $kg \cdot hr^{-1}$]	0.1 $lb_m \cdot hr^{-1}$ [0.045 $kg \cdot hr^{-1}$]
Powder	Pre-Alloyed, Blended Elemental -40 +325 mesh, Graded Capability	Pre-Alloyed, Blended Elemental, Graded Capability
Near, Net Shape (Oversize)	Near-Net (0.03 - 0.2 in [0.762 - 5.08 mm])	Net
Reproducibility	±0.03 in [±0.76 mm]	±0.005 in [±0.127 mm]
Layer Dimensions	[$\approx 15_w \times 8_h$ mm]	[$\approx 1_w \times 2_h$ mm]
Typical Products	Small to Large Structural Parts	Small Structural Parts, Tooling

Figure 20: Machining preform (rib-on-web geometry) of a LAM Ti-6Al-4V part. From [69].

Figure 21: Machined LAM Ti-6Al-4V parts. From bottom left counter clockwise: cylindrical geometries, aircraft fitting, and angled walls. From [69].

Variables and Considerations in the Direct Metal Deposition Process

In order to fully understand the end result of the DMD process, one must appreciate the variables and other considerations that control the DMD process. Review articles on the topic by Laeng *et al*[70], and Lewis and Schlienger[71] will be summarized below. A book by Steen[72] is also an invaluable source of information on laser processing in general. Important aspects of a DMD process include laser-metal interactions, laser variables, powder delivery, and process monitoring. Of course there are other important aspects to the DMD process, such as how the solid model is sliced and translated into process commands, which will not be discussed here since the main focus of this thesis is on the deposited structure itself.

Laser-Metal Interaction

A laser (Light Amplification by the Stimulated Emission of Radiation) generates photons through stimulated emission, were an active medium is stimulated or "pumped" with a DC, RF, or light source such that the molecules assume excited states.[73,74] By chance a molecule in the excited state passes a photon and undergoes stimulated emission, resulting in the excited atom returning to the ground state and the emission of a photon of light with a characteristic wavelength. The photons oscillate between mirrors located at the ends of a cylindrical cavity, where one of the mirrors is completely reflective and the other is partially transparent. The oscillating photon may be absorbed by a molecule in a lower energy state, leave the cavity, or strike a molecule in the excited state. If the latter occurs, another photon will be emitted, travelling in exactly the same direction and with exactly the same energy, and the associated electromagnetic waves are perfectly in phase. The process repeats itself, but in order for the process to work, one condition must hold: there must be more molecules in the upper states than in the lower states, in other words, a population inversion must be achieved. One difficulty remains: eventually the population inversion will revert to having more molecules in the ground state and these molecules will eventually consume all of the available photons. This is solved by increasing the number of energy levels available such that the molecule decaying from the excited state enters a metastable state. The molecule in the metastable state makes the lasing transition into a higher metastable state, which in turn decays rapidly to the ground state. The atom in the ground state cannot absorb the energy of the photon emitted in the lasing transition and a workable laser is obtained. The population inversion is maintained because the atoms

decay more rapidly in the lower energy metastable state than in the higher energy metastable state.

If the photon energy is sufficient and properly focused, it can be used to melt metallic materials. Not all of the energy is absorbed into the material; energy is also reflected and possibly transmitted through the target. The fraction of absorbed, transmitted and reflected energy sums to unity. The total energy interacting with the target is given in Equation [1] where the coefficients *A*, *R*, and *T* refer to the absorbtivity, reflectivity and transmissivity of the material.

$$E = A \cdot E + R \cdot E + T \cdot E \qquad [\ 1\ ]$$

The absorbed energy is typically very low, around 10 to 20 percent of the total energy, because of the high reflectivity of metals, especially at larger laser wavelengths. For example, CO_2 and Nd:YAG lasers have wavelengths of 10.6 and 1.06 μm, respectively. For a given material more energy input would be required of the CO_2 than the Nd:YAG laser to melt a metal powder. The amount of energy absorbed by the laser can be enhanced by redirecting the reflected energy back onto the target[75] or increasing the temperature of the target.[76]

The energy that enters the material is continuously absorbed. Beer-Lambert's law quantifies the amount of energy at a depth *z*, E_z, as Equation [2] where μ is the absorption coefficient.

$$E_z = (A \cdot E)e^{-\mu z} \qquad [\ 2\ ]$$

At the surface of the material Equation [1] reduces to $E_z = E_0$. The laser energy penetration depth for a given material is defined as $p = 1/\mu$. At a depth of $z = p$, about 63% of the initial energy has been absorbed. The phase changes that result in the interaction of a laser beam with a metal are illustrated in Figure 22. Lasers have the capability of melting, boiling and forming plasma if sufficient power is applied. The keyhole occurs if there is sufficient energy density per unit length to form plasma. The motion of the liquid metal in the melt pool is very turbulent.

Laser Variables

In addition to material properties and type of laser, the intensity and distribution of the laser power are important factors that will determine other process variables such as deposition rate. The energy intensity of the beam depends on the laser power, *P*, velocity of the target, *v*, and spot size of the laser, *d* according to Equation [3].

$$I = \frac{P}{vd} \qquad [3]$$

For a given laser power, increasing the spot size and target velocity will decrease the intensity. In order for a laser to effectively melt a layer of metal to form a seamless bond with the base metal (cladding), a laser power of about 1 kW is required. Figure 23 shows a region in which laser cladding is feasible for blown powder. The region is bound by dilution (melting of the substrate), an aspect ratio (clad width to height), and an energy intensity limit.

Another laser variable that is important to the DMD process is delivery of the laser beam. The beam must be transported from the source to the target and properly focused to obtain the appropriate energy density and spot size. Optical systems used to deliver the beam to the target include reflective-transmissive (CO_2) and fiber optic beam delivery (Nd:YAG). The reflective-transmissive method, commonly used with CO_2 lasers, consists of a series of reflective mirrors aligned at specific angles to deliver the beam to the target. The fiber optic system is commonly used with Nd:YAG systems and as the name suggests, consists of a fiber optic cable to transmit the beam to the target. Advantages in using the fiber optic delivery system include ease of delivery (with the reflective system, the entire system sealed to avoid contamination, provide a safety mechanism from the invisible beam), ease of alignment (again, lack of mirrors) and ability to incorporate multiple degrees of freedom.

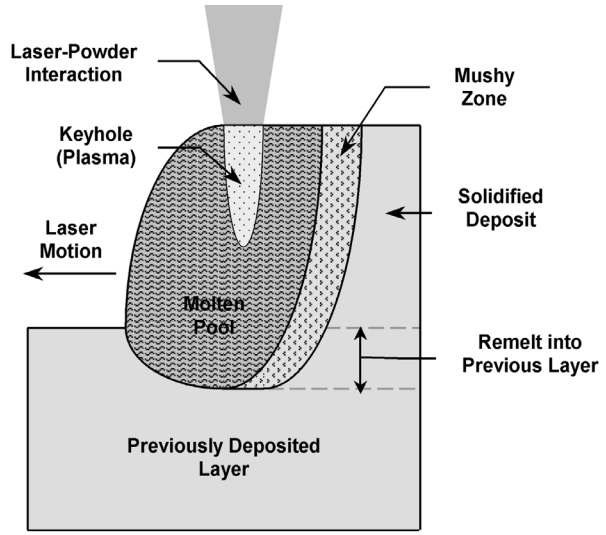

Figure 22: Illustration of the phase changes present in direct metal deposition processes.

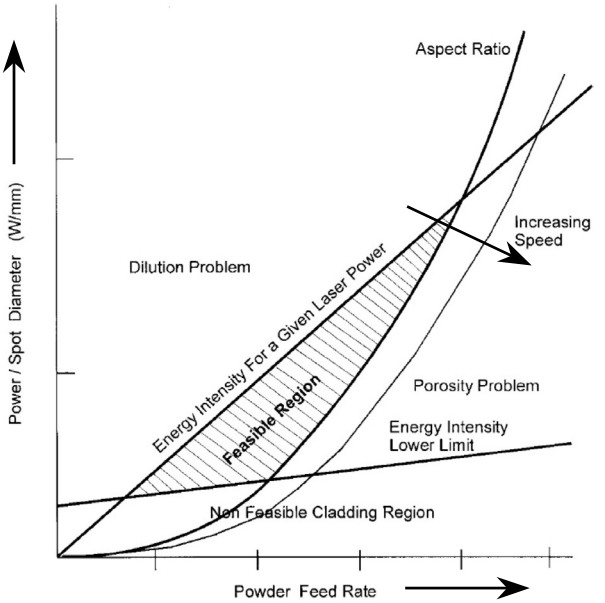

Figure 23: The operating window for blown powder laser cladding. After [75] in [70] p. 3980; [72], p. 250.

Powder Delivery

The delivery of the material into the focal point of the laser beam another is important aspect of the DMD process. Powder can be preplaced, wire-fed, or pneumatically fed (blown). In the preplaced powder method, a layer of powder is deposited first, then the laser beam scans the bed of powder. This method is good for single line builds, but not for multiple tracks as porosity, gaps, and cracking become a problem. Some control in the amount of matirial at the focal point of the laser can be obtained using feeding methods. Wire feed is useful in building rotationally symmetric shapes that can be rotated in one continuous track. The powder feed method gives the best control of any powder delivery method. In the powder feed method powder is fed using an inert gas from a storage container that can be preheated, through a splitter that delivers the powder to a nozzle(s). The powder is then injected into the focal point of the beam resulting in a molten puddle of metal. The transport gas doubles as a shielding gas to potect the metal from oxidation. Powder feeding can be lateral, multiaxial, or coaxial (concentric), with the multiaxial and coaxial being the methods of choice for DMD because they offer the greatest process control, part quality and complexity.

Process Control

The true advantage of any rapid manufacturing process is in situ process control. Variables such as laser power, table speed, melt pool temperature, powder and gas feed rate, and build temperature can be measured and adjusted in-flight to control the process. The most important to this work is temperature measurement. Griffith, et al[77] measured the thermal excursions of an H13 tool steel build using thermocouples placed along the height of the build and Hofmeister, et al[78,79] used high speed CCD cameras to measure the melt pool temperature and subsequent solidification rates.

Numerical Methods

Principles

Numerical methods are useful for solving problems in fluid dynamics, heat and mass transfer, and other partial differential equations describing physical phenomena. They are oftentimes necessary when trying to solve problems with complex shapes, boundary conditions, and other non-linearities, where an analytical solution would be impractical or impossible. Presently, two numerical methods are commonly used is the solution of these complex partial differential equations: the *finite difference method* (FDM) [80] and the *finite element method* (FEM)[81,82]. The basic concept behind both methods is to subdivide the problem's physical domain into a network of small regions or *elements* that are assigned a reference nodal point or *node* to each element. In the FEM, an approximate solution to the complex problem is obtained by representing the solution within each of the elements by a relatively simple function. The spatial and temporal derivatives of the partial differential equation are approximated over the dimensions of the element in the FDM. FEM is more suitable for geometrically complex physical domains through the use of variable size and shape elements, while the FDM is limited to rectangular geometries. Since the problem at hand (modeling the thermal behavior in the Laser Additive Manufacturing process) is of simple rectangular geometry, further discussion will only focus on the FDM. Explicitly, the methods used to derive finite difference equations for steady state, transient, and non-linear heat flow and heat flow coupled with a phase change will be described.

Finite Difference Method

As mentioned above, the basic philosophy in using numerical techniques to solve complex partial differential equations is the subdivision of the problems physical domain into elements, each having a reference node. The aggregate of these points is termed the *nodal network*, *grid*, or *mesh*. As the mesh becomes finer (numerous elements are used) the analytical solution is approached. The computational cost of a fine mesh is high as illustrated by the following statement: if N nodes are chosen, there exists a system of N algebraic equations that must be solved for in order to give a solution to the problem. The goal becomes the derivation of

the system of algebraic equations such that they represent the physical phenomena described in the problem, and solving for this set of equations to obtain an approximate solution.

Before one can derive the finite difference equations representing a physical problem, the partial differential equation must be classified into one of three categories: elliptic, parabolic, or hyperbolic. To illustrate the classes, we consider the linear† 2nd order partial differential equation for a conic section[83] (Equation [4]) in two independent variables x and y.

$$A\frac{\partial^2\phi}{\partial x^2}+B\frac{\partial^2\phi}{\partial x\partial y}+C\frac{\partial^2\phi}{\partial y^2}+D\frac{\partial\phi}{\partial x}+E\frac{\partial\phi}{\partial y}+F\phi+G(x,y)=0 \qquad [\ 4\ ]$$

Equation [4] at the point (x_o,y_o) is classified as elliptic, parabolic, or hyperbolic if:

$$B^2-4AC<0\ ,=0,\text{or}>0 \qquad [\ 5\ ]$$

respectively. The names are derived from the graphical form of Equation [4] which represents an ellipse, parabola, or hyperbola according to Equation [5].[84] Examples of each class are shown in Table V.

Table V: Classification of Selected Second Order Partial Differential Equations

Description	Equation	Class
Steady State Heat Conduction	$\frac{\partial^2 T}{\partial x^2}+\frac{\partial^2 T}{\partial y^2}=0$	Elliptic
One-Dimensional Transient Heat Conduction	$\frac{\partial^2 T}{\partial x^2}=\frac{1}{\alpha}\frac{\partial T}{\partial t}$	Parabolic
2nd Order Wave Equation	$\frac{\partial^2\phi}{\partial x^2}=\frac{1}{c^2}\frac{\partial^2\phi}{\partial t^2}$	Hyperbolic

The physical significance of these classifications is as follows. For an elliptic system, the conditions at any given location are influenced by changes in conditions at both sides of that location, whether the changes are in the x or y variable. The two dimensional steady-state heat conduction (Table V) is elliptic in x and y spatial coordinates. The one-dimensional transient heat conduction equation (Table V) is elliptic in the x variable for the same reasons as stated above; however, in the time variable, the conditions at any instant are only influenced by changes taking place at earlier times, hence the conditions on the time derivative take precedence and the entire equation is parabolic in t. A parabolic equation has at least one variable that is

† The coefficients of the partial derivatives are functions of the two independent variables, but not the dependent variable.

influenced by changes on only one side (i.e. earlier time, or upstream location). The significance of a parabolic partial differential equation such as the transient heat conduction equation in a computational sense, is that the temperature field at any time is not influenced by the temperature field at future times, hence one starts with a given temperature field and marches forward to compute the field at future time steps. Lastly, elliptic equations are usually free of discontinuities or waves; parabolic equations have an infinite wave speed; and hyperbolic equations have a finite wave speed. The discussion henceforth will be limited further to the parabolic one and two dimensional transient heat conduction equations.

Steady-State Finite Differencing

In the FDM, the finite difference equations are typically derived in the following order. First, a Taylor Series approximation of the derivatives is made, then a control volume is applied to a node where a physical quantity such as energy is conserved over the control volume. Before equations can be derived, we must first define a coordinate system for the physical domain and a labeling convention for the nodes contained in the domain. This is illustrated in Figure 24[85] along with the control volume concept, where a dashed box indicates the nodal control volume or element. The local coordinate system shown in Figure 24 will be used throughout this work. For example, the temperature of the central node (m,n) is denoted $T_{m,n}$, and its adjacent right-

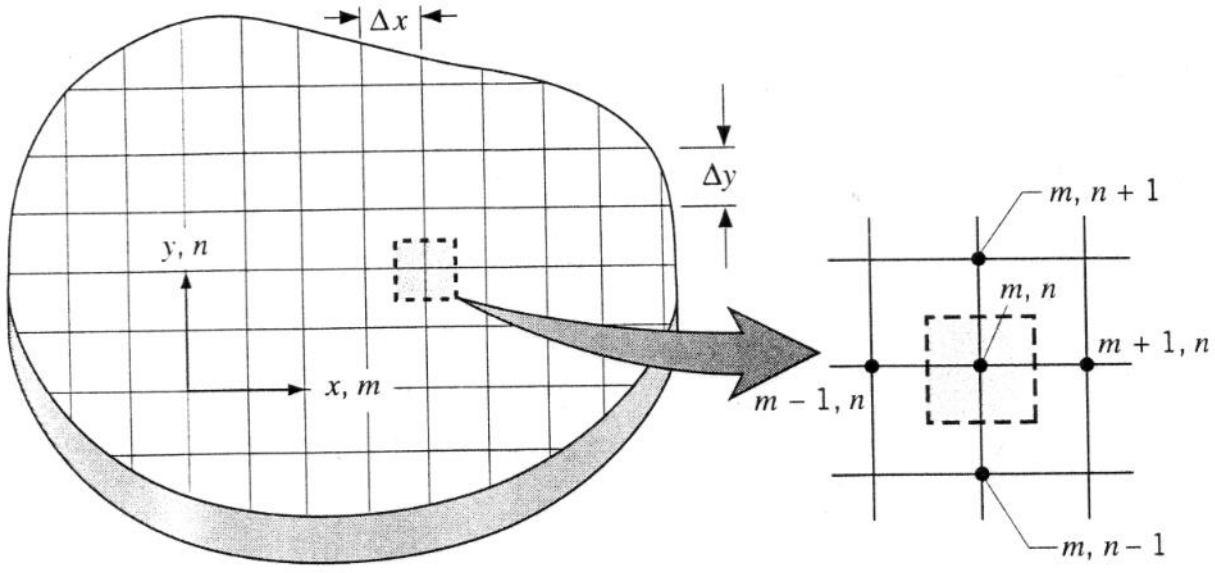

Figure 24: Two dimensional nodal network used to derive finite difference equations. The dashed box represents a control volume or element for the node *n, m* of size $\Delta x \times \Delta y$. Node *n, m* is found at the position (x_n, y_m). From [85], page 174.

hand node $(m+1,n)$ is $T_{m+1,n}$ and so forth.

Consider the two-dimensional steady state heat conduction equation with no internal heat generation shown in Equation [6]:

$$\frac{\partial^2 T}{\partial x^2} + \frac{\partial^2 T}{\partial y^2} = 0 \qquad [\ 6\ ]$$

The second order partial derivative in the x-coordinate can be approximated by taking a Taylor Series expansion of the function, $T(x)$ about a point $x_{m,n}$ in the positive (forward) and negative (backward) x direction and combining these two expansions to find a central difference approximation to the derivative about the node m,n. The forward and backwards Taylor series approximations are illustrated in Equations [7] and [8], respectively:

$$T_{m+1,n} \approx T_{m,n} + \Delta x\left[\frac{dT}{dx}\right]_{m,n} + \frac{(\Delta x)^2}{2!}\left[\frac{d^2T}{dx^2}\right]_{m,n} + \frac{(\Delta x)^3}{3!}\left[\frac{d^3T}{dx^3}\right]_{m,n} + \ldots \qquad [\ 7\ ]$$

$$T_{m-1,n} \approx T_{m,n} - \Delta x\left[\frac{dT}{dx}\right]_{m,n} + \frac{(\Delta x)^2}{2!}\left[\frac{d^2T}{dx^2}\right]_{m,n} - \frac{(\Delta x)^3}{3!}\left[\frac{d^3T}{dx^3}\right]_{m,n} + \ldots \qquad [\ 8\ ]$$

Rearranging equations [7] and [8], the forward and backwards finite difference approximations for the first derivative become:

$$\left[\frac{dT}{dx}\right]_{m,n} = \frac{T_{m+1,n} - T_{m,n}}{\Delta x} + O(\Delta x) \qquad \text{(forward)} \qquad [\ 9\ ]$$

$$\left[\frac{dT}{dx}\right]_{m,n} = \frac{T_{m,n} - T_{m-1,n}}{\Delta x} + O(\Delta x) \qquad \text{(backward)} \qquad [\ 10\ ]$$

where the term $O(\Delta x)$ is the truncation error and contains the terms in equations [7] and [8] not used in Equations [9] and [10]. Subtracting Equation [8] from [7] we obtain Equation [11], the central difference approximation to the first derivative

$$\left[\frac{dT}{dx}\right]_{m,n} = \frac{T_{m+1,n} - T_{m-1,n}}{2\Delta x} - O(\Delta x^2) \qquad \text{(central)} \qquad [\ 11\ ]$$

where the error has been improved to second order in the spatial increment $O(\Delta x^2)$. The central difference approximation of the second derivative of temperature with respect to x in Equation [6] is found by adding Equations [7] and [8] to obtain Equation [12].

$$\left[\frac{d^2T}{dx^2}\right]_{m,n} = \frac{T_{m-1,n} - 2T_{m,n} + T_{m-1,n}}{\Delta x^2} - O(\Delta x^2) \qquad \text{(central)} \qquad [\ 12\ ]$$

The central difference approximation of the *y* coordinate derivatives can be made in a similar fashion giving Equations [13] and [14] for the first and second derivatives:

$$\left[\frac{dT}{dy}\right]_{m,n} = \frac{T_{m,n+1} - T_{m,n-1}}{2\Delta y} - O(\Delta y^2) \qquad \text{(central)} \qquad [\ 13\ ]$$

$$\left[\frac{d^2T}{dy^2}\right]_{m,n} = \frac{T_{m,n-1} - 2T_{m,n} + T_{m,n+1}}{\Delta y^2} - O(\Delta y^2) \qquad \text{(central)} \qquad [\ 14\ ]$$

The equations necessary for approximating the solution to Equation [6] about the interior node *m,n* have been derived and give Equation [15] assuming a uniform mesh of $\Delta x = \Delta y$:

$$T_{m,n+1} + T_{m+1,n} + T_{m,n-1} + T_{m-1,n} - 4T_{m,n} = 0 \qquad [\ 15\ ]$$

Equation [15] states that the temperature of an internal node *m,n* having no internal heat generation, is simply one fourth of the sum of the temperatures of the surrounding nodes. Only the four nearest neighboring nodes have been considered to contribute to the temperature of node *m,n*. Özişik[80] considers finite difference approximations where 8 and 12 neighboring nodes contribute to the temperature of the central node *m,n* in order to improve the accuracy of the approximation.

Taylor Series approximations of the derivatives in the two-dimensional steady-state heat conduction equation are useful for determining temperature distributions for interior nodes because only the conduction terms are included. For exterior nodes that lie on the physical domain boundaries that may experience convective, radiative, or adiabatic heat fluxes, or for interior nodes that experience internal heat generation, the control volume approach is a more intuitive way to derive the finite differencing equations.

In order to derive finite difference equations via the control volume approach, the assumption must be made that heat flows into the node of interest since it is often unknown which direction the heat will flow. For the explanation of the approach, we will be considering two-dimensional steady-state conduction of an inside corner node with convection at the outer surfaces,

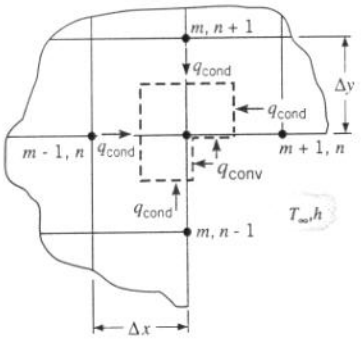

Figure 25: Control volume representation of an internal corner of a solid with surface convection. From [85], page 177.

internal energy generation, and conduction on the interior as shown in Figure 25. The general energy balance for steady-state conditions with internal energy generation is given in Equation [16], where, the rate of energy entering the control volume and the rate of energy generated in the control volume are shown in Equations [17] and [18].

$$\dot{E}_{in} + \dot{E}_g = 0 \qquad [\ 16\ ]$$

$$\begin{aligned} \dot{E}_{in} &= \sum_{i=1}^{4} q_{i\to m,n} + q_{\infty\to m,n} \\ &= q_{m,n+1\to m,n} + q_{m+1,n\to m,n} + q_{m,n-1\to m,n} + q_{m-1,n\to m,n} + q_{\infty\to m,n} \end{aligned} \qquad [\ 17\ ]$$

$$\dot{E}_g = \dot{q}V \qquad [\ 18\ ]$$

Even though we are deriving finite difference equations for a two dimensional problem, we only consider heat flow along the "lanes" between the central node *m, n* and its surrounding nodes; therefore, Fourier's Law can be used to approximate the heat flux along these lanes as shown in Equation [19]. The coefficient *A* is the area normal to the direction of heat flow, in reference to Equation [19] and Figure 25, $A = \Delta x \cdot 1$. The temperature gradient is taken to be in the direction of heat flow. Also, the thermal conductivity, *k*, is assumed to be independent of temperature.

$$q_{m,n+1\to m,n} = kA\frac{dT}{dy} \qquad [\ 19\ ]$$

Using the forward difference approximation to the temperature gradient shown in Equation [9] we obtain the finite difference approximation of Fourier's Law in reference to the lane $(m,n+1)\to(m,n)$ as Equation [20].

$$q_{m,n+1\to m,n} = k\cdot(\Delta x\cdot 1)\frac{T_{m,n+1} - T_{m,n}}{\Delta y} \qquad [\ 20\ ]$$

A similar approach can be taken with the remaining terms shown in Equation [17]; the resulting finite difference equations are shown in **Table VI**. Typically, a square element geometry is used, that is $\Delta x = \Delta y$. Summing the equations in **Table VI**, the complete finite difference equation for an internal corner node with surface convection is shown in Equation [21]. Each node in the physical domain will have it's own finite difference equation which will depend on it's location (on a free surface or interior) and what boundary conditions are applied. Finite difference equations for various geometries and boundary conditions are contained in Reference 85. Also shown in **Table VI** is the local numbering scheme used to simplify the equations when used in a computer program. This will be referred to in a later section.

Table VI: Summary of finite difference heat flux equations for an internal corner node with convection.

Lane	*Local Node Number*	*Area*	*Heat Flux*
m, n+1	1	$\Delta x \cdot 1$	$k \cdot (\Delta x \cdot 1)\frac{T_{m,n+1} - T_{m,n}}{\Delta y}$
m+1, *n*	2	$\frac{\Delta y}{2} \cdot 1$	$k \cdot \left(\frac{\Delta y}{2} \cdot 1\right)\frac{T_{m+1,n} - T_{m,n}}{\Delta x}$
m, *n-1*	3	$\frac{\Delta x}{2} \cdot 1$	$k \cdot \left(\frac{\Delta x}{2} \cdot 1\right)\frac{T_{m+1,n} - T_{m,n}}{\Delta y}$
m-1, *n*	4	$\Delta y \cdot 1$	$k \cdot (\Delta y \cdot 1)\frac{T_{m-1,n} - T_{m,n}}{\Delta x}$
Fluid	-	$\left(\frac{\Delta x}{2} + \frac{\Delta y}{2}\right) \cdot 1$	$h\left(\frac{\Delta x}{2} + \frac{\Delta y}{2}\right) \cdot 1\left(T_\infty - T_{m,n}\right)$

$$T_{m,n+1} + T_{m-1,n} + \tfrac{1}{2}\left(T_{m+1,n} + T_{m,n-1}\right) - \left(3 + \frac{h\Delta x}{k}\right)T_{m,n} + \frac{h\Delta x}{k}T_\infty + \frac{\dot{q}\Delta x^2}{k} = 0 \qquad [\ 21\ ]$$

With each node having an assigned finite difference equation, a system of equations (Equation [22]) can be established so that each unknown temperature, $\{T\}$, can be solved for, using a matrix of coefficients, $[K]$, and known boundary conditions, $\{F\}$ to give the approximate temperature distribution in the physical domain.

$$[K]\{T\} = \{F\} \qquad [\ 22\ ]$$

The finite difference principles outlined for steady-state heat conduction problems are the basis for developing approximations for transient and non-linear heat conduction problems. Each of these topics will be discussed in the forthcoming sub-sections.

Transient Finite Differencing

There are several finite difference schemes available to compute approximate solutions to transient heat conduction problems. The simple explicit (forwards difference), simple implicit (backwards difference), and Crank-Nicolson are three of the more common finite difference schemes, and will be discussed here. In the derivation of equations for steady-state heat conduction, the control volume approach was used. For the transient case, only the finite differencing of an interior node will be considered; therefore a more general mathematical

approach will be followed. The control volume approach for transient finite differencing will be demonstrated in the Experiment section relating to the thermal model.

Simple Explicit (Forward Difference)

We begin the discussion of transient heat conduction using Equation [23] which describes two dimensional transient conduction with no applied loads (convection, heat generation, radiation).

$$\frac{\partial^2 T}{\partial x^2} + \frac{\partial^2 T}{\partial y^2} = \frac{\rho C_p}{k}\frac{\partial T}{\partial t} \qquad [\ 23\ ]$$

In order to solve Equation [23] we must discretize both the spatial and temporal derivatives. The spatial derivatives are the same as in the steady-state case (Equation [14]). The temporal derivative for the central node (m,n) is given in Equation [24], where the superscript p is used to designate temperature at the current time step and p+1 is the next (future) time step.

$$\left.\frac{\partial T}{\partial t}\right|_{m,n} \approx \frac{T_{m,n}^{p+1} - T_{m,n}^{p}}{\Delta t} \qquad [\ 24\ ]$$

Assembling these components gives Equation [25], the *explicit* or *forward* finite difference equation for two-dimensional heat conduction, where the finite-difference form of the Fourier number is given by Equation [26].

$$T_{m,n}^{p+1} = Fo\left(T_{m+1,n}^{p} + T_{m,n+1}^{p} + T_{m-1,n}^{p} + T_{m,n-1}^{p}\right) + \left(1 - 4Fo\right)T_{m,n}^{p} \qquad [\ 25\ ]$$

$$Fo = \frac{k\Delta t}{\rho C_p \Delta x^2} \qquad [\ 26\ ]$$

Equation [25] is called *explicit* or *forward difference* because we are calculating the unknown temperatures in the future ($p+1$) using known nodal temperatures as illustrated in Figure 26. Calculations begin with initially known temperatures at t=0 (p=0) and solving for temperatures $t=(p+1)\Delta t$. The time step is marched in this fashion and the transient behavior is calculated. Accuracy of the solution can be improved by reducing the spatial increment (Δx, Δy) or time increment (Δt), however there is a significant computational cost.

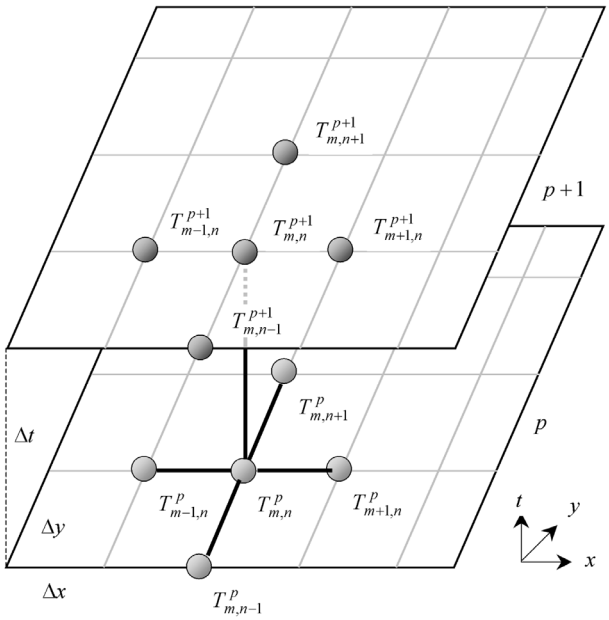

Figure 26: Finite difference molecules for the simple explicit scheme. The known temperatures at node (m,n) and it's surrounding nodes at time step p are used to calculated the unknown temperature at the time step p+1. Bold lines joining the molecules highlight the nodes involved in the calculation.

In the simple explicit method, the time increment must be kept below a certain value in order maintain stability of the solution. If too large a time step is used, the solution may begin to oscillate causing the solution to diverge from the correct solution. The stability criterion is determined from the coefficient of the $T^{p}_{m,n}$ term. Specifically the coefficient must be greater than or equal to zero as in Equation [27].

$$\left(1-4Fo\right)\geq 0 \text{ or } \Delta t \leq \frac{\rho C_p \Delta x^2}{4k} \qquad [\ 27\ ]$$

The significance of the criterion on a computational level is that if the mesh were refined to be half of the original, the maximum time step would have to be quartered, resulting in 4 times as many times steps need to get to an equivalent time with the original mesh. In addition twice as many computations must be made because the mesh was halved, giving an 8-fold increase in the amount of computational time required for a solution.

Lastly, further restrictions may be placed on the time step if certain boundary conditions are imposed. For example, for a surface node with convection, the coefficient of the $T^{p}_{m,n}$ term is $\left(1-4Fo-2BiFo\right)$, where Bi is the Biot number, $\frac{h\Delta x}{k}$. In order for the coefficient to be greater

than zero, Equation [28] must be true. The most stringent criteria should be used for the entire mesh.

$$Fo(2+Bi) \le \frac{1}{2} \text{ or } \Delta t \le \frac{\rho C_p \Delta x^2}{k(4+2Bi)} \qquad [\ 28\ ]$$

Simple Implicit (Backwards Difference) Method

In the explicit scheme, the temperature of a node (*m,*n) at time $t+\Delta t$ may be calculated from knowledge of temperatures at the same node (*m,n*) and surrounding nodes at time *t*. Thus, determination of nodal temperature at some time does not depend on the temperatures of the surrounding nodes at the same time. This is computationally simple to perform and the method is conditionally stable; however, a restriction on the size of the time step is required to ensure stability. Instead of discretizing the spatial derivatives at the time step *p*, they are discretized at the $p+1$ time step for the implicit method as shown in Equation [29].

$$T_{m,n}^{p} = (1+4Fo)T_{m,n}^{p+1} - Fo\left(T_{m+1,n}^{p+1} + T_{m,n+1}^{p+1} + T_{m-1,n}^{p+1} + T_{m,n-1}^{p+1}\right) \qquad [\ 29\ ]$$

In the implicit method, the new $p+1$ temperature of the node (*m,n*) depends on the new temperatures of the surrounding nodes, which are unknown unless they are prescribed boundary conditions as illustrated in Figure 27. This entails that the equations for every node must be solved simultaneously as shown in Equation [30], where [*K*], $[T^{p+1}]$, and $[T^{p}]$ are the coefficient, unknown and known temperature matrices, respectively.

$$\left\{T^{p+1}\right\} = [K]^{-1}\left\{T^{p}\right\} \qquad [\ 30\ ]$$

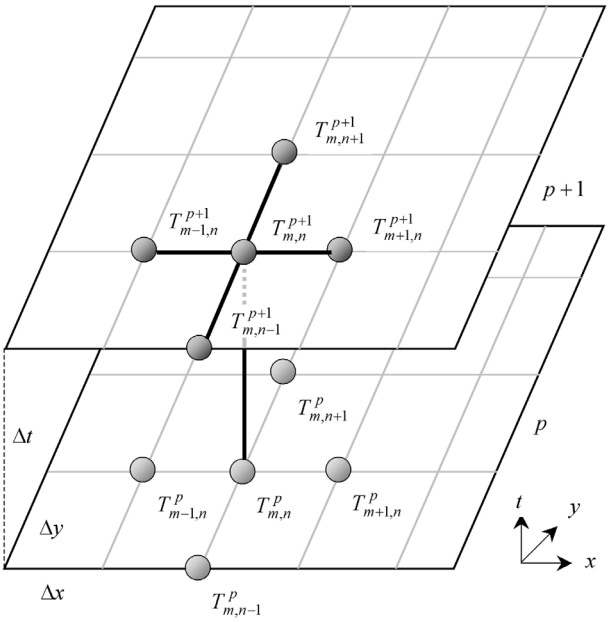

Figure 27: Finite difference molecules for the simple implicit scheme. The known temperature at node (*m*,*n*) for time step *p* and the unknown temperatures of the nodes surrounding (*m*,*n*) at time step *p*+1 are used to calculate the temperature at (*m*,*n*) at time step *p*+1. Bold lines joining the molecules highlight the nodes involved in the calculation.

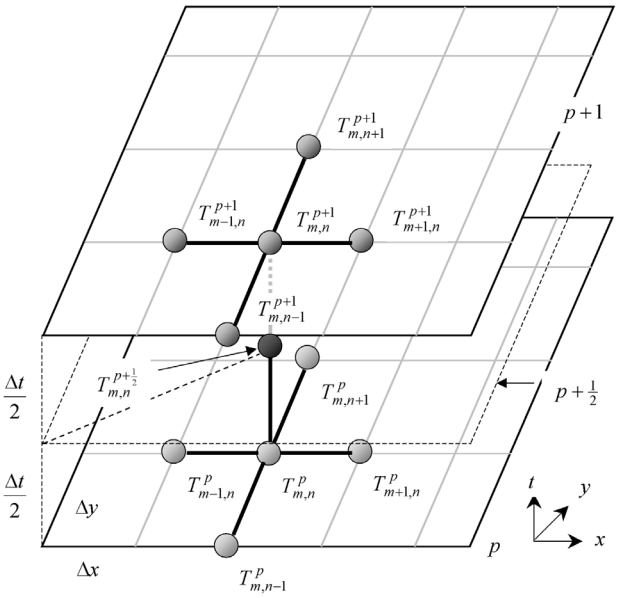

Figure 28: Finite difference molecules for the Crank-Nicolson scheme. The time derivative of Equation [31] is taken at the time step *p*+1 (black molecule). Surrounding nodes at both the *p* and *p*+1 time steps are used in the calculation of $T^{p+1}_{m,n}$.

Crank-Nicolson

The simple implicit method has been made more efficient without reverting to requirements on the time step to ensure stability. The Crank-Nicolson (C-N) method is one such method. The C-N method retains the same discretized temporal derivative as in the explicit and implicit methods, but uses the arithmetic average of the discretized spatial derivatives of the explicit and implicit method as shown in Equation [31]. The finite difference molecules for the C-N scheme are shown in Figure 28. One can think of the C-N scheme as taking the time derivative about the central (black molecule) at the time step $p+\frac{1}{2}$ in Figure 28.

$$\frac{T^{p+1}_{m,n}-T^{p}_{m,n}}{\Delta t}=\frac{1}{2}\frac{k}{\rho C_p}\left(\frac{T^{p+1}_{m-1,n}+T^{p+1}_{m+1,n}-2T^{p+1}_{m,n}}{\Delta x^2}+\frac{T^{p}_{m-1,n}+T^{p}_{m+1,n}-2T^{p}_{m,n}}{\Delta x^2}\right)+$$
$$+\frac{1}{2}\frac{k}{\rho C_p}\left(\frac{T^{p+1}_{m,n-1}+T^{p+1}_{m,n+1}-2T^{p+1}_{m,n}}{\Delta y^2}+\frac{T^{p}_{m,n-1}+T^{p}_{m,n+1}-2T^{p}_{m,n}}{\Delta y^2}\right) \qquad [\ 31\ ]$$

The C-N solution is second order accurate in both the spatial and temporal derivatives ($O[(\Delta t)^2,(\Delta x)^2]$) and, as in the implicit scheme, there is no stability restriction on the time step.

Nonlinear Heat Conduction

Temperature Dependent Properties

We begin our discussion with the temperature dependent version of Equation [23] shown in Equation [32]. Recall that the left hand side of Equation [32] is an energy transport term, thus the thermal conductivity varies with temperature spatially. The right hand side of Equation [32] is an energy storage term, therefore, the specific heat varies with temperature temporally.

$$k(T)\left(\frac{\partial^2 T}{\partial x^2}+\frac{\partial^2 T}{\partial y^2}\right)=\rho C_p(T)\frac{\partial T}{\partial t} \qquad [\ 32\ ]$$

Adding the temperature dependent properties, namely thermal conductivity and specific heat, is a fairly easy task provided we make some assumptions concerning how we calculate the thermal property for the next time step given that the temperature is unknown at the next time step. Özişik[80] proposes two methods to accomplish this task. In the first method, the thermal property is calculated at the temperature T^p and used in the calculation of the temperature T^{p+1} as illustrated in Equation [33] with thermal conductivity as an example. In other words the properties are lagging by one time step. Note the labeling convention to be used henceforth: k^p is equivalent to the thermal property evaluated at temperature T^p, i.e. $k(T^p)$.

$$k^{p+1}\approx k\left(T^p\right)=k^p \qquad [\ 33\ ]$$

Lagging temperature dependent properties by one time step is the least accurate method; however, approximate results can be obtained if the temperature gradient or time step is not too large. A more accurate approach is obtained by using an extrapolation method. The thermal property is approximated at the time step p+1 by expanding the thermal property at this time step as shown in Equation [34] for thermal conductivity.

$$k^{p+1}\cong k^p+\left(\frac{\partial k}{\partial t}\right)\Bigg|^p\Delta t\cong k^p+\left(\frac{\partial k}{\partial T}\right)\left(\frac{\partial T}{\partial t}\right)\Bigg|^p\Delta t \qquad [\ 34\ ]$$

Making the substitution for the temporal derivative at time step p we obtain Equation [35] for thermal conductivity and Equation [36] for heat capacity.

$$k_{m,n}^{p+1} \cong k\left(T_{m,n}^{p}\right)+\left(\frac{\partial k}{\partial T}\right)\Bigg|_{T=T_{m,n}^{p}}\left(T_{m,n}^{p}-T_{m,n}^{p-1}\right) \qquad [\ 35\ ]$$

$$C_{m,n}^{p+1} \cong C\left(T_{m,n}^{p}\right)+\left(\frac{\partial C}{\partial T}\right)\Bigg|_{T=T_{m,n}^{p}}\left(T_{m,n}^{p}-T_{m,n}^{p-1}\right) \qquad [\ 36\ ]$$

Recall Fourier's Law for heat conduction as illustrated in Equations [19] and [20] depends only on thermal conductivity, a transport property. Heat capacity and density enter the transient diffusion equation (Equation [23]) as energy storage terms. In temperature dependent form, the thermal conductivity depends on the central node and surrounding nodes at a given time step while the heat capacity depends only on the time step. Thus k^{p+1} should depend on the temperature of the central node and a specific surrounding node. The thermal conductivity between two nodes (e.g. (m,n) and (m,n+1)) can be estimated at any time p (known temperature) by taking the average thermal conductivity at each node as illustrated in Equation [37]. This is a reasonable approximation if the thermal property data is linear as is typical of thermal conductivity and the temperature difference between the central and surrounding nodes is small.

$$k_{(m,n+1)\to(m,n)}^{p}=\frac{k\left(T_{m,n+1}^{p}\right)+k\left(T_{m,n}^{p}\right)}{2}=k\left(\frac{T_{m,n+1}^{p}+T_{m,n}^{p}}{2}\right) \qquad [\ 37\ ]$$

To simplify Equation [37], we adopt a local node numbering convention for each surrounding node as in **Table VI**. Using this convention, the left hand side of Equation [37] becomes k_1^p.

Combining the temperature dependent thermal conductivity and heat capacity, we obtain the generalized temperature dependent form of Equation [26] in Equation [38], the finite difference form of the Fourier number. Notice that the specific heat enters the calculation as is shown in Equation [36].

$$Fo_i^{p+1}=\frac{k_i^{p+1}}{\rho C_i^{p+1}}\frac{\Delta t}{\Delta x^2}=\frac{k\left(\frac{T_{m,n+1}^{p}+T_{m,n}^{p}}{2}\right)}{\rho C_{m,n}^{p}}\frac{\Delta t}{\Delta x^2}=\frac{k\left(T_{m,n+1}^{p}+T_{m,n}^{p}\right)}{\rho C_{m,n}^{p}}\frac{\Delta t}{2\Delta x^2} \qquad [\ 38\ ]$$

The final temperature dependent form of the backwards difference equation for an interior node is shown in Equation [39]. The temperature independent version of the implicit finite difference equation is shown in Equation [29].

$$\begin{aligned}T_{m,n}^{p}=&-\left(Fo_1^{p+1}T_{m,n+1}^{p+1}+Fo_2^{p+1}T_{m+1,n}^{p+1}+Fo_3^{p+1}T_{m,n-1}^{p+1}+Fo_4^{p+1}T_{m-1,n}^{p+1}\right)+\\&+\left(Fo_1^{p+1}+Fo_2^{p+1}+Fo_3^{p+1}+Fo_4^{p+1}+1\right)T_{m,n}^{p+1}\end{aligned} \qquad [\ 39\ ]$$

Phase Change

Transient heat-transfer problems involving a phase change add a degree of complexity to the numerical solution. In particular, the position of the solid-liquid interface is not known *a priori* and must be determined as a part of the solution. This section serves to introduce the mathematical formulation[86] of the phase-change problem and highlight some of the techniques available to solve change of phase or Stefan problems. The only technique that will be discussed in detail will be the enthalpy method as it seems most applicable to the problem at hand.

One-dimensional solidification and melting problems are schematically illustrated in Figure 29 and Figure 30 and a schematic of the multi-dimensional solidification situation is illustrated in Figure 31. The solidification problem can be described as follows: a semi-infinite region ($0 \le x < \infty$) is initially at a temperature $T_i > T_m$, where T_m is the melting temperature. At time t = 0, the temperature at the boundary surface, x = 0, is lowered to $T_0 < T_m$ due to a heat flux in the negative x direction. As a result freezing begins at the boundary and the location of the solid-liquid interface $S(t)$ moves in the positive x direction as illustrated in Figure 29. The mathematical formulation of the one-dimensional change of phase problem is shown in Equations [40] and [41] for the solid and liquid phases assuming temperature independent material properties, heat transfer between the solid and liquid occurs by conduction, and ignoring convection in the liquid.

$$k_s \frac{\partial^2 T_s}{\partial x^2} = \rho_s C_s \frac{\partial T_s}{\partial t} \qquad [\ 40\ ]$$

$$k_l \frac{\partial^2 T_l}{\partial x^2} = \rho_l C_l \frac{\partial T_l}{\partial t} \qquad [\ 41\ ]$$

The energy balance for solidification is as follows: The rate of heat removed from the solid phase must equal the sum of the heat supplied from the liquid phase and the rate of heat liberated at the solid-liquid interface during solidification. This is mathematically shown in Equation [42] with L being the latent heat of solidification per unit mass and $S(t)$ is the position of the solid-liquid interface. In addition to Equation [42], the boundary condition that temperature of the solid and liquid equal the melting temperature at the solid-liquid interface must be imposed.

$$k_s \frac{\partial T_s}{\partial x} - k \frac{\partial T_l}{\partial x} = \rho_s L \frac{dS(t)}{dt} \qquad [\ 42\ ]$$

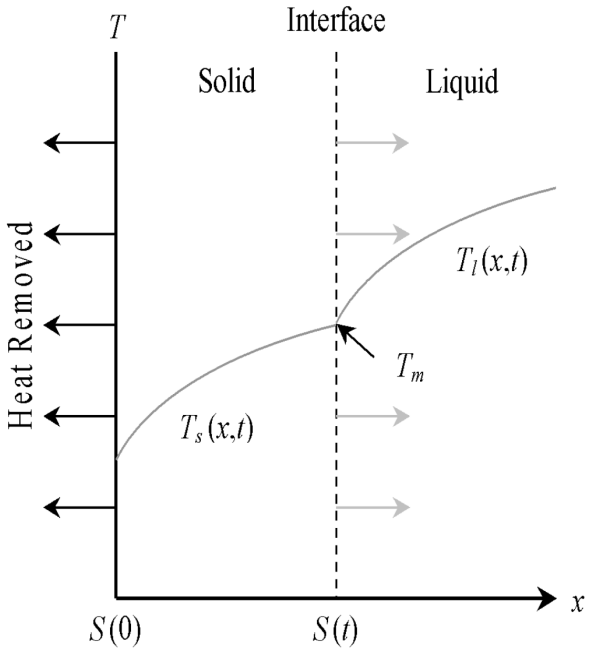

Figure 29: One-dimensional solidification. After [80] p. 277.

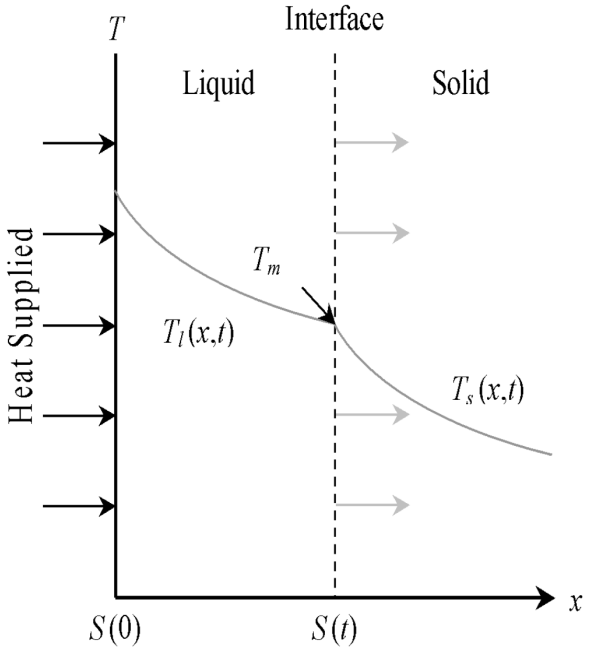

Figure 30: One-dimensional melting. After [80] p. 277.

The assumption made above that heat transfer in the liquid occurs by conduction severely limits the exactness of the numerical solution especially in problems where the velocity of fluid is very high, as in welding processes. If Equation [42] is manipulated to neglect heat transfer by conduction in the liquid phase, but consider convective heat transfer in the liquid phase, Equation [43] is obtained where h is the heat transfer coefficient and T_∞ is the bulk fluid temperature.

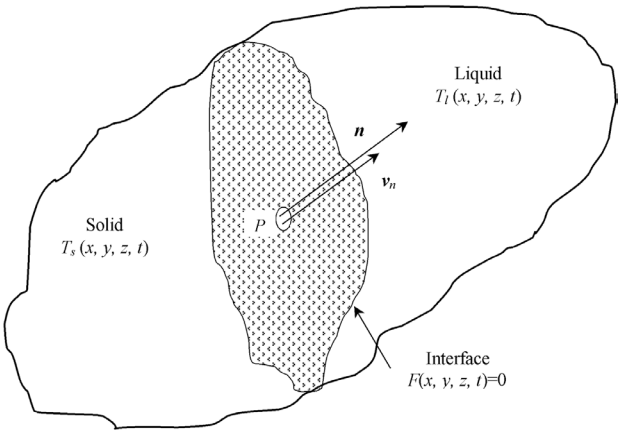

Figure 31: Solidification in three dimensions showing the solid liquid interface moving in the direction n with velocity v_n. After [86], p. 398.

$$k_s \frac{\partial T_s}{\partial x} - h\left(T_\infty - T_m\right) = \rho L \frac{dS(t)}{dt} \qquad [\ 43\ ]$$

The interface boundary conditions can be extended to the multi-dimensional case (Figure 31). Let the solid-liquid interface be defined by Equation [44].

$$F(x, y, z, t) = 0 \qquad [\ 44\ ]$$

If the densities of the solid and liquid are assumed to be equal, the boundary conditions on the interface become Equations [45] and [46] where $\partial/\partial n$ denotes derivatives along the direction of the vector ***n*** normal to the solid-liquid interface and v_n is the velocity of the interface at the location *P* in the direction ***n***.

$$T_s(x,y,z,t) = T_l(x,y,z,t) = T_m \quad \text{at } F(x,y,z,t) = 0 \qquad [\,45\,]$$

$$k_s \frac{\partial T_s}{\partial n} - k_l \frac{\partial T_l}{\partial n} = \rho L v_n \qquad [\,46\,]$$

An alternative two-dimensional form of these equations suitable for numerical solution is shown in Equations [47] and [48].

$$F(x,z,t) = z - S(x,t) \qquad [\,47\,]$$

$$\left(1 + \left(\frac{\partial S}{\partial x}\right)^2\right)\left(k_s \frac{\partial T_s}{\partial z} - k_l \frac{\partial T_l}{\partial z}\right) = \rho L \frac{dS}{dt} \quad \text{at } z = S(x,t) \qquad [\,48\,]$$

There exist several methods to solve change of phase problems by finite difference and other numerical methods. Özişik[80] lists five categories of finite difference techniques used to solve problems involving a change of phase. They are as follows:

i. *Fixed Grid Methods* in which the space and time domains are subdivided into equally spaced increments, Δx, and Δt. These increments remain constant; therefore, it is possible that the moving solid-liquid interface will lie between two spatial grid points at any given time.

ii. *Variable Grid Methods* in which either the space **or** time domain is subdivided into equally spaced increments such that the increment of the remaining domain is selected such that solid-liquid interface falls on a grid point at each time step. For example, if equal time steps are chosen, the number of space intervals (number of elements) is kept constant and the size of the element (Δx) may be selected such that interface falls on a node during each time step. Conversely, the space increment can be fixed and the time increment varied.

iii. *The Front Fixing Method* is used in one-dimensional problems and essentially a coordinate transformation scheme that immobilizes the moving solid liquid interface hence eliminates the need for tracking the moving interface. The numerical solution becomes more complicated as a result.

iv. *The Adaptive Grid Generation Method* is useful for solving multidimensional moving boundary problems in bodies having irregular shape. Numerical grid generation is applied to map the irregular region to a regular region in the computational domain where the problem is solved and the results transformed back to the physical domain. A considerable amount of computer time is required since the grid is generated at each time step.

v. *The Enthalpy Method* is useful in that it can be applied to problems where the change of phase takes place over an extended temperature range as in alloys or amorphous substances.

The discussion on phase-change problems will conclude with the underlying theory behind the enthalpy method and an example of an implicit finite difference technique employed to solve problems involving solidification of an alloy. In the enthalpy method, the enthalpy function, $H(T)$, is used as a dependent variable along with temperature as shown in Equation [49]. Equations [42] through [48] assume that the energy associated with the liquid and solid phases are coupled through the energy balance condition, requiring that the solid-liquid interfaces be tracked. In the enthalpy method, a single energy equation becomes applicable for both phases and the solution is greatly simplified. Both finite difference and finite element techniques may be employed using the enthalpy method.

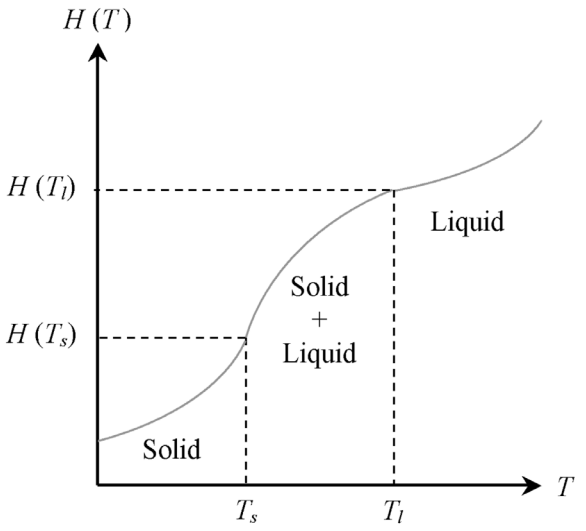

Figure 32: Enthalpy function $H(T)$ for an alloy or amorphous substance.

$$\nabla \cdot (k \nabla T) = \rho \frac{\partial H(T)}{\partial t} \qquad [49]$$

The enthalpy function for an alloy is shown schematically in Figure 32 and mathematically in Equations [50], [51], and [52]. Note that in a pure substance, there is no two phase solid and liquid region (mushy region), resulting in a discontinuity in the enthalpy function at T_{melt}.

$$H = C_p T \qquad \text{for} \qquad T < T_{solid} \qquad [50]$$

$$H = C_p T + \frac{T - T_{solid}}{T_{liquid} - T_{solid}} \qquad \text{for} \qquad T_{solid} \le T \le T_{liquid} \qquad [\ 51\ ]$$

$$H = C_p T + L \qquad \text{for} \qquad T > T_{liquid} \qquad [\ 52\ ]$$

The corresponding relations for the temperature as a function of enthalpy is shown mathematically in Equations [53], [54], and [55].

$$T = \frac{H}{C_p} \qquad \text{for} \qquad H < C_p T_{solid} \qquad [\ 53\ ]$$

$$T = \frac{H\left(T_{liquid} - T_{solid}\right) + L T_{solid}}{C_p\left(T_{liquid} - T_{solid}\right) + L} \qquad \text{for} \qquad C_p T_{solid} \le H \le \left(C_p T_{liquid} + L\right) \qquad [\ 54\ ]$$

$$T = \frac{H - L}{C_p} \qquad \text{for} \qquad H > \left(C_p T_{liquid} + L\right) \qquad [\ 55\ ]$$

The mathematical formulation of Equation [49] for a one dimensional solidification problem is given in Equation [56] and its corresponding implicit finite difference equation is given by Equation [57].

$$k \frac{\partial T^2}{\partial x^2} = \rho \frac{\partial H(T)}{\partial t} \qquad [\ 56\ ]$$

$$k \frac{T_{i-1}^{p+1} - 2T_i^{p+1} + T_{i+1}^{p+1}}{\Delta x^2} = \rho \frac{H_i^{p+1} - H_i^p}{\Delta t} \qquad [\ 57\ ]$$

The solution of Equation [57] for the enthalpy at the time step p+1 is shown in Equation [58] where the notation $T = F^*(H)$ denotes that the temperature is a function of enthalpy as given by Equations [53], [54], and [55]. The vector form of Equation [58] is shown in Equation [59] with $\mathbf{F}_i\left(\mathbf{H}^{p+1}\right)$ defined in Equation [60].

$$H_i^{p+1} = H_i^p + \frac{k\Delta t}{\rho \Delta x^2}\left(F^*\left(H_{i-1}^{p+1}\right) - 2F^*\left(H_i^{p+1}\right) + F^*\left(H_{i+1}^{p+1}\right)\right) \qquad [\ 58\ ]$$

$$\mathbf{G}\left(\mathbf{H}^{p+1}\right) \equiv \mathbf{H}^p + \Delta t \mathbf{F}\left(\mathbf{H}^{p+1}\right) - \mathbf{H}^{p+1} = 0 \qquad [\ 59\ ]$$

$$\mathbf{F}_i(\mathbf{H}) = \frac{k}{\rho \Delta x^2}\left(F^*\left(H_{i-1}\right) - 2F^*\left(H_i\right) + F^*\left(H_{i+1}\right)\right) \qquad [\ 60\ ]$$

The above equations can be used to solve for the enthalpy of node i at the time step p+1 using known temperatures and thus known enthalpies at time step p for node i and surrounding nodes (i-1) and (i+1). In order to solve the set of non-linear equations described in Equations[58], [

59], and [60] an iterative scheme[87] such as Newton's Method[88] is needed to determine the enthalpy of the next time step, $\mathbf{H}^{p+1}$. First, and initial guess is made for $\mathbf{H}^{p+1}$ from known temperatures and enthalpies from time step p as shown in Equation [61], where the integer k represents the k^{th} iteration, $\mathbf{H}_i^p$ and $\mathbf{F}_i\left(\mathbf{H}_i^p\right)$ are defined by Equations [50] through [52] and [60], respectively.

$$\mathbf{H}_i^{p+1,k=0} = \mathbf{H}_i^p + \Delta t \mathbf{F}_i\left(\mathbf{H}_i^p\right) \qquad [\ 61\ ]$$

Newton's Method is employed to calculate the next iteration, k+1, as in Equation [62], where $\mathbf{H}_i^{p+1,k}$ is defined as Equation [61], ω is a relaxation factor, $\mathbf{G}\left(\mathbf{H}_i^{p+1,k}\right)$ is defined as Equation [59] and $\mathbf{G}'\left(\mathbf{H}_i^{p+1,k}\right)$ is defined below as Equation [63].

$$\mathbf{H}_i^{p+1,k+1} = \mathbf{H}_i^{p+1,k} - \omega \frac{\mathbf{G}\left(\mathbf{H}_i^{p+1,k}\right)}{\mathbf{G}'\left(\mathbf{H}_i^{p+1,k}\right)} \qquad [\ 62\ ]$$

$$\mathbf{G}'\left(\mathbf{H}_i^{p+1,k}\right) = \Delta t \frac{\partial \mathbf{F}_i\left(\mathbf{H}_i^{p+1,k}\right)}{\partial \mathbf{H}_i^{p+1,k}} - \mathbf{I} \equiv \mathbf{J} - \mathbf{I} \qquad [\ 63\ ]$$

The **I** term is the identity matrix and **J** is the Jacobian matrix whose components are given by Equation [64].

$$\mathbf{J}_{ii} = \Delta t \frac{\partial F_i}{\partial H_i}\bigg|_{\mathbf{H}=\mathbf{H}_i^{p+1,k}} \qquad [\ 64\ ]$$

The equation for the determination of the i^{th} component of enthalpy becomes Equation [65].

$$H_i^{p+1,k+1} = H_i^{p+1,k} + \omega \frac{H_i^{p+1,k} - H_i^{p+1,k} + \Delta t F_i\left(\mathbf{H}^{p+1,k}\right)}{1 - J_{ii}} \qquad [\ 65\ ]$$

The algorithm to solve the solidification problem must be such that the position of the solid-liquid interface is defined iteratively in such that it always moves a distance Δx. The algorithm for solving the implicit one-dimensional solidification problem is given below.

1) Let Δt_i be the time step where the interface moves one spatial increment, Δx. First, an initial guess for the size of the time step Δt_k^0 is taken as $\Delta t_i^0 = \Delta t_{i-1}$.

2) The enthalpy distribution $\mathbf{H}^{t+\Delta t_i^m}$, where the superscript m on Δt refers to the m^{th} iteration on the time step, is determined from the solution of Equations [61] and [65]. The m^{th} time step is computed using an iterative scheme given by Equation [66] where ω^* is the relaxation parameter associated with the time step.

$$\Delta t_i^{m+1} = \Delta t_i^m + \omega^* \Delta t_i^m \left(\frac{H_{i+1}^{t+\Delta_i^m}}{CT_{melt} + (L/2)} - 1 \right) \qquad [\ 66\ ]$$

3) When the value of $H_{i+1}^{t+\Delta_i^m}$ converges to $CT_{melt} + (L/2)$, the corresponding enthalpy values at all nodes are considered to be the solution for the time $t + \Delta t_i^m$.

4) Once the enthalpy values are available at the nodes, the corresponding values of node temperatures T_i are determined from the enthalpy function in Equations [53] through [55].

5) The extent of the "mushy" zone, or *x*-position of the solidus boundary, x_s, can be found[87] by an interpolation on the temperature distribution at time $t = p\Delta t$ from Equation [67] where *S* is the position of the last node in the solid.

$$x_s = \left(S + \frac{T_S^p - \frac{1}{2}\left(T_{liquid} - T_{solid}\right)}{T_S^p - T_{S+1}^p} \right) \Delta x \qquad [\ 67\ ]$$

Summary

The numerical methods presented within are to serve as an outline for the derivation of a set of finite difference equations to model the thermal history in the Laser Forming process. A more mathematical approach was taken above in order to demonstrate the basic principles of the finite difference method; however, it should be noted that as the boundary conditions become more numerous and complex, it becomes conceptually easier to derive finite difference equations based on the control volume approach. This is demonstrated in the Appendix for the problem at hand. Also, the introduction on phase change problems is quite extensive even though it will not be considered in the model or in the results. Its presence is important, however, as the topic of phase change will resurface in the Future Work sections of this thesis.

Chapter 2:

Literature Review / Introduction

DMD of Titanium

Early papers on the direct metal deposition of titanium were concerned with the development of AeroMet's Laser Forming process and "selling" the process to industry. As a result, the papers mainly dealt with material properties, quality of the parts produced, and economic advantages of the process. The evolution and understanding of microstructure was largely neglected. There was one exception out of the papers published on AeroMet's process. In a paper by Arcella and Whitney[89], et. al., electron microprobe analyses were performed on LaserCast† ingots of Ti-6Al-4V fabricated using pre-alloyed and blended elemental powders. Titanium, aluminum, and vanadium concentrations were constant along a 1 mm length (*z*-direction) on the centerline of the build. For reference, each fused layer was approximately 0.5 mm thick and data points were measured every 0.25 mm.

It is worth noting here that several papers[67,68,89,90] on the Laser Forming of Ti-6Al-4V by those affiliated with AeroMet report mechanical properties at or above levels required for traditional cast or wrought Ti-6Al-4V.

More recently, Kobryn, et. al.,[91,92,93] have explored the effect of process parameters on the build characteristics (porosity, build height) and microstructural features (prior beta grain width). Two different DMD systems were used, LENS (Nd-YAG, 0.5 – 1.2 kW), and ARL‡ (CO_2, 14 kW). The conclusions regarding the effect of laser velocity on build characteristics and are that porosity, layer height, and prior beta grain width decrease as laser velocity increases. The columnar beta grain width was also shown to decrease with an increase in incident energy (laser power / laser velocity). The use of the Nd:YAG laser resulted in a fine Widmanstätten microstructure and discontinuous α at prior beta grain boundaries indicating a rapid cooling rate. The microstructure of material deposited with the CO_2 laser had a coarser Widmanstätten morphology with continuous α prior beta grains indicating a slower cooling rate. Slow cooling rates are a result of high incident energy (high power and low speed); conversely, low laser power and high velocity result in fast cooling rates. Layer bands were also observed in their results[92,93] and described by the authors as a sudden change in the number of equiaxed α particles in the Nd:YAG builds and a change in the coarseness of the Widmanstätten structure in

† LaserCast later became AeroMet's LaserForming
‡ Applied Research Lab, Penn State; same laser system as AeroMet

the CO_2 builds. The reason given for the presence of the layer bands is that a new heat affected zone forms each time a new layer is deposited. No further analysis or proof of this theory is given.

Kobryn and Semiatin[91,93] also performed limited experiments to deduce the microstructural evolution DMD Ti-6Al-4V. To this end, single pass laser glazes (no metal deposition, just laser heating) and Finite Element Method simulations of single pass laser glazes were made at different levels of incident energy and the heat affected and fusion zones of the experimental glazes compared with the FEM results. The resulting thermal gradients, G, and solidification rates, R, were plotted on a Ti-6Al-4V solidification map. The CO_2 laser glaze (R = 0.4 cm/s, G = 900 K/cm) was predicted to have a mixed columnar and equiaxed prior beta grain morphology while the Nd:YAG glaze (R = 0.7 cm/s, G = 11000 K/cm) was predicted to have a fully columnar morphology. The results of the thermal model are interesting, but are not encompassing as they do not consider the deposition of multiple layers of material. The thermal gradients and solidification rates are bound to change as multiple layers are added.

DMD Thermal Behavior

The people involved with the LENS process, namely Optomec and Sandia national Labs have greatly advanced the understanding of DMD processes, from the effect of process parameters on build characteristics and microstructural evolution to *in situ* process measurements and feedback control. Like AeroMet's process, early work on the LENS process[94, 95] included influence of processing parameters on build characteristics (porosity, surface finish, mechanical properties, and build height). The dimensional aspects of these characteristics (build height, surface finish) are of particular importance because the end result of the LENS process is a net-shape part, i.e., no machining desired.

More recently, investigations have been made into the solidification behavior that occurs during the LENS deposition of 316 stainless steel and H13 tool steels. The thermal behavior of the melt pool is of importance because the thermal gradients and cooling rates they control the morphology of the first solid to form and thus the properties of the sample. If one knows the temperature profile in the melt pool, with the proper equipment and feedback loop, the process can be controlled to give a desired melt pool shape, and therefore control microstructural features by-wire.

Hofmiester, et.al.,[78,79] examined the melt pool temperature profile in LENS 316 SS builds using a high speed thermal imaging techniques. The resulting image gives temperature of the melt pool as a function of temperature and time. The effect of process parameters on melt pool temperature profiles was examined. It was shown that the molten pool size increases with laser power up to a certain point whereupon an increase in power raises the temperature of the melt pool and has little effect on the melt pool size. As incident energy increases, the separation between the liquidus and solidus isotherms also increases. Also, higher power causes heating in previously deposited layers resulting in reduced cooling rates in the solid. At the solid liquid interface, cooling rates are higher at low power levels because the melt pool is small. As the laser power increases, the quench rate at the solid liquid interface reaches a constant value on of approximately 10^3 K/s; however, in the solid an increase in laser power will continue to decrease the cooling rate. The resulting solidification structures were finer for the low power builds as a result of the high cooling rate.

Griffith, et. al.,[77,96] examined the thermal behavior in LENS deposited H13 tool steel. In the experiment, fine diameter thermocouples were placed at various heights in the single line build of a box. The temperature excursion experienced at this fixed point in the build was recorded and used to describe the evolution of microstructure in the build. It was determined that the last layer to be deposited exhibited segregation due to partitioning during solidification. A region further below in the build experiences cycling in a temperature range where martensite that has formed during the initial deposition decomposes into ferrite, austenite, and carbides. The initial layers deposited experience cycling in a sub-critical region where precipitation and coarsening of alloy carbides occur. A kinetic model was developed to predict the hardness from the thermal behavior measured with the *in situ* thermocouples. This research shows the necessity of temperature data, be it experimental or modeled, for predicting microstructural evolution.

DMD Thermal Modeling

In conjunction with thermal imaging work of 316SS, Hofmeister, et. al.,[78] performed finite element modeling using birthing techniques to simulate the deposition of a thin wall of material (~60 layers). In the element birthing scheme, an element is deposited or birthed having a set temperature. Two temperatures, $T = T_{melt} = 1377°C$ or $T = T_{superheat} = 1627°C$ were used as the initial temperatures for a birthed element. Only conduction was considered in the model and

a constant substrate temperature was used (thermocouple data indicates that when the build is 5 layers high, a steady state temperature of 300°C is attained).

Out of a need to understand how processing parameters control residual stress while maintaining optimum depositions conditions, Bueth, et. al.,[97] developed a process map (dimensionless plots) for the LENS process. The maps can be used to relate processing variables to build characteristics for any thin-walled structure. The results demonstrate how melt pool length can be controlled as a function of wall height, incident energy, laser velocity, and substrate preheat temperature for temperature independent and temperature dependent properties. The model considers conductive heat flow, and considers a moving point heat source. The results of the process map are that melt pool size is dominated by changes in laser velocity and power, and not affected much by substrate temperature. The fact that the substrate can be heated without affecting solidification is promising in that preheating can be used to control residual stress development in the build. It was also observed that for the initial layers deposited, the melt pool size is greatly reduced. Beuth and Klingbeil[98] have also considered process maps for thermal gradient (dT/dz) which is directly related to the residual stress.

Directions for This Research

There are three aspects of the current research: (1) heat treatment of Laser Formed Ti-6Al-4V; (2) examination of the as-deposited microstructure in Laser Formed Ti-6Al-4V; (3) modeling of the Laser Forming DMD process. The literature suggests a clear need for further research in these areas. The heat treatment phase of the research is needed to qualify the Laser Forming process for the aerospace industry, i.e., proving that heat treated Laser Formed material has the same properties as conventional wrought material. Characterization of the as-deposited material is also needed to qualify the process, but on a fundamental level, is also needed to understand how the microstructure evolves during the deposition process. Understanding of the microstructural evolution will aid in control of process parameters and the final properties of the part. For Ti-6Al-4V, it is clear that some understanding has been gained through the work of Kobryn and Semiatin; however, evidence is not present to support explanations for the presence of the evolution of microstructural features such as the layer band phenomena. In addition, examination of the solidification behavior in Laser Deposited Ti-6Al-4V has not been performed on multiple layered parts. As a result, there are significant gaps in the understanding of

microstructural evolution in DMD Ti-6Al-4V. Much work has been performed by those involved with the LENS process regarding microstructural evolution using experimental and modeling techniques for material systems other than titanium.

The research presented here will advance the understanding of microstructural evolution in Laser Forming of Ti-6Al-4V through characterization of the as-deposited material and thermal modeling. In its current form, the model focuses on thermal behavior after solidification whereas other models that have been developed for the LENS process focus on the melt pool and the effect of process parameters on melt pool characteristics. Both thermal cycling and solidification behavior must be examined in order to fully understand the effect of process parameters on microstructure development; however, solidification has been largely ignored here as the thermal model is still in its infancy. Since process parameter sets were not available for the as-deposited build or to use to model the Laser Forming process, an exhaustive study as to the effect of parameter sets on thermal behavior in the deposit was not explored. Instead, best-guess parameter sets were used based on published mass deposition rates for the Laser Forming process to demonstrate that the thermal model could be used to determine the thermal cycling in a multiple layer build. This information is used to determine the microstructural evolution in the Laser Forming of Ti-6Al-4V.

Chapter 3:

Experiment

As-Deposited Procedures

Laser Formed Coupons

The Laser Forming process and corresponding coordinate system are illustrated in Figure 33. Thirteen Laser Formed test coupons (Figure 34), labeled "B" through "N" were received from Boeing/AeroMet to undergo microstructural evaluation and heat treatment. The coupons were nominally 15 mm wide (*y*), 60 mm tall (*z*), and 65 mm long (*x*). Eighteen layers of Ti-6Al-4V, having a thickness of about 3 mm, were deposited on a 7 mm thick Ti-6Al-4V substrate that was previously mill-annealed at 700-730 °C for 2 hours. Each deposited layer was about 6 mm thick; however, due to overlap of the layers, each ripple seen in Figure 34 is about 3 mm thick. Processing parameters such as laser speed and power, mass deposition rate, preheat temperature, etc., associated with the as-deposited coupons were unavailable due to the proprietary nature of the process.

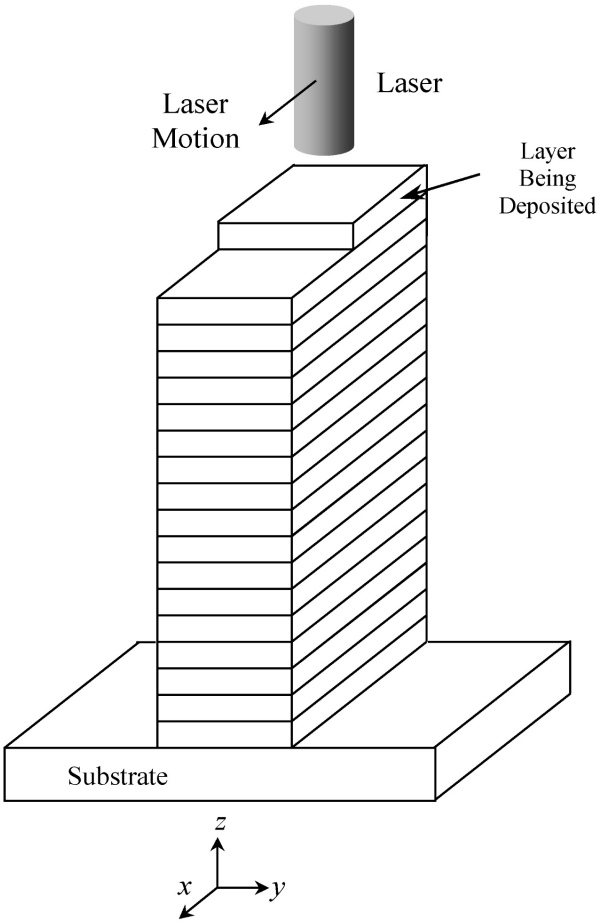

Figure 33: Geometry of a layer coupon showing the Laser Forming process coordinate system.

Metallographic Sample Preparation

Samples were cut along the *y*-*z* plane (Figure 33) from coupons B, E, H, and K to examine the as-deposited macro and microstructure. The *y*-*z* samples were also sectioned in the *x*-*z* and *x*-*y* planes. Sectioning was performed using a Struers Accutom-5 sectioning saw with

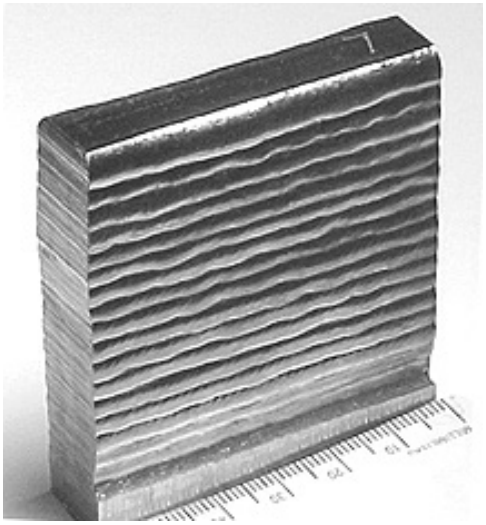

Figure 34: Single line Laser Formed Ti-6Al-4V coupons. Laser motion is horizontal, build height is bottom to top.

silicon carbide blade and cutting rates (< 0.04 mm/s) slow enough to not affect the microstructure. Heat-treated coupons were sectioned in the *y-z*. The *x-z* plane was examined in the as-deposited, but not the heat treated condition. The *x-y* plane was not examined.

Samples having a maximum dimension less than 32 mm were mounted in Bakelite. All of the heat-treated samples were left as *y-z* sections, having dimensions of 15 mm wide (*y*), 60 mm tall (*z*), and 3 mm thick (*x*). The larger samples were mounted to Bakelite blanks using a cyanoacrylate adhesive. The samples were removed from the blanks after polishing.

Samples were ground and polished on a Buehler AutoMet2/EcoMet3 polishing system. Rough grinding using 240, 340, 400, and 600 grit SiC grinding discs were used. The sample holder and wheel were rotated in the same direction (complementary) with wheel rotating twice as fast as the sample holder (240 RPM vs. 120 RPM). A pressure of 4 pounds per sample was applied over about 10 minutes for each grinding level. A one step final polish using colloidal silica (~0.06 μm particles) on a short nap cloth (PSI Final Finish Cloth) with a sample pressure of 3-6 pounds/sample was used. The sample holder and wheel rotated in opposite directions (contra) at the same speed (140 RPM). The final polish was performed for 8 minutes. For an additional 2 minutes, deionized water was slowly added to the cloth to clean both the sample and cloth.

A 5 vol.% hydrofluoric acid (HF) in deionized water solution was used as the etchant. Samples were submersed in a watch glass containing the etchant for approximately 10 seconds, rinsed in a beaker of deionized water, and then dried.

Microscopy

Macrostructural observation was performed on an Olympus SZH10 stereoscope. Microstructural evaluation was performed on an Olympus BH-2 optical microscope. A CCD camera attached to a PC running Image-Pro Plus image analysis software could be connected to either scope to record digital images. Images were calibrated and measurements made using either the Image-Pro Plus or Carnoy (www.carnoy.org) image analysis software. More specific details pertaining to the measurement of certain features are contained in the results section.

Hardness Measurements

Vickers macrohardness measurements were made on a Leco LV100. Macrohardness indentations were made applying a load of 20 kg for 10 seconds. Vickers microhardness measurements were made using Leco DM-400 hardness tester. Indentations were made using a 300-gram load applied for 10 seconds. The two diagonals of each indentation (both macro and micro) were measured three times, and the hardness for the particular location taken to be the average of the three measurements.

Electron Microprobe

A Cameca SX-50 Microprobe Analyzer was used to map the composition of the as received deposit. The Cameca SX-50 is a fully automated electron-beam instrument capable of semiquantitative and quantitative chemical analysis of areas as small as 1-3 μm^2 as well as routine surface scanning for back-scattered electron (BSE) and secondary electron (SE) characterization and imaging. The instrument is fitted with four multi-crystal wavelength-dispersive spectrometers (WDS) and a PGT energy-dispersive solid-state detector (EDS) that can work simultaneously. Quantitative analysis of elements N through U can be performed with detection limits as low as several hundred parts per million, depending on element.[†]

Line scans of various lengths and positions were performed to obtain a quantitative variation of aluminum, vanadium, and titanium in the as-deposited material. Line scans intersecting zero, one, and two layer bands were performed. The scan length, step distance, beam dimensions, and number of analyses performed per scan varied according to Table VII. A beam current of 20.1 nA and an acceleration voltage of 15 kV were used. Calibration of aluminum, vanadium, and titanium x-ray intensities were based on primary standards of kyanite

Table VII: Summary of Quantitative Microprobe Analyses

Feature Analyzed	Scan Length, *z*	Step Distance, Δz	Beam Dimensions	Number of Analyses
Layer Band	8.1 mm	50 μm	5x4 μm	163
	1.6 mm	20 μm	5x4 μm	80 x 3
Top of Part (Absent of Layer Band)	9.9	100 μm	10x8μm	100 x 3

[†] http://vtso.geol.vt.edu/eprobe/probe.html

(Al_2SiO_5), $YbVO_4$, and TiO_2, respectively. Aluminum, vanadium, and titanium were detected on thallium acid phthalate (TAP), lithium fluoride (LiF), and penta-erithrytol (PET) crystals, respectively. In the x-ray spectra for this alloy, the V-K_α and Ti-K_β peaks overlap. In order to accurately detect vanadium, the Ti-K_β peak was subtracted from the background of the V-K_α peak. Though not perfect, this technique seemed to work well, giving a nominal alloy composition of 90.4 wt.% Ti, 5.6 wt.% Al, and 2.8 wt.% V.

Heat Treatment Procedure

The vaccum heat treatment system (Centorr 16-5X10W-16) used in this research is shown schematically in Figure 35. Eleven laser formed Ti-6Al-4V coupons received the following heat treatment in: (1) a 2-hour solution treatment at 913°C, (2) a furnace-controlled cool down to 315°C at rates ranging from 0.3°C/min to 500°C/min, and (3) a 4-hour aging treatment at 538°C followed by a furnace cool. All thermal treatments were performed in a vacuum of 10^{-4} torr. A thermocouple located in the hot-zone next to the part measured the temperature throughout the heat treatment. Data is recorded on a computer, which is connected to the sample thermocouple/furnace controller.

Furnace System

The furnace system consists of a three-phase tungsten heating element housed in a double walled (water cooled) stainless steel chamber. The maximum temperature of the furnace is 1650°C. Temperature is monitored and controlled though a Process Setpoint Controller (PSC, Red Lion Controls) connected to a Type-C thermocouple located in the hot zone of the furnace. In order to obtain accurate temperature measurements in a vacuum, the hot-zone thermocouple (TC) should be placed in contact or if the diffusion bonding of the TC and sample are of concern, as close as possible without touching. The temperature of the stainless steel jacket is monitored by a Honeywell process controller connected to a Type-K thermocouple.

Vacuum System

The vacuum system consists of a Welch 1397 mechanical pump connected inline to a Varian diffusion pump. A thin coating of silicone high vacuum grease (Dow Corning) has been applied to all seals in the vacuum system. The main vacuum valve separates the chamber from the vacuum pumps. The chamber has two inlet ports located on the side and top of the chamber. There is also an outlet port to bleed off vacuum/pressure in the chamber. Three gauges are installed in the system to measure the level of vacuum. The first, a diaphragm gauge, reads both pressure and vacuum, but is mainly used a pressure gauge. A Teledyne-Hastings thermocouple gauge (DV-6) is used to read low vacuum while an ionization gage reads medium to high vacuum.

A typical procedure for bringing the furnace under vacuum suitable (< 10^{-4} Torr) for operation at high temperatures (>500°C) is as follows. After loading and positioning the sample in the chamber, the chamber is sealed and the bleed valve and one of the inlet valves are opened. The chamber, and more importantly, the cooling system is purged with inert gas for about 1 minute. With the chamber purged and sealed, the main vacuum valve is opened and the mechanical pump switched on. After the vacuum stabilizes (about 1 hour), the diffusion pump and ionization gauge are switched on. After 45 minutes, the system will have reached the maximum vacuum and the furnace may be switched on.

Quench System

The furnace controller was able to maintain a constant cooling rate up to 10°C/min

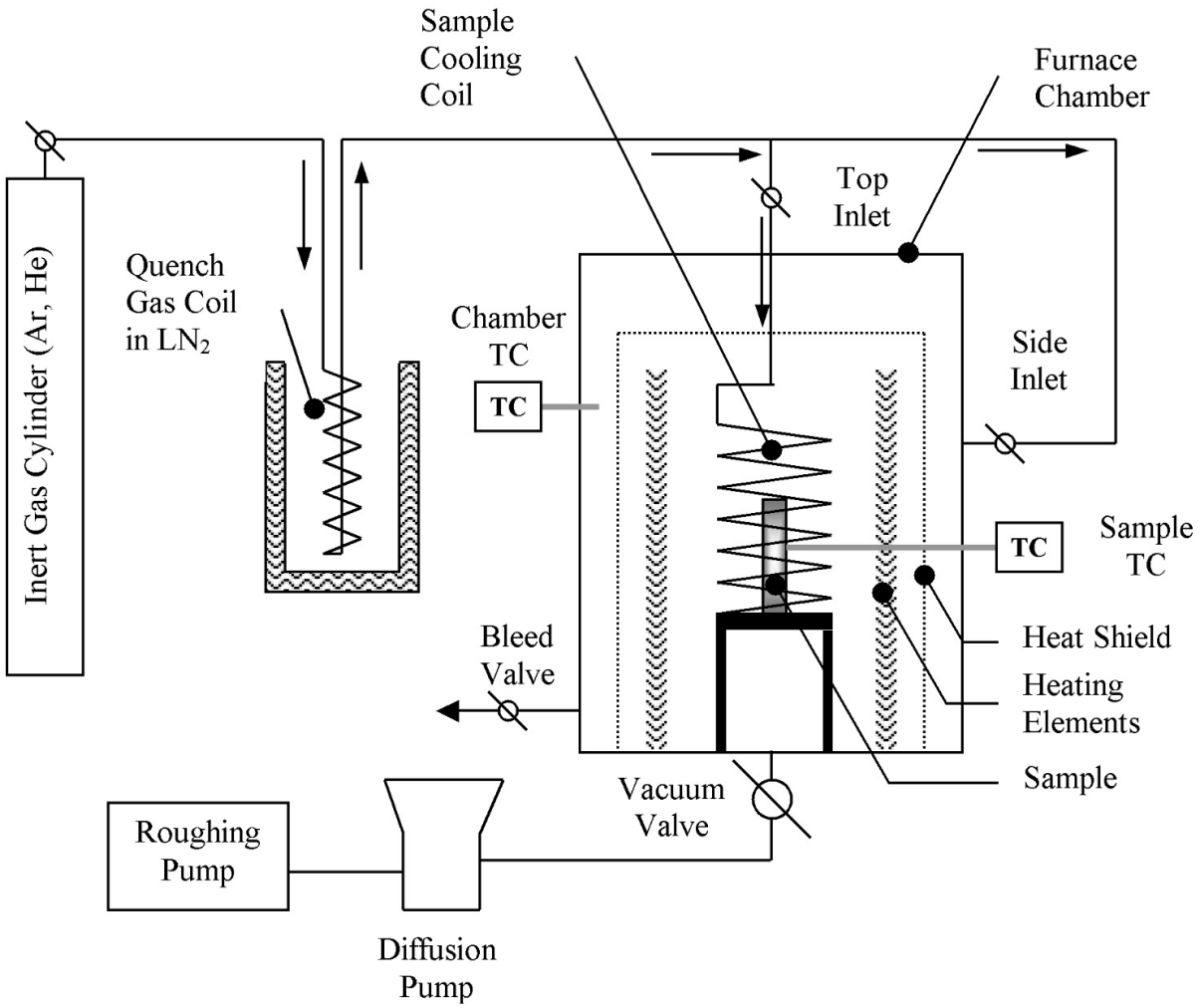

Figure 35: Vacuum heat treatment system used to heat treat the laser formed Ti-6Al-4V samples.

without the aid of a quench gas. Thus, heat treatments requiring cooling rates less than or equal to 10°C/min were cooled in a vacuum, whereas faster cooling rates required an inert quench gas of argon or helium. A cooling rate of about 50°C/min was attainable using argon at room temperature and a chamber pressure of 25 psi. Faster cooling rates were reached using argon or helium cooled to liquid nitrogen temperatures. For cooling rates between 10°C/min and 200°C/min the furnace controller can adjust the temperature in the hot zone as needed to maintain a relatively constant cooling rate. For cooling rates faster than 200°C/min, the only the flow rate and temperature of the quench gas controls the cooling rate.

An apparatus, quench gas coil (QGC), was constructed to cool the quench gas using liquid nitrogen. The apparatus consisted of 5/16 inch copper tubing wound into a coil that was submerged in a dewar of liquid nitrogen. The inlet of the coil was connected to the inert gas cylinder and a high-pressure regulator. The outlet of the coil was connected to two gas inlet ports on the vacuum chamber using nylon tubing. The two chamber inlet ports were located at the top and side of the chamber, with the top inlet port contained a tube that entered the hot zone of the furnace. Gas flowing in the side of the chamber would contact the heat shield. In order to attain the fastest cooling rates a valve on the side of the chamber would be opened first to begin cooling the outer chamber, but allowing the furnace to continue to maintain a constant temperature in the hot zone and sample. After about a minute of cooling the outer chamber, the top valve would be opened, directly cooling the sample and the inner chamber.

To improve interaction of the quench gas with the sample, (sample cooling coil, SCC), a coil fabricated from welded stainless steel (316) tubing (0.18" ID X 0.25" OD) was attached to a sample stand and placed in the hot zone of the furnace, with a sample placed in the center of the coil. Slots were cut into the inner diameter of the SCC as an outlet for and to direct the cooling gas radially around the sample. The inlet to the SCC was attached to the top inlet valve of the furnace.

A typical quenching procedure would begin with pressuring the quench system[†] with the quench gas followed by submerging the QGC into the dewar of liquid nitrogen. After the QGC was sufficiently cool, as indicated by reduced boiling of the LN_2, the main vacuum valve was closed and the side gas inlet valve opened, allowing the cooling gas to flow into the exterior

[†] The entire quench system and vacuum chamber should be purged with inert gas before beginning the pump down of the system.

vacuum chamber. Once the chamber was pressurized, the chamber bleed valve is opened, allowing the hot gas to vent (gas was ventilated outside of the building). After cooling the exterior chamber with the furnace controller still in the programmed hold at 913°C, the top inlet tube is opened allowing the sample and inner chamber to be cooled via the SCC. This corresponds to the furnace controller beginning the ramp down phase of the program. Adjustments can be made to the cooling gas flow rate or the chamber bleed valve to increase or decrease the cooling rate as appropriate.

Thermal Model

Model Overview

The thermal model calculates the two-dimensional transient temperature distribution as a result of multiple layer depositions of the titanium alloy Ti-6Al-4V during a single line build assuming temperature dependent thermophysical properties.

A numerical solution to the two-dimensional transient heat conduction equation is obtained using implicit (backwards-difference) finite-difference techniques. The results presented herein are computed using the implicit finite difference scheme. Explicit (forwards-difference) and Crank-Nicolson schemes were also constructed; however, the implicit scheme maintained a comfortable median between required computational power and accuracy. For a detailed summary of the implicit finite difference technique as well as how temperature dependent properties are calculated, please see the introduction.

Model Assumptions

One half of the part geometry is modeled on the $+y$ - z plane as illustrated in Figure 36. The simplifying assumptions made in the model include neglecting latent heat of melting/fusion effects, heat flow in the y-z plane is transient, heat flow in the x direction is steady-state and ignored, a constant temperature is maintained at the base of the substrate, convective cooling occurs on the outer surface of the build, symmetry boundary conditions imply the heat flux across the centerline (y = 0) is zero, and temperature dependent thermophysical properties for Ti-6Al-4V (shown in Table IX). It should be noted that only thermal conductivity, k, and specific heat, C_p, and not density, ρ, were considered to be a function of temperature.

Table VIII: Model geometry and constant process variables

½ Layer Width, w	7.0 *mm*
Layer Height, h	5.0 *mm*
Substrate Height	7.0 *mm*
Time Step, Δt	0.25 *s*
T_{laser}	2162.25 *K*
T_{base}	298 *K*
t_{pass}	200 *s*
Number of Layers Deposited	8
Time Steps for an 8 Layer Model	16,000
Nodes for an 8 Layer Model	384

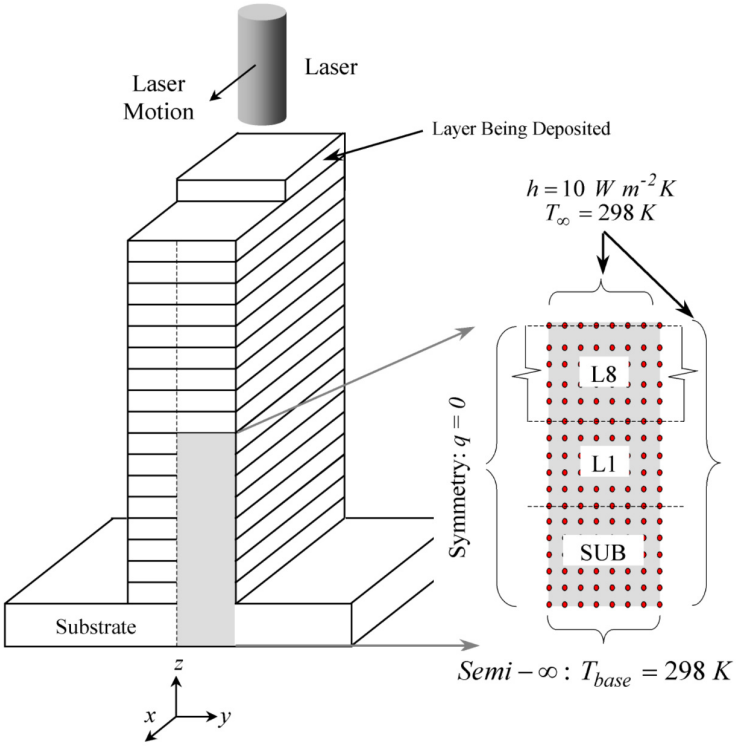

Figure 36: Schematic of modeled geometry (left), mesh and applied boundary conditions (right). The shaded region corresponds to the 2-½ dimensional geometry for an 8-layer model. The nodal mesh has nodes spaced equally at 1.0 mm. The substrate (SUB) is 7 mm thick (z) and each layer (L1, through L8) are 5 mm in height (z).

Modeling the deposition process was simplified by first assuming that as the laser moves away from the origin in the x direction, heat is no longer input into the two dimensional plane being modeled. Heat is input into the build at a fixed x position by assuming that when the laser is overhead, heating occurs, and when the laser moves away, cooling occurs as illustrated in Figure 37. Initially at $t = 0$, only the substrate (SUB) is present, having a uniform temperature T_{base}. At time $t = t_1$, a new layer is "birthed" or deposited having a constant temperature, T_{laser}, that is typically greater than the melting temperature. The new layer is held at T_{laser} for a "dwell time" (e.g., $0 < t \leq t_{dwell}$ for layer 1 (L1)), that is calculated from the laser speed, v_{laser}, and a

Table IX: Temperature Dependent Thermophysical Properties for Ti-6Al-4V [a, b]

Temperature [K]	311	366	422	477	533	589	644	700	755	811	866	922
k [W / (m K)$^{-1}$]	7.3	7.4	8.0	8.5	9.2	9.9	10.6	11.2	11.9	12.6	13.1	13.8
C_p [J / (kg K)$^{-1}$]	502.1	543.9	577.4	594.1	627.6	648.5	669.4	707.1	723.8	753.1	774.0	815.9

[a] R.A. Wood and R.J. Favor, Titanium Alloys Handbook, Metals and Ceramics Information Center, December 1972 (Figure 5-4:1).
[b] R. Boyer, G. Welsch, and E.W. Collings, eds. Materials Properties Handbook: Titanium Alloys, (ASM International, Materials Park, IH, 1994). pp. 513-6.

finite thickness, Δx, according to Equation [68]. The laser speed can be specified or calculated from Equation [69] .

$$t_{dwell} = \frac{\Delta x}{v_{laser}} \qquad [\ 68\ ]$$

The dwell time simulates the period of time that the laser is passing over a finite thickness, Δx. For $t > t_{dwell}$, there is no heat input into the build and the part is allowed to cool primarily by heat flow through the substrate (dictated by the constant temperature of the substrate at $z = 0$) and secondarily through convective cooling on the outside of the build. The part is allowed to cool for an interpass time, t_{pass}, which is calculated from v_{laser} and the build length, l, according to Equation [69]. When $t = t_{pass} + \Delta t$, a second layer is deposited on top of the first, and the process repeated. Solutions to the transient heat conduction equation are obtained at every time increment, Δt and stored to a file.

$$v_{laser} = \frac{l}{t_{pass}} \qquad [\ 69\ ]$$

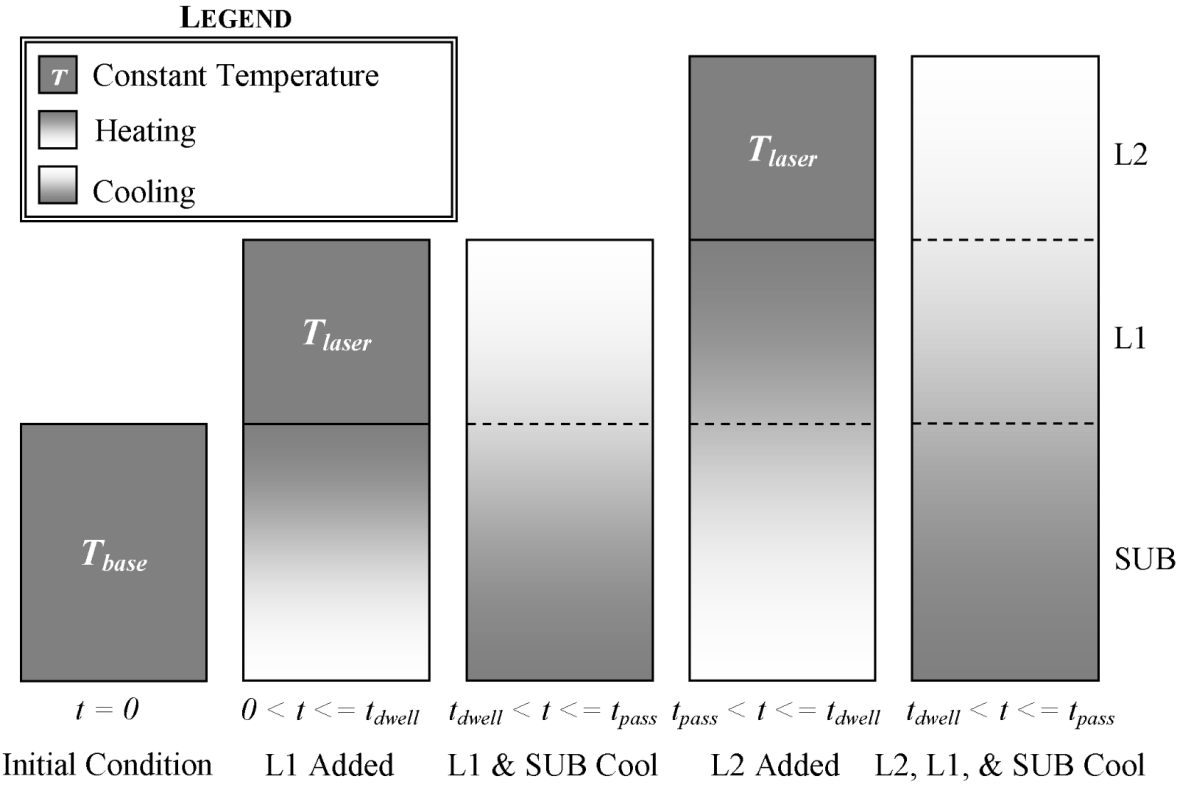

Figure 37: Schematic illustrating the method used to simulate additive layer deposition for a two-layer line build.

Process Parameter Sets

The laser velocity v_{laser} and cross sectional area ($y \times z$) of a layer gives an estimated mass deposition rate in units of mass per unit time according to Equation [70]:

$$\dot{M} = \rho \cdot w \cdot h \cdot v_{laser} \qquad [\ 70\ ]$$

where, ρ, w, and h are material density, layer width and layer height, respectively. Model constants used in the current research are shown in Table VIII. Table X shows three estimated process parameter sets (PS) used to calculate the forthcoming results. For the initial study of the model, the interpass time, laser superheat temperature, and base temperature are held constant while allowing the laser velocity, dwell time, and mass deposition rate to vary. Parameter Set A (PS-A) represents a slow laser speed, long dwell time, and slow build rate, while PS-C represents a fast laser speed, short dwell time, and high build rate. PS-B is in between PS-A and PS-C in terms of laser speed and build rate.

Table X: Model Processing Parameters Sets

Parameter Set (PS)	***Part Length*** $[m]$	v_{laser} $[m\ s^{-1}]$	t_{dwell} $[s]$	$\dot{M}$ $[kg\ hr^{-1}]$
PS-A	0.02	0.0001	10	0.178
PS-B	0.2	0.001	1	1.78
PS-C	0.8	0.004	0.25	7.13

Computer Program

The thermal model was programmed using the software package, *Mathematica*, by Wolfram.[99] A flow chart of the model can be seen in Appendix A: Thermal Model Flow Chart. The program was written as follows. First process parameters and material properties are input. From process parameters that describe the mesh, the position of each node is generated and placed in the appropriate table based on its position. That is, nodes that receive convective cooling on the side of the part are placed in a different list than those located on the top of the part because the coefficients and positions of surrounding nodes are different. There are lists for interior, symmetry, surface, and for the substrate. Once the nodes are generated, the program begins calculating the temperature of each node in the build for every time increment, or time step. The previously generated node lists are used to tell the program where coefficients to the

finite difference equations should be placed in the matrices used to calculate the temperature. Calculations are performed inside nested Do loops, the outermost being for each layer, and the innermost iterating for each time step. After the temperature is calculated for each layer, the data is saved to a file in order to conserve physical memory. Memory amounts in the range of 500 to 1000 MB were necessary to calculate the temperature profile for a build containing 384 nodes and 16,000 time steps. The data is saved in *Mathematica* notebook format and is arranged with rows containing calculated temperatures for each time step and the columns corresponding to nodes. A separate data file is generated containing process parameters used. The data is opened in a separate *Mathematica* notebook to generate plots of temperature versus time or position.

Chapter 4:

Results and Discussion

Results: As-Deposited Characterization

Ti-6Al-4V parts fabricated by direct metal deposition processes such as AeroMet's Laser Forming process exhibit distinct macro and microstructural features in the as-deposited[†] state. The macrostructural features include, large prior beta grains, a heat-affected zone in the substrate, and a macroscopic banding. Certain microstructural changes account for the observed features in the macrostructure. This section will characterize the macrostructural and microstructural features observed in as-deposited Ti-6Al-4V through dimensional and limited compositional measurement. It should also be noted that only results for the observations falling in the *y*-*z* plane of the build will be presented. The microstructure in the other orientations exhibited similar features and characteristics. In addition, there was little change in the as-deposited macro and microstructure in the *x* direction, i.e. a "steady state" was attained, after a distance of approximately 50 mm from the start of the build.

Macrostructural Features

Figure 38 is a macrograph of the deposit profile in the *y*-*z* plane showing the presence of large columnar prior beta grains (PβG), a well defined heat-affected zone in the substrate, and the presence of a macroscopic banding or "layer bands" that appears at the cusp of every layer except for the last three to be deposited. This section serves to measure certain macrostructural features that appear in as-deposited Ti-6Al-4V. Specifically, PβG width, heat affected zone depth, depth of re-melting, layer band thickness, and inter-band distance measurements will be

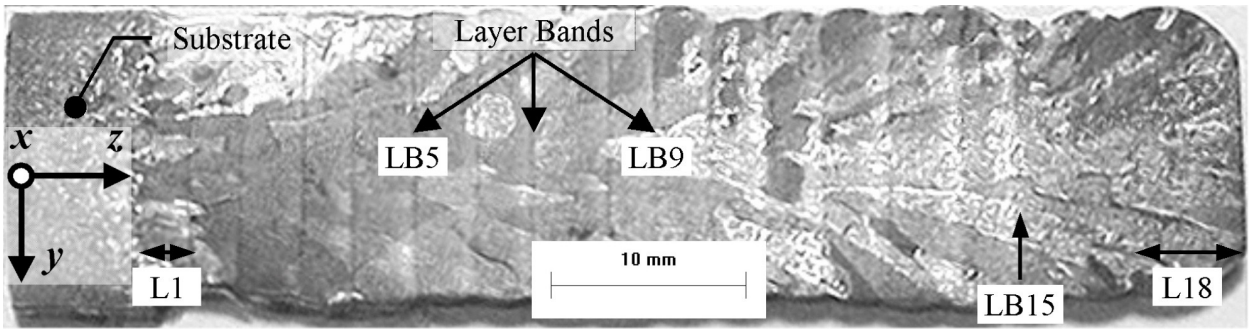

Figure 38: Polished and etched cross-section of an 18 layer LaserFormed Ti-6Al-4V rib-on-web build showing macroscopically visible features (HAZ, layer bands, and columnar prior beta grains). Layers (Lx) and Layer Bands (LBx) are labeled, with LB15 being the last visible layer band. The process coordinate system is also shown with laser motion in the *x* and build height in the *z* directions. (Profile10a)

[†] As-Deposited will refer to material deposited via AeroMet's Laser Forming process

presented.

Prior Beta Grains

Deposit

Figure 39 is a representative micrograph of the deposit PβG size. In the deposit, the PβG's are columnar in nature, oriented nearly perpendicular to the substrate (y-z plane) and cross multiple deposited layers and layer bands. The average PβG width of 222 measurements taken from 4 different *y* - *z* cross-sections (different *x* positions along the build) was 1.39 ± 0.80 mm. Qualitatively, the aspect ratio (width to height) was closer to unity (equiaxed) near the edges of the build, with the grains in the center of the deposit being more columnar (aspect ratio greater than unity).

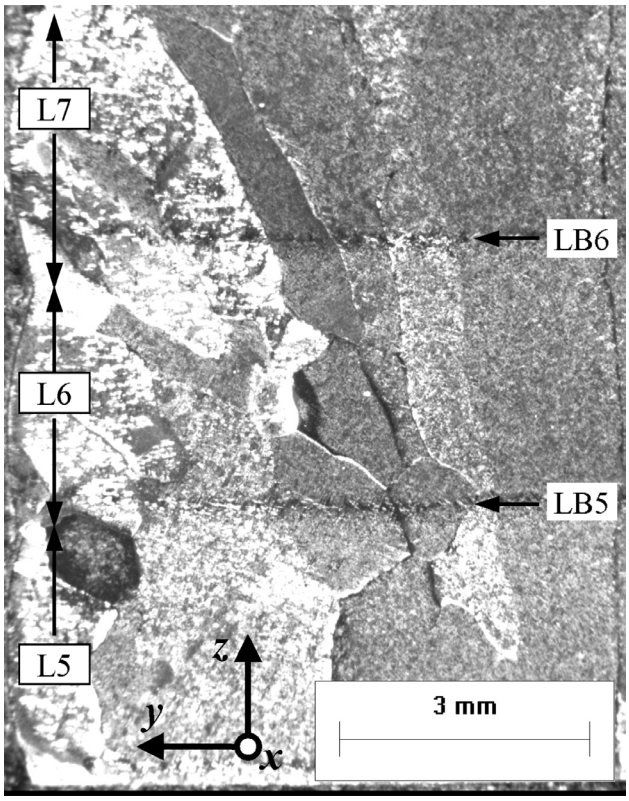

Figure 39: Macrograph of polished and etched surface of an as-received deposit showing prior beta grains (PβG) that have grown through several layers. Two layer bands are also visible (~12x). (AR-K-M-MAC(1.5)-001.tif)

Figure 41 shows the macrostructure from two different cross section planes, *x*-*z* and *y*-*z*. The section of the *x*-*z* plane shows that the columnar PβG's are tilted in the direction of laser motion (*x*).

Substrate

Figure 40 is a representative macrograph of the heat-affected zone (HAZ) appearing in the Ti-6Al-4V substrate (SUB) showing the presence of equiaxed PβG's that increase in size from the bottom of the substrate to the beginning of the first layer to be deposited (L1). At the intersection of L1 and the substrate, the PβG morphology changes from equiaxed to columnar.

The change in PβG size as function of HAZ depth (*z*-direction) in the substrate is shown in Figure 42. There is a three order of magnitude increase in the PβG size moving from the substrate into the deposit. The region in the substrate where no apparent grain growth has occurred is termed the unaffected zone (UAZ). The transition from the UAZ to the HAZ occurs approximately 1.5 mm from the bottom of the substrate and is demarcated by appreciable PβG growth. The HAZ depth was measured for three as-deposited samples and found to be approximately 5.4 ± 1.7mm. The gradual increase in PβG size continues until the grain morphology changes from equiaxed to columnar.

Concomitant with the change in grain morphology is the transition of the HAZ to a Fusion Zone (FZ). The FZ is a region of the substrate or previously deposited layer that was remelted as a result of the deposition of a new layer. The FZ in the substrate is nominally 1.0 mm.

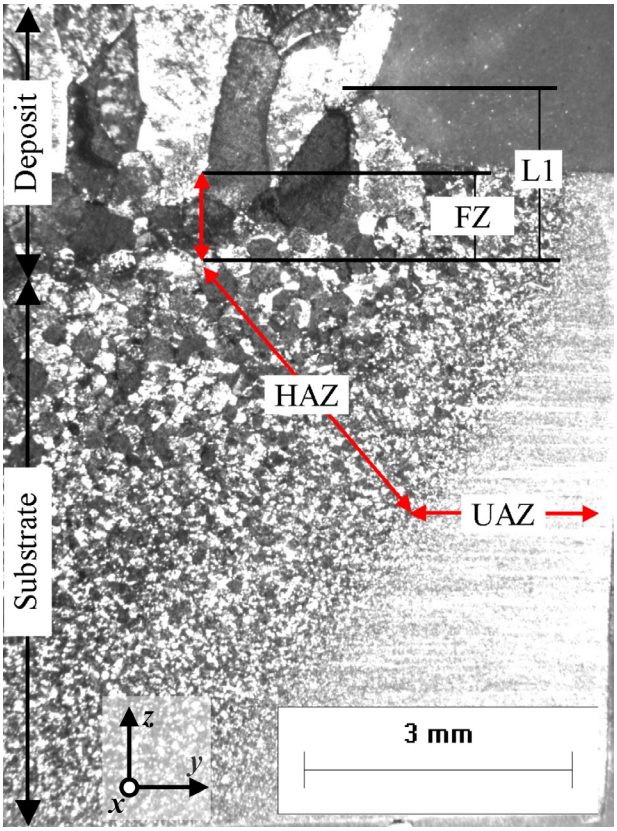

Figure 40: Etched and polished cross-section of the y-z plane in the substrate showing distinct changes in the prior beta grain size and morphology. The unaffected zone (UAZ), heat-affected zone (HAZ) and fusion zone (FZ) boundaries are shown (~12x). [AR-H-B-MAC(1.5)-001.tif]

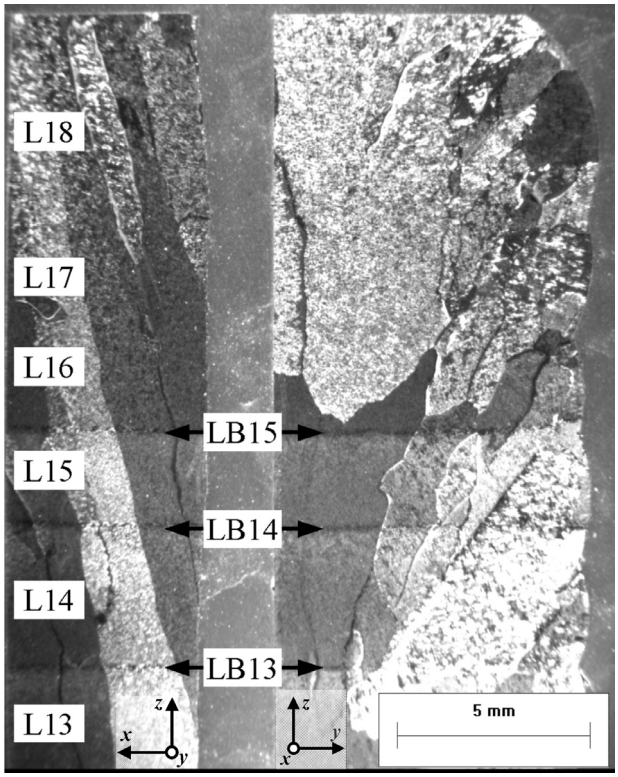

Figure 41: *x-z* (left) and *y-z* (right) cross sections taken from the top of the deposit showing the absence of layer bands for layers 16 through 18. Laser motion is in the *x* direction, as indicated by the slanted PβG's in the *x-z* sample. [AR-E-T-MAC(0.7)-001.tif]

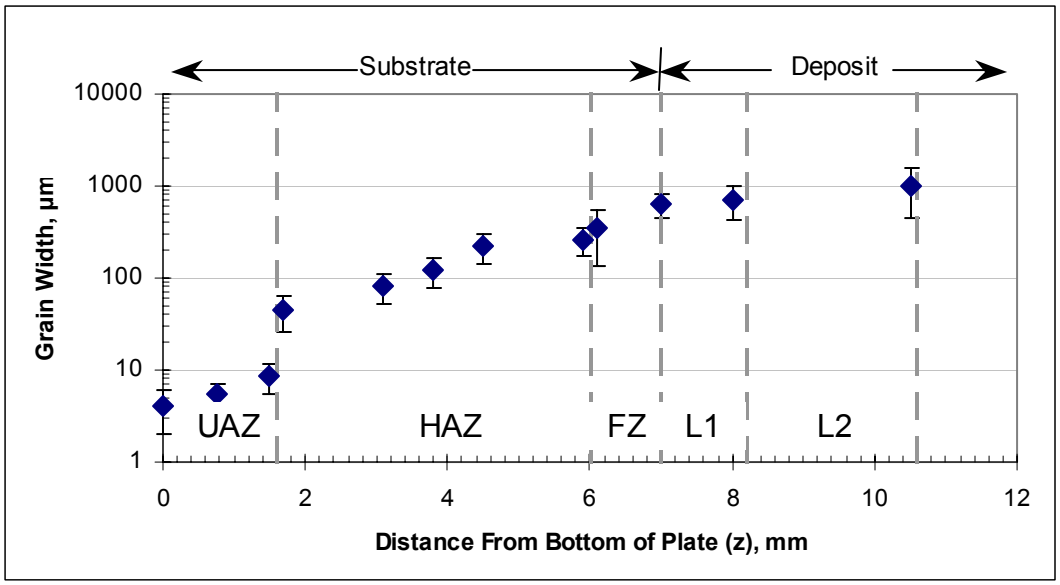

Figure 42: Increase in prior beta grain size moving in the *z* direction from the substrate into the deposit.

Layer Band

Inter-band Spacing

The macroscopic banding is observed in every deposited layer except for the last three layers to be deposited as illustrated in Figure 41. That is, the build consists of 18 deposited layers with only 15 layer bands observed. The spacing between each band was measured and found to be relatively constant through the length (*x*) and height (*z*) of the build, giving an average inter-band spacing of 2.9 ± 0.5 mm for 141 observations.

Microstructure

There are two distinct regions that exhibit microstructural differences in Laser Formed Ti-6Al-4V. First the "nominal" (Figure 43) or deposit microstructure between layer bands will be discussed followed by a description of layer band microstructure (Figure 44) and the features that distinguishes it from the nominal microstructure.

Deposit

Morphology

The nominal microstructure exhibits a basketweave Widmanstätten α morphology as shown in Figure 43. The normal morphology is present between layer bands and in the deposit of layers L16, L17, and the bottom of L18. The acicular HCP α phase is outlined in a thin layer

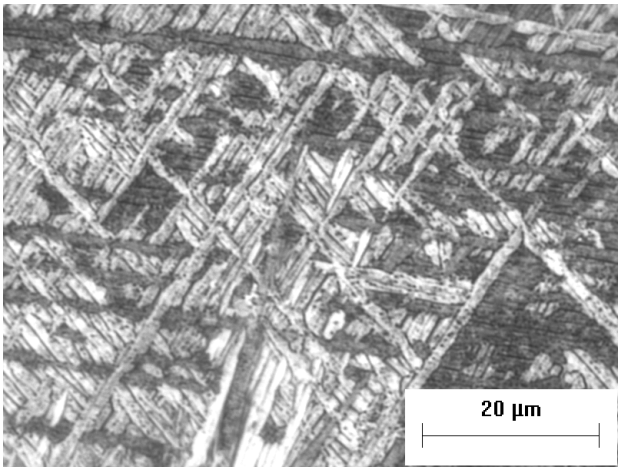

Figure 43: Nominal microstructure observed in the as received deposit consisting of randomly oriented (basketweave) Widmanstätten acicular α grains outlined in retained β phase. (~1000x) [AR-E-B-(N)[100x].tif]

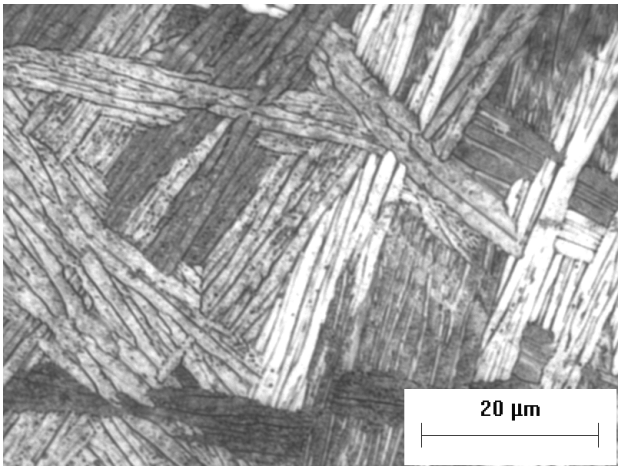

Figure 44: Microstructure of the layer band consisting of colony Widmanstätten acicular α grains outlined in retained β phase. (~1000x) [AR-E-B-(LB)[100x].tif]

of retained BCC β (dark) at the α grain boundaries. The prior beta grains are outlined in continuous α (Figure 49).

For the last layer to be deposited, L18, a transition from a basketweave Widmanstätten α morphology to a colony Widmanstätten α morphology with very fine acicular α grains less than 1µm in width occurs. It appears in Figure 45 that there is less β phase present in this region.

Grain Size

The width of the acicular α grains varies considerably between layer bands. Just above the layer band, fine basketweave Widmanstätten is observed; however increasing in the *z* direction towards the next layer band, the α grain width nearly doubles. This trend is exhibited in the micrographs of Figure 46, Figure 47, and Figure 48 for position in the *z*-direction just above, between, and just below a layer band in the same layer. The change in α grain width with the z-direction is quantitatively shown in Figure 50. The trend of increasing α grain width between layer bands is present for every layer band. After LB 15 in the 16th deposited layer (L16), the gradient continues in a similar fashion as in previously deposited layers until the cusp of L16 and L17 is reached, hereafter the α grain width begins to decrease.

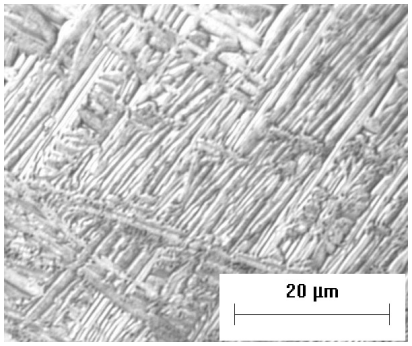

Figure 46: Micrograph taken just above a layer band (LB9) showing fine basketweave Widmanstätten α. The average grain width for this image was 1.0±0.4µm for 10 measurements. (~1000x). [AR-K-M-013.jpg]

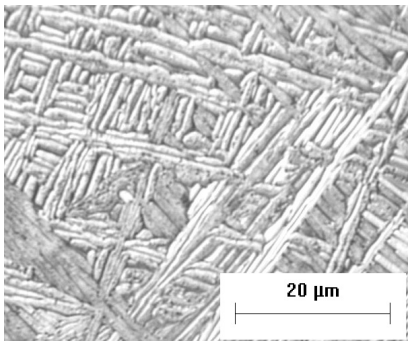

Figure 47: Micrograph taken midway between two layer bands (LB9 and LB10) showing slightly coarser basketweave Widmanstätten α. The average grain width for this image was 1.2±0.2µm for 10 measurements. (~1000x). [AR-K-M-014.jpg]

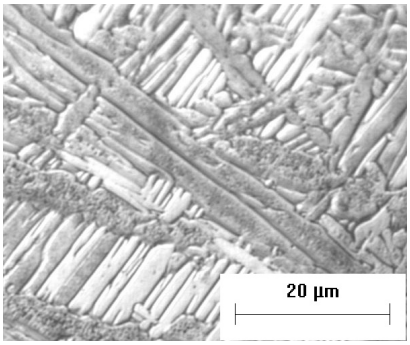

Figure 48: Micrograph taken just below a layer band (LB10) showing coarse basketweave Widmanstätten α. The average grain width for this image was 1.9±0.9µm for 10 measurements. (~1000x). [AR-K-M-015.jpg]

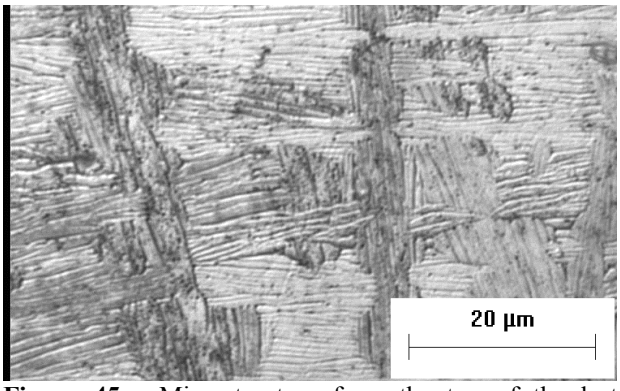

Figure 45: Microstructure from the top of the last deposited layer (L18) exhibited a colony Widmanstätten morphology with very fine grain width. There appears to be less beta in this microstructure.

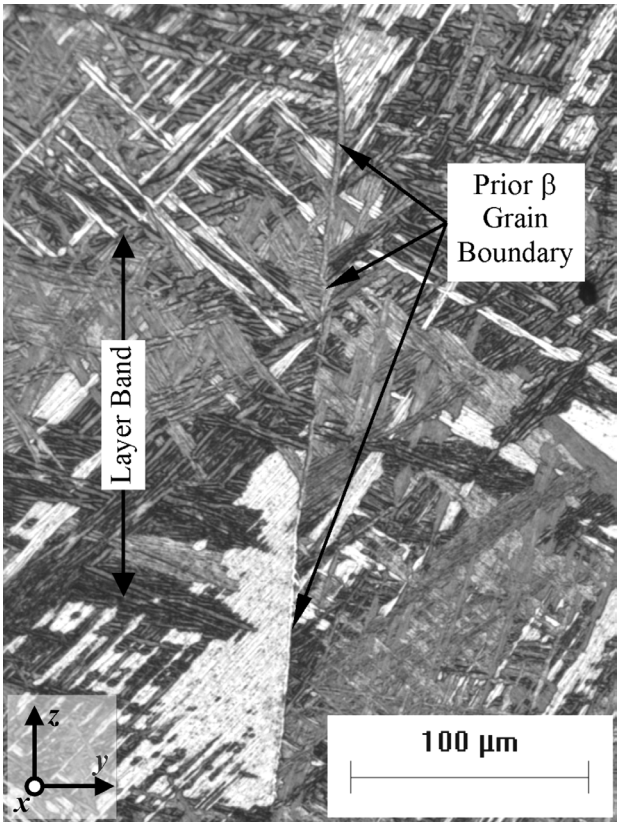

Figure 49: Micrograph showing a prior beta grain boundary outlined in continuous α that runs through a layer band. (~200x) [AR-E-B-(LB-PbG)[20x].tif]

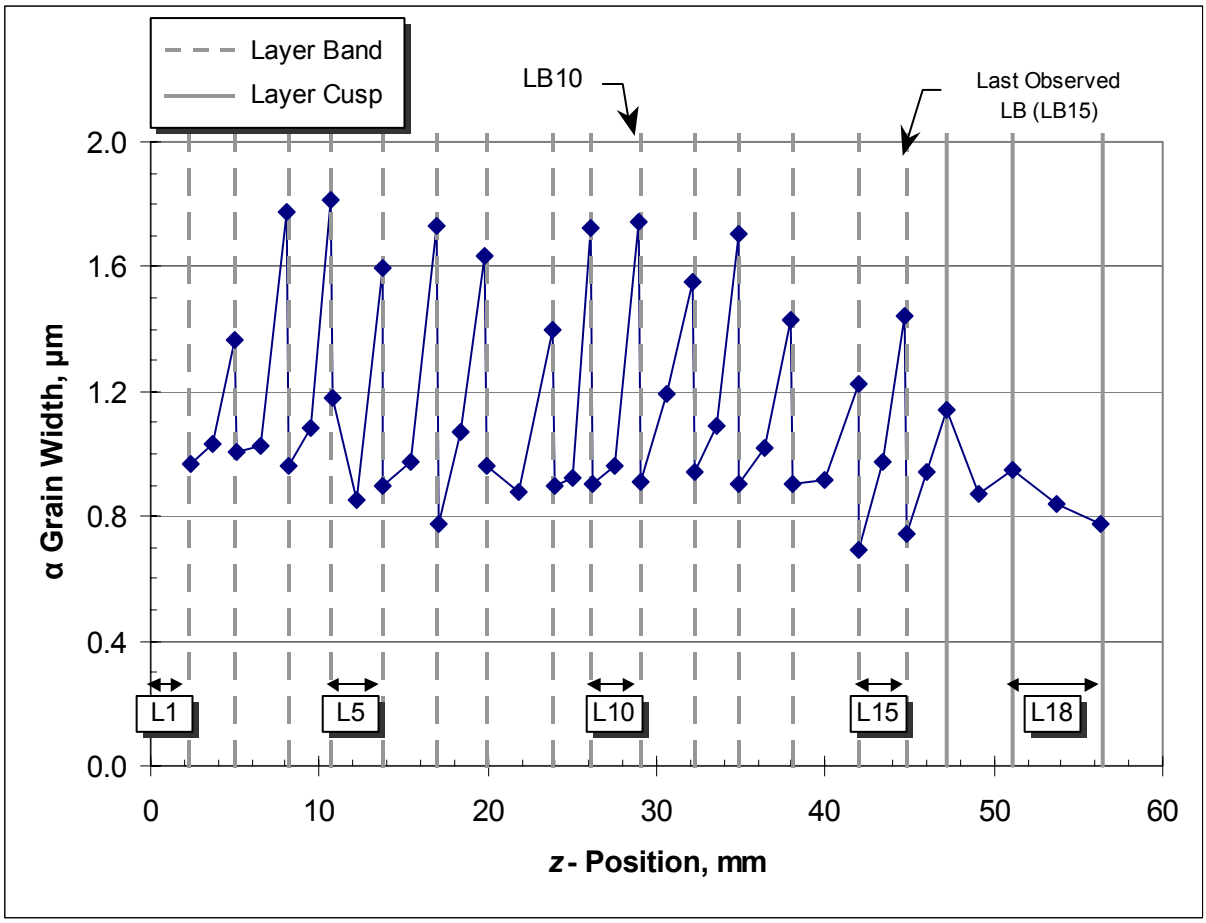

Figure 50: Alpha grain width versus *z* position in the build. Dashed gray vertical lines represent layer bands (LB) and solid vertical gray lines (L) represent layer cusps, where no layer bands are observed.

Layer Band

Morphology

The layer band microstructure consists of coarse colonies of acicular Widmanstätten α grains. A colony is defined as a packet of α grains having the same orientation relationship with the parent β grain. The layer band is macro and microscopically different than what is observed between the layer bands. In addition, layer bands traverse the entire width of the deposit, with the only discontinuity being prior beta grains outlined in continuous α that run vertically through the LB as seen in Figure 49.

Layer Band Width

The thickness of the region of the deposit exhibiting the colony α microstructure increases slightly with build height as shown in Figure 51, with an average value of 166 ± 29 µm.

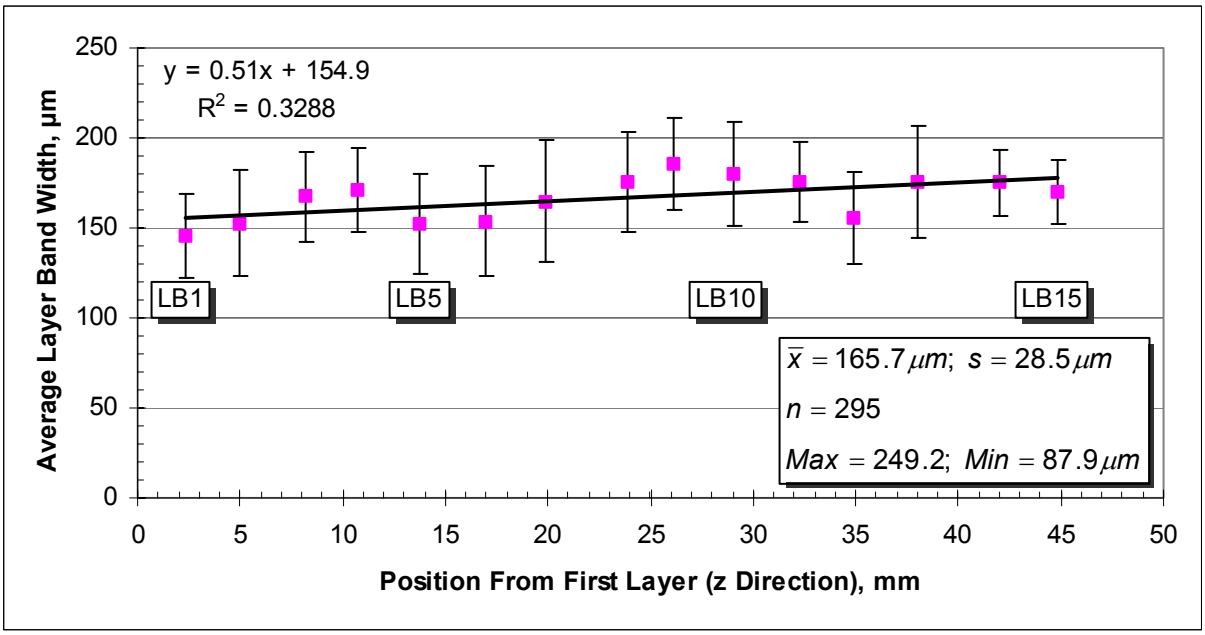

Figure 51: Width of the layer band as a function of build height.

Colony Size

The size of the α colonies within the layer band remains constant throughout the height of the build, with an average colony size of 13.2 ± 7.2 µm.

Substrate

Morphology

The substrate exhibits a variety of microstructural morphologies dependent upon the position from the bottom of the plate. Figure 52 is a micrograph from the UAZ showing a bimodal structure of globular α grains elongated in the direction of rolling and equiaxed lamellar α+β. The substrate was mill annealed at 700°C for 2 hours after rolling and prior to deposition of Ti-6Al-4V.

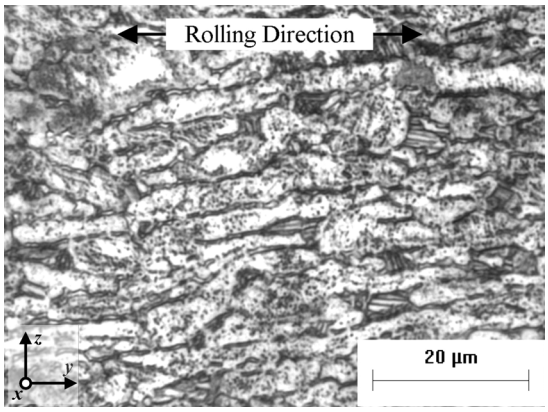

Figure 52: Micrograph of the unaffected zone in the substrate showing a bimodal microstructure consisting of elongated α grains and equiaxed colonies of lamellar α+β. . (~1000x) [AR-E-B(UAZ)[100x].tif]

The α grains become larger and more acicular as the HAZ and FZ are encountered as shown in Figure 53 and Figure 54 respectively. In the HAZ, the morphology of the Widmanstätten α grains is colonial, due to the small PβG size. In the FZ a basketweave morphology is observed.

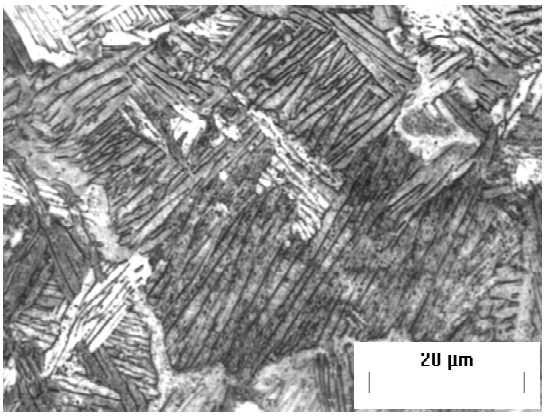

Figure 53: HAZ microstructure showing colony Widmanstätten α outlined in retained β. Alpha outlines the prior beta grains. This image contains one PβG. (~1000x) [AR-E-B(HAZ)[100x].tif]

Characterization of Features

Deposit vs. Layer Band

Hardness Profile

Vickers macro and micro hardness measurements were made along both the z and y directions of the build to determine if a difference microstructural features correlate to differences in mechanical properties. The

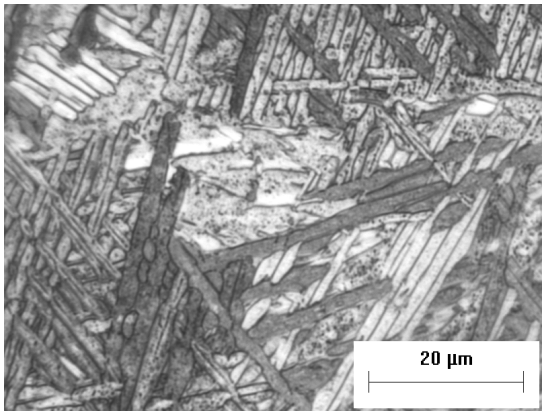

Figure 54: Fusion zone microstructure, showing basketweave Widmanstätten α structure with dispersed globular α. (~1000x) [AR-E-B(FZ)[100x].tif]

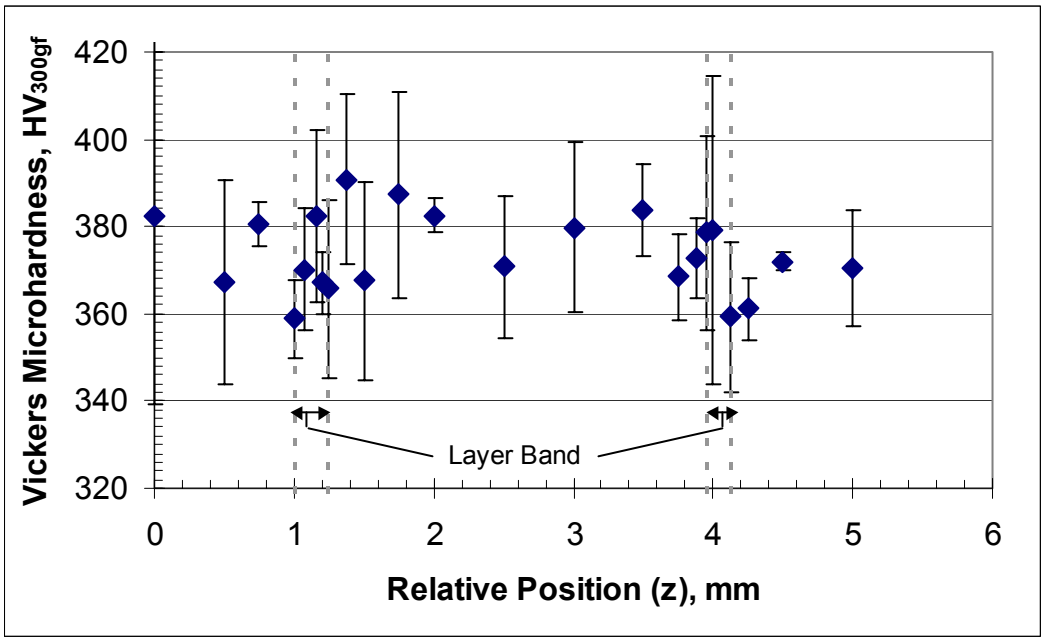

Figure 55: Vickers Microhardness profile between two layer bands showing little variation in hardness across three deposited layers

vertical (*z*) measurements were made from the bottom of the substrate to the top of the part and are shown in Figure 57. In addition to the vertical macrohardness profile in Figure 57, microhardness measurements were made profiling the hardness between two layer bands as shown in Figure 55. The only significant difference in the hardness profile is observed in the substrate where the hardness is slightly lower than in the deposit.

Horizontal (*y*) Vickers microhardness measurements were made on and between two layer bands with the resulting data shown in Figure 56. Again, there is no distinguishable difference in the hardness of the layer band compared with the nominal material.

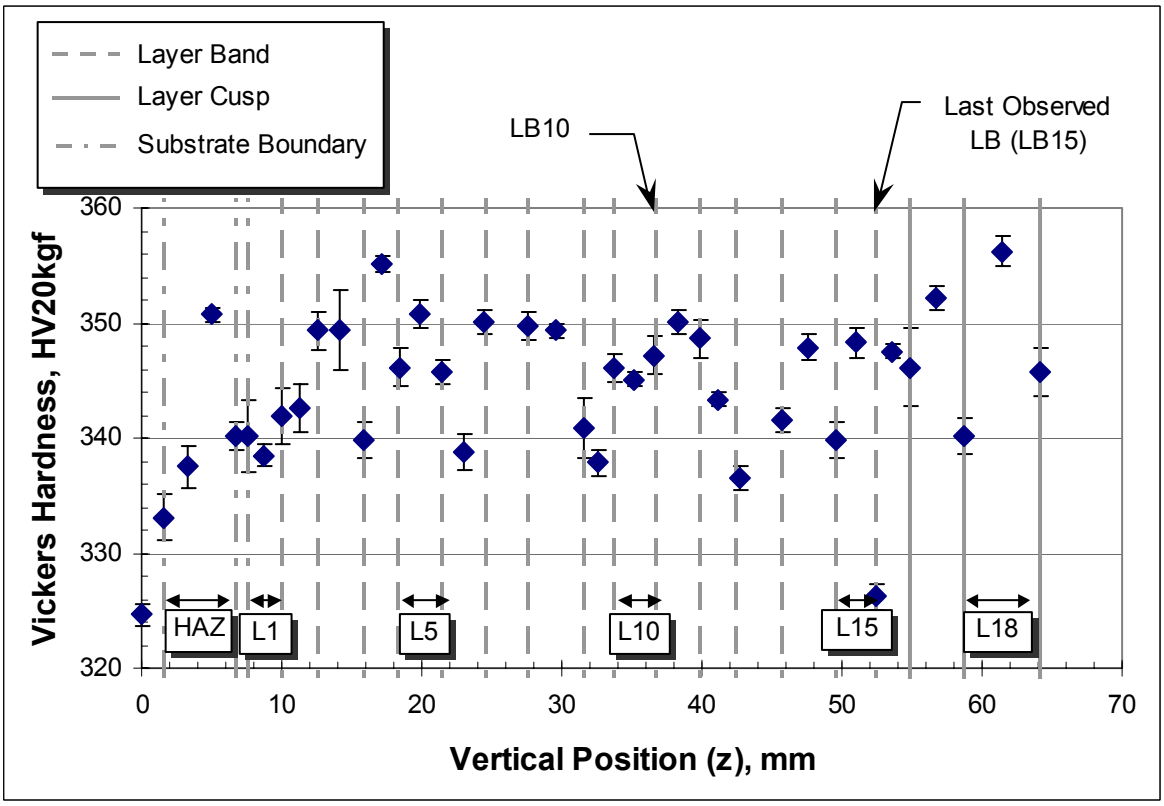

Figure 57: Vickers macrohardness vertical profile of the laser formed deposit

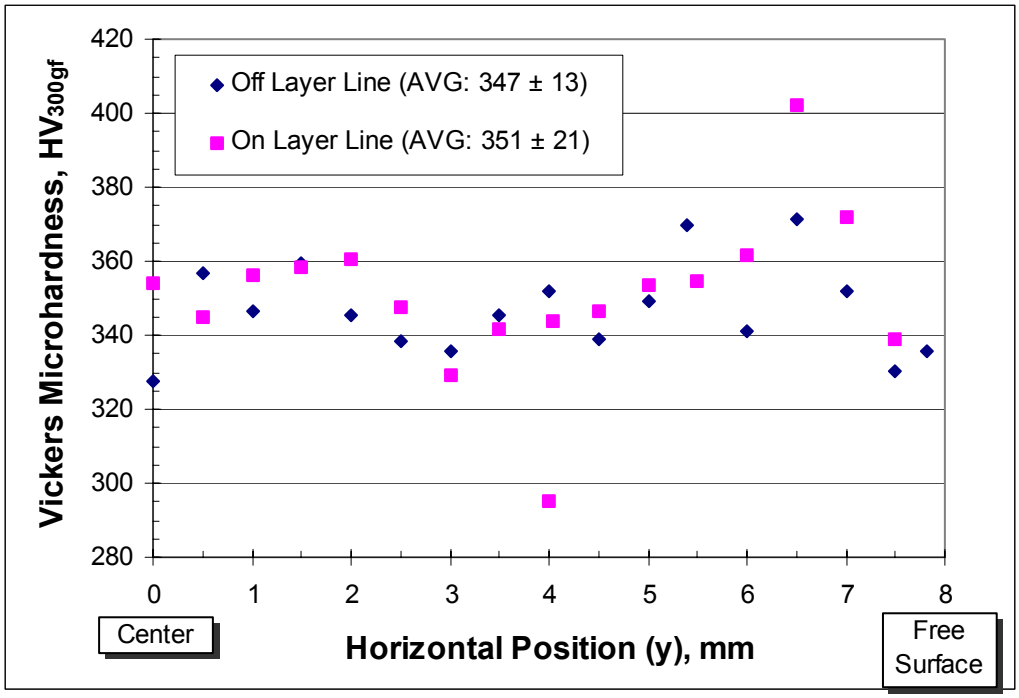

Figure 56: Horizontal Vickers Microhardness profile measured from a layer band and the adjacent material.

Composition Profile

Quantitative compositional analyses were made at various *z*-positions in the as-deposited material to determine if the microstructural differences in the layer band and normal material were due to segregation of alloying elements. Please refer to the Experiment-As-Deposited Procedures for a summary of the beam sizes and step distances. An 8.1 mm and three 1.6 mm traverses were made across layer band(s) as shown in Figure 58 using a beam spot size of 5 μm by 4 μm. The result of the 8.1 mm traverse across three layer bands is shown in Figure 59. Figure 60 shows composition data representative of the 1.58 mm traverse across a single layer band. Figure 61 shows the composition profile of a 9.9 mm traverse across the 16th, 17th, and 18th deposited layers where layer bands are not present. Table XI shows the average, standard deviation, and count for each traverse. Table XII shows the average normalized weight percent so that the total equals 100%.

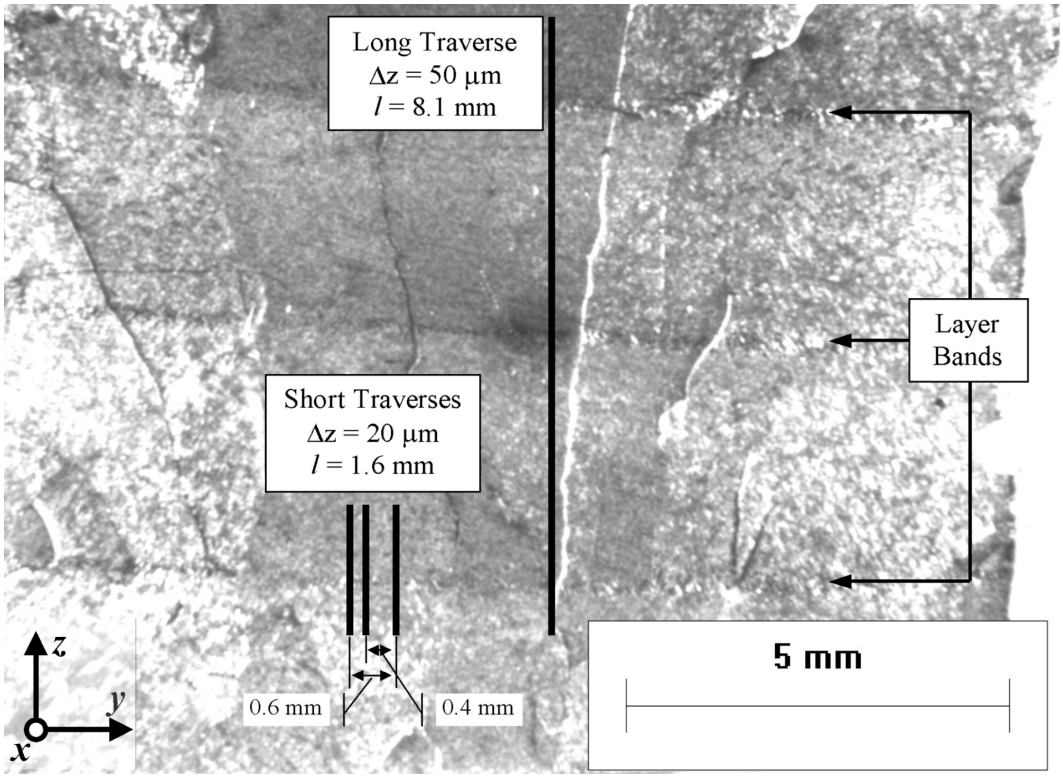

Figure 58: Macrograph showing the approximate positions of the compositional analyses on a sample containing layer bands.

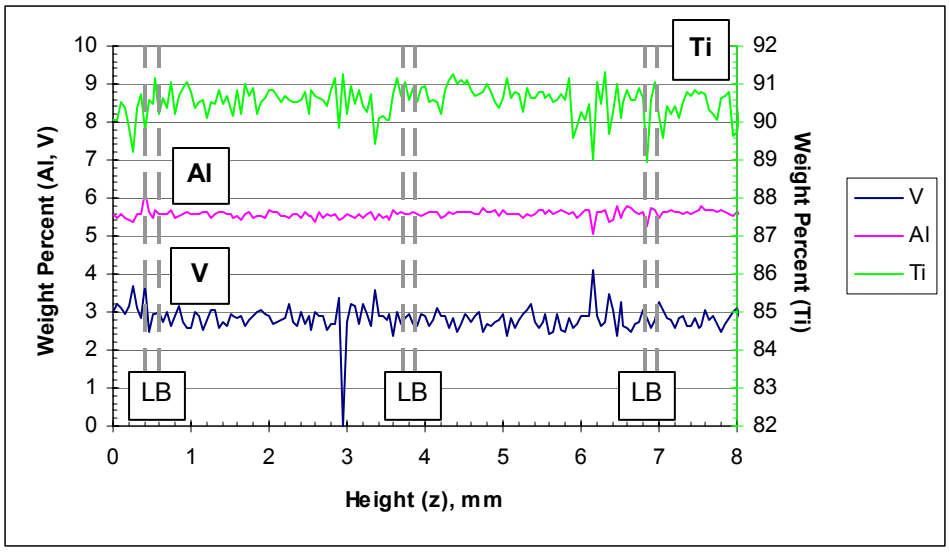

Figure 59: Composition profile for the 8.1 mm long traverse that crosses three layer bands. The position of the layer bands are approximate. The average composition in weight percent for this figure is 90.54 Ti, 5.58 Al, and 2.83 V.

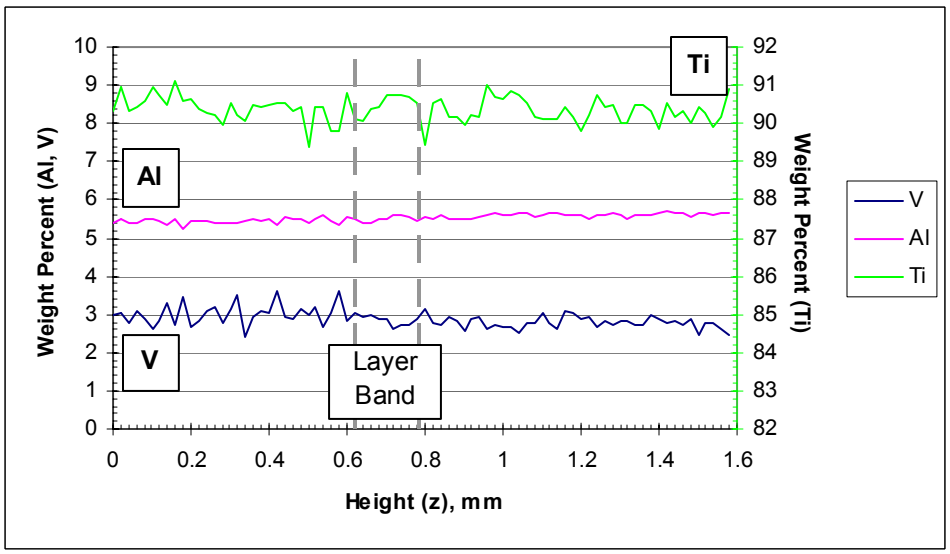

Figure 60: Composition profile of the central 1.6 mm long traverse that crosses one layer band. The position of the layer band is approximate. The average composition in weight percent for this figure is 90.37 Ti, 5.53 Al, and 2.88 V.

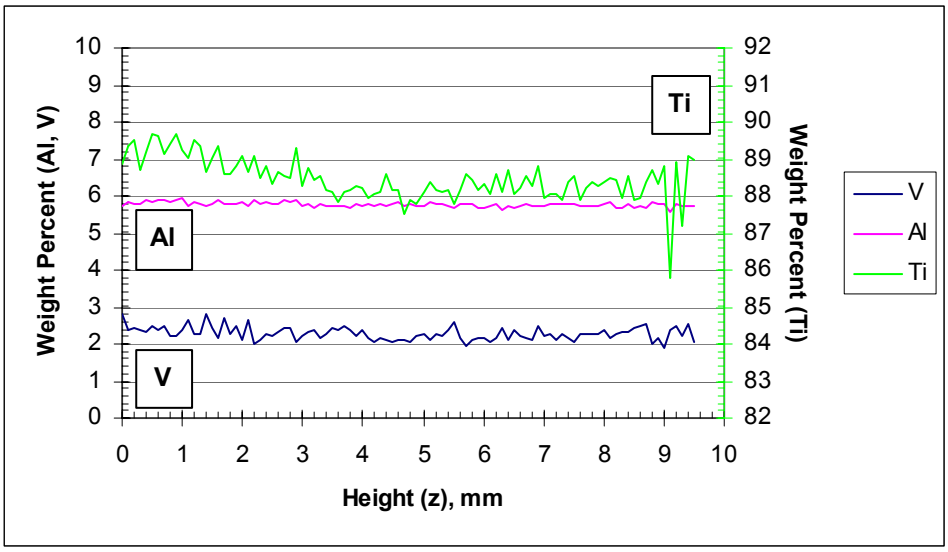

Figure 61: Composition profile of the central 9.9 mm long traverse that does not cross any layer band. The average composition in weight percent for this figure is 88.47 Ti, 5.77 Al, and 2.28 V.

The data shown above for the composition profiles made on a layer band show that there is no systematic variation in the amounts of titanium, aluminum, or vanadium. The composition profile from the top of the build (absent of layer bands) does not exhibit systematic variation in aluminum or vanadium, but the amount of titanium decreases about 1 percent in the last two layers to be deposited. The amount of aluminum is greater and the amount of vanadium is less in the top of the part as compared to the region containing layer bands. It should be noted that the raw totals (Table XI) for the scans made at the top of the part are about 1 percent lower than in the region containing layer bands. Lastly, the normalized average composition for all analyses (5.79 Al, 2.67 V, and 91.54 Ti) was less than the nominal composition of the alloy (6Al-4V, balance Ti) with a greater deviation from the nominal composition occurring in the region containing layer bands.

Table XI: Composition Measurements

	Position From Center Measurement	Weight Percent				Statistic
		Ti	*Al*	*V*	*Total*	
Long Traverse (LB)	-	90.54	5.58	2.83	98.95	*Average*
		0.42	0.10	0.34	0.42	*StDev*
		163	163	163	163	*Count*
Short Traverse (LB)	Right (y = 0.4 mm)	90.48	5.58	2.83	98.88	*Average*
		0.44	0.08	0.23	0.39	*StDev*
		80	80	80	80	*Count*
	Center (y = 0 mm)	90.37	5.53	2.88	98.77	*Average*
		0.34	0.10	0.24	0.34	*StDev*
		80	80	80	80	*Count*
	Left (y = -0.2 mm)	90.18	5.60	2.78	98.55	*Average*
		0.44	0.13	0.27	0.39	*StDev*
		80	80	80	80	*Count*
Long Traverse (No LB)	Right (y = 3.9 mm)	89.22	5.84	2.37	97.43	*Average*
		0.59	0.08	0.19	0.63	*StDev*
		100	100	100	100	*Count*
	Center (y = 0 mm)	88.47	5.77	2.28	96.52	*Average*
		0.58	0.06	0.18	0.65	*StDev*
		96	96	96	96	*Count*
	Left (y = -3.9 mm)	89.27	5.84	2.39	97.50	*Average*
		0.76	0.07	0.21	0.89	*StDev*
		100	100	100	100	*Count*

Table XII: Normalized Composition

	Position From Center Measurement	Normalization Factor	Average Normalized Weight Percents			
			Ti	*Al*	*V*	*Total*
Long Traverse (LB)	-	1.01	91.50	5.64	2.86	100.00
Short Traverse (LB)	Right (y = 0.4 mm)	1.01	91.50	5.64	2.86	100.00
	Center (y = 0 mm)	1.01	91.49	5.60	2.91	100.00
	Left (y = -0.2 mm)	1.01	91.50	5.68	2.82	100.00
Long Traverse (No LB)	Right (y = 3.9 mm)	1.03	91.57	5.99	2.44	100.00
	Center (y = 0 mm)	1.04	91.66	5.97	2.37	100.00
	Left (y = -3.9 mm)	1.03	91.56	5.99	2.45	100.00

Discussion: As-Deposited Micro and Macrostructure

Before the observed macro and microstructures are discussed, it will be helpful to understand, on a basic level, what is occurring during the direct metal deposition process. A molten layer of metal is deposited in a single line on a substrate of the same metal. Initially this new layer will be molten and some remelting of the substrate will occur (and is necessary to obtain a good metallurgical bond). A remelting depth of approximately 1 mm was observed in the as-deposited material. The substrate will be instantaneously heated due to the presence of the molten material. Initially the temperature in the substrate will vary from the initial temperature of the substrate to the temperature of the molten material. Different regions of the substrate will be heated into the $\alpha+\beta$, β, β+Liquid, and Liquid phase fields. A gradient in the peak temperatures observed during the deposition of the first layer will be present, with higher peak temperatures experienced closer to the new layer. In addition the time a point experiences the peak temperature will be a gradient as well, with positions closer to the new layer experiencing the peak temperature sooner.

The heating and cooling that occurs in direct metal deposition process can be thought of as decaying thermal wave traveling in the $-z$ direction through the material. This is analogous to a wave coming ashore. Ahead of the wave heating occurs while behind the wave cooling occurs. The properties of the thermal wave, temperature and velocity, will be dependent upon processing parameters (energy input) and thermal properties of the material (thermal conductivity), respectively. The temperature of the wave will not be constant, as energy is transferred to the material as the wave moves.

As the laser moves away in the x-direction, the substrate and newly deposited layer will begin cooling. Recall that the microstructure at the instant cooling begins will also be a function of position since peak temperature is a function of position. The cooling rate depends on the starting temperature and will increase with z-position since peak temperature increases with z position. Upon cooling, phase transformations will take place that are dependent upon peak temperature and cooling rate. For example if a position A in the substrate is heated above the beta transus and cooled rapidly α' may form; however, for a position B just below A, the cooling rate and starting temperature may not be sufficient to transform to α' and $\alpha+\beta$ will be present. It

is evident that a variety of microstructures and morphologies may be present that develop at different times during the deposition process.

The above discussion is for the deposition of a single layer and there is no need to extend it to multiple layers at this time. In DMD processes, multiple layers of material are deposited, resulting in a wide array of temperature changes taking place under non-equilibrium conditions. This makes interpretation of as-deposited microstructures difficult, especially in alloys such as Ti-6Al-4V where a wide range of phase transformations and morphologies occur. It is also difficult to determine when a particular feature forms since there are so many layers that have been deposited. It helps to have experimental temperature data taken during the deposition, or a thermal model that generates the temperature data; however, data for non equilibrium transformations is necessary to draw accurate conclusions about what is occurring during the deposition process. A discussion of how thermal model data relates to the observed macro and microstructural features, in particular when the features form will follow in a subsequent section. First an understanding of what temperature and cooling conditions will result in the observed microstructures is necessary.

Substrate

The substrate exhibits three distinct zones caused by different levels of heating, the unaffected zone (UAZ), heat affected zone (HAZ) and fusion zone (FZ). In the UAZ little or no α or β grain growth is observed; therefore, it can be concluded that this region did not see temperatures that were sufficient for growth of the α or β phases.

On a macroscopic level the HAZ exhibits a change in the prior beta grain size from less than 10μm at the UAZ/HAZ interface to 200μm at the HAZ/FZ interface. The prior beta grains are equiaxed and contain colony Widmanstätten α. The increased amount of beta grain growth and change in microstructural morphology from elongated α grains to colony Widmanstätten α indicates that the HAZ was heated above the β transus.

The FZ marks a transition from an equiaxed prior beta grain morphology to one that is columnar indicating that melting has occurred. In processes utilizing a high energy heat source such as a laser or an electrode that causes localized melting in a metal, initial solidification occurs epitaxially from the base metal. This is due to similarities in the composition and surface

energies of the melt and base metals. The microstructure in the FZ exhibits a basketweave Widmanstätten α morphology, indicative if faster cooling rates from the β phase field.

Deposit Prior Beta Grains

It was observed that the deposit prior beta grains are columnar in nature, and oriented nearly perpendicular to the substrate in the *y*-*z* plane and slightly tilted in the direction of laser motion in the *x*-*z* plane. The prior beta grains also grow across multiple deposited layers. Initial solidification of the columnar grains occurs epitaxially from the grains in the base metal, or previously deposited layers, due to similarities in the composition and surface energies of the metal. This allows for the columnar grains to continue growing across multiple layers. The aligned orientation of the prior beta grains is typical for high-energy processes, such as welding and laser deposition of thick layers. Upon cooling from the melt, the growing grains align themselves with the steepest temperature gradients.[100] In direct metal deposition of a single line of material, heat flows nearly perpendicular to the substrate in both the *y* and *x* directions. There is a slight bias of the prior beta grains in the +*x* direction, or the direction of laser motion, due to the moving heat source. The grain boundaries of the prior beta grains are outlined in continuous α.

Nominal Microstructure

The nominal microstructure is observed between layer bands. The microstructural morphology is basketweave Widmanstätten α. Increasing cooling rate from the β phase field, increasing the amount of β stabilizer (V in the case of Ti-6Al-4V), and decreasing the β excursion temperature and time will favor formation of the basketweave α over a colony morphology.[31]

The width of the α grains is smallest just above a layer band (e.g., LB1) and largest just below the next layer band (e.g., LB2). The gradient in α grain width is present between every layer band in the deposit and just above the last layer band observed. An Analysis of Variance (ANOVA) and Student's t-test (See Appendix B: Statistics) were performed on the α grain width data for measurements made just above, in between, and just below a layer band. It was determined using a confidence level of 95% (α=0.05) and assuming unequal variances that the means were unequal. That is, there was statistical difference between the mean values of the α

grain size above, between, and just below a layer band; therefore, the argument that a gradient exists and not that there is scatter in the data is statistically sound.

Compositional gradients or thermal effects are two of the most likely reasons why a gradient in the microstructure would exist. Since there was no systematic variation in composition between layer bands, it can be concluded that the gradient in α grain size is due to thermal effects, specifically peak heating temperature and cooling rate from the peak temperature. Higher temperatures result in larger grains while faster cooling rates result in finer grains. These effects are actually competing since typically with a higher temperature, a faster cooling rate would be expected. If time is considered, the argument could be made that larger grains are a result of longer times at or above a certain temperature. At this point it is unclear whether time, temperature, or cooling rate are responsible for the gradient in α grain size for the DMD process. The evolution of the gradient in the α grain width will be discussed with the formation of the layer bands below.

Layer Bands

The layer bands exhibit a colony Widmanstätten α morphology that is different from the nominal microstructure which has a basketweave Widmanstätten α morphology. The colony or packet size, layer band thickness, and inter-band spacing remains constant throughout the build, indicating that whatever causes the layer bands is constant and periodic. It was stated above that the basketweave morphology will tend to form with increasing cooling rate from the β phase field, increasing the amount of β stabilizer (V in the case of Ti-6Al-4V), and decreasing the β excursion temperature and time.[31] Three theories have been proposed for the formation of the layer bands, including, oxidation, macro/microsegregation of alloying constituents, and thermal cycling effects.

In titanium alloys, the α phase is stabilized by oxygen interstitials and subsequently embrittles the alloy at high levels.[101] It was thought the surface of each freshly deposited layer would oxidize, resulting in a region that was α stabilized (absent of β) and having a higher hardness. As the next layer is deposited, the α-case of the previous layer would be "buried" in the microstructure. Oxidation effects were ruled out as a cause of the layer band for several reasons. First, the hardness both on and off of the layer band were very similar, whereas an α case is described as hard and brittle. A statistical analysis of the hardness data collected on and

off a layer band was performed using ANOVA and a Student t-test (See Appendix B: Statistics). It was determined using a confidence level of 99% (α=0.01) and assuming unequal variances that the means were equal. That is, there was no statistical difference between the mean values of hardness measured on and off a layer band. Secondly, the direct metal deposition of the alloy is done in an inert atmosphere or argon. Also, there wasn't any discoloration on the surface of the parts normally associated with high temperature oxidation.

The second hypothesis for the formation of the layer band is macrosegregation of solute in the solidifying material. Macrosegregation is defined as segregation that extends over several grain diameters. The type of macrosegregation that is described most often in literature on fusion welding is termed transverse solute banding.[102,103,104,105,106] The bands normally appear as curvilinear contours on the polished and etched surfaces of fusion weldments. These bands are attributed to thermal variations in the weld pool, which periodically change the solid-liquid interface velocity.[102,103,105] Electron microprobe studies have shown that in titanium alloys, transverse solute banding is a result of vanadium and aluminum segregation.[103] In the current work, quantitative electron microprobe composition analyses were performed on the DMD Ti-6Al-4V deposit. Significant scatter was observed in the titanium and vanadium composition profile due to the difficulty in distinguishing between these two elements. There was no systematic variation in the aluminum profile, where according to [31] we would expect to observe an increase in the aluminum concentration as a layer band was traversed. The electron microprobe scans were made with various step distances and analysis areas with the same result; there was no systematic difference in the aluminum composition as a layer band was traversed. Macrosegragation effects have therefore been ruled out as a cause of the layer band formation.

The third hypothesis for the presence of layer bands in the DMD material is due to the multiple thermal cycles that a fixed point sees during the build of the part. The analysis of Kobryn, et. al.,[92,93] agrees in that the macroscopic banding is a result of a new heat affected zone being formed. The dynamic nature of this process was described above and it is apparent that a fixed point in the build will experience several thermal excursions into different phase fields, will experience temperatures in the phase field for different times, and attain different cooling rates as multiple layers are deposited. The formation of layer bands is similar to what was proposed above for the presence of a gradient in the α grain width. There must be a specific combination of peak temperature, time at this temperature, and cooling rate that lead to the

formation of the colony (layer band) morphology over the basketweave (nominal) morphology; however, we cannot yet quantify the "what" since the temperature profiles are unknown.

Last Three Deposited Layers

It was observed that the microstructure of the last three layers to be deposited (L16-L18) was different than the rest of the deposit. First this region was absent of the layer band morphology. The second difference was that L16 exhibited the gradient α morphology as above without a layer band being present at the top of the layer. L17 and part of L18 exhibited basketweave morphology with very fine α grains. The top of L18, which would be the last metal to solidify exhibited a colony morphology containing very fine acicular α grains. The very fine α grains in the last two layers to be deposited can be explained by the high cooling rate associated with the deposition of a new layer of material and lack of subsequent thermal cycles to coarsen the α grains. The basketweave morphology observed in L17 and the bottom of L18 is also indicative of the high cooling rates from high in the β phase field. Note here that morphology is controlled by cooling rate, which is why the morphology is basketweave and not colony α.

The transition from a basketweave to colony morphology in L18 is most likely a result of segregation of aluminum to the top of a deposited layer, stabilizing the α phase and producing the colony morphology. L18 was not examined in its entirety using the electron microprobe; however, L16 and L17 were examined, with the result showing a slightly higher (+0.4wt%) amount of aluminum and decrease in titanium and vanadium as compared to traverses made from the middle of the build. Difficulties arise using the electron microprobe in distinguishing between titanium and vanadium since they are next to one another in the periodic table. If the electron microprobe data is correct, a decrease in vanadium or an increase in aluminum could result in the formation of the colony morphology. It was also noted in the microstructure that there was little β phase present, indicating a decrease in vanadium.

The colony morphology described for last layer deposited is not the same as what is observed in the layer bands. It will be shown that the layer band forms after the deposition of several more layers. The reason the colony morphology in the last layer deposited is not present in L17 or L16 is because when a new layer is deposited, partial remelting of a previous layer occurs, redistributing the solute and homogenizing the composition.

As-Deposited Microstructural Evolution

We can gain some insight as to when microstructural features such as the gradient in the α grain size and layer bands form (i.e., what layer deposition is responsible for their formation) through clues in the as-deposited microstructure. First, prior beta grains and grain boundaries have grown through the layer band, suggesting that the formation of the layer band in the first layer occurs only after subsequent layers are deposited. Second, layer bands are absent in the last three layers to be deposited suggesting that the layer bands are formed in the first layer to be deposited after the deposition of three subsequent layers. Lastly, the third to last layer deposited exhibits a gradient in the α grain size, where a layer band is not observed at the top of the layer. Thus, in order to pinpoint the cause of the layer band only the last four layers to be deposited need to be examined.

Beginning with the deposition of the layer containing the last observed layer band, L15, after cooling from the molten state, a fine basketweave Widmanstätten α morphology that transitions to a fine colony α morphology will be present as was observed in the last deposited layer (L18). The next layer (L16) is deposited on top of L15, causing remelting at the top of L15 and heating of the bottom of L15 high into the β phase field. This heating is followed by rapid cooling leading to a fine basketweave α morphology. L17 is deposited on top of L15 and L16, again causing heating of L15 into the β phase field, but for shorter period of time, resulting in a variation in the amount of α grain growth that occurs. More α grain growth will occur closer to the top of the part resulting in the gradient morphology as described above for the nominal microstructure. Upon deposition of L18, only a narrow region near the top of L15 will see an excursion into the β phase field of sufficient time and temperature to form the colony morphology, i.e. a layer band is formed. The material below the layer band (L15) may see an excursion into the β phase field upon deposition of L18, but it will not be of sufficient time or temperature to produce morphological changes. Thus the morphology induced in L15 by the deposition of L17, a gradient in the α grain width, will be below the fifteenth layer band (LB15).

In summary, it has been described that the gradient basketweave Widmanstätten α morphology forms in a layer, *n*, due to the deposition of layer *n+2*, while the layer band forms during the deposition layer *n+3*. It should be stated that this is not an empirical relationship and will be highly dependent on the processing parameters used. The beauty of the DMD process is

that the processing parameters could be changed to produce an all-layer band morphology, or an all basketweave morphology.

Results: Heat Treatment

The prescribed heat treatment was a 2-hour solution treatment at 913°C (1675°F) followed by a furnace-controlled cool down to 315°C at rates ranging from 0.3°C/min to 500°C/min. Each sample was subjected to a 4-hour aging treatment at 538°C (1000°F) followed by a furnace cool. All thermal treatments were performed in a vacuum of 10^{-4} torr.

Cooling Rate

Table XIII is a summary of the cooling rates attained during the solution treatment. The first column ("Heat Treat Label") is the label chosen to designate each heat-treated sample based on the programmed and actual cooling rates observed. "Programmed Cooling Rate" is the rate at which the furnace was programmed to cool. The third column is the Actual Cooling Rate over the prescribed temperature range (913 – 315 °C) determined from the slope of a linear fit of the time vs. temperature data recorded during the quench. The difference in cooling rate over the first and last 300 °C of the heat treatment is shown in columns 4 and 5. An example of the time vs. temperature data showing the cooling rate for the prescribed temperature range and the first and last 300°C of the temperature range is shown in Figure 62.

Table XIII: Programmed and Actual Cooling Rates for the Heat Treatment

Heat Treat Label	Programmed Cooling Rate	Actual Cooling Rate (913-315 °C)	Cooling Rate (913-600 °C)	Cooling Rate (599-315 °C)	Quench Atmosphere	Notes
	°C/min	°C/min	°C/min	°C/min		
0.3	0.3	0.3	0.3	0.3	Vacuum	
1	1	1	1	1	Vacuum	
10	10	9.9	9.9	9.9	Vacuum	
50	100	49	82	36	Ar @RT, 25 psi	
70/90	100	75	96	55	Ar @LN2, 25 psi	Heat treated twice, aged once
200	200	175	-	-	He @LN2, 90 psi	Data lost, estimated cooling rate
266	300	268	282	260	He @LN2, 100 psi	Cooling Rate to 350°C
400	400	358	618	256	He @LN2, 100 psi	
500	500	441	706	357	He @LN2, 115 psi	
555a	555	487	657	388	He @LN2, 110 psi	
555b	555	470	601	381	He @LN2, 115 psi	

For cooling rates of 10°C/min or less, the furnace controller does not need assistance in the form of a quench gas to attain the programmed rate; therefore, the actual cooling rate and programmed cooling rates are equal. For cooling rates faster than 10°C/min, a quench gas is needed. In order for the furnace to be able to cool at a constant rate above 10°C/min, several parameters such as flow rate of the quench gas, temperature of the quench gas, and when to begin cooling the chamber must be properly set. Because of the large number of variables involved, the limited number of samples, and the expense associated with using helium to obtain the fastest cooling rates (a full cylinder of helium was used for each of the heat treatments greater than 300°C/min), the process to attain exact cooling rates was not optimized, i.e., not all of the programmed and actual cooling rates are equal. Table XIII shows that under fast cooling rates, the furnace controller looses ability to maintain a constant cooling rate, and the cooling rate is dictated by quench gas variables (temperature, flow rate, pressure).

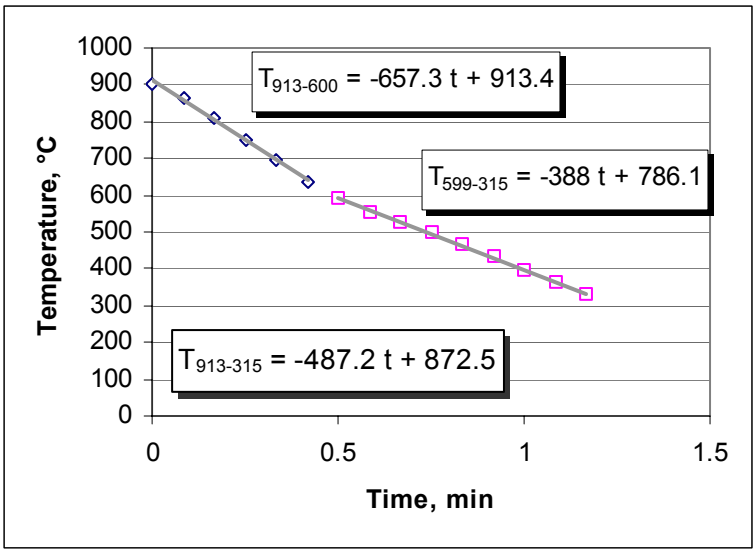

Figure 62: Temperature vs. time data for the solution treatment of the sample labeled 555a.

Microstructural Features

Representative micrographs of the heat-treated Laser Formed Ti-6Al-4V samples are shown in Figure 63, Figure 64, and Figure 65 for the slowest (0.3°C/min), median (200°C/min), and fastest (487°C/min) cooling rates, respectively. Figure 66 shows that the layer band structure was retained during the heat treatment, consistent with the suggestion that the banding occurs as a result of a super-transus thermal excursion.

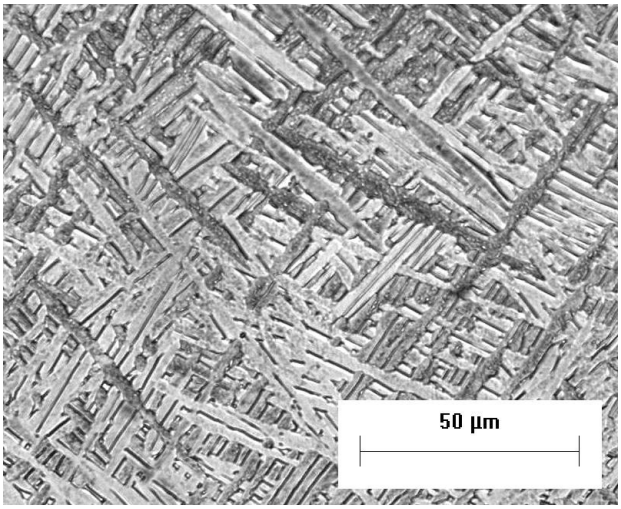

Figure 63: Nominal microstructure of sample cooled at a rate of 0.3°C/min showing a random distribution of α grains outlined in β. Average α grain width is 3.7 ± 0.7µm (~500x).

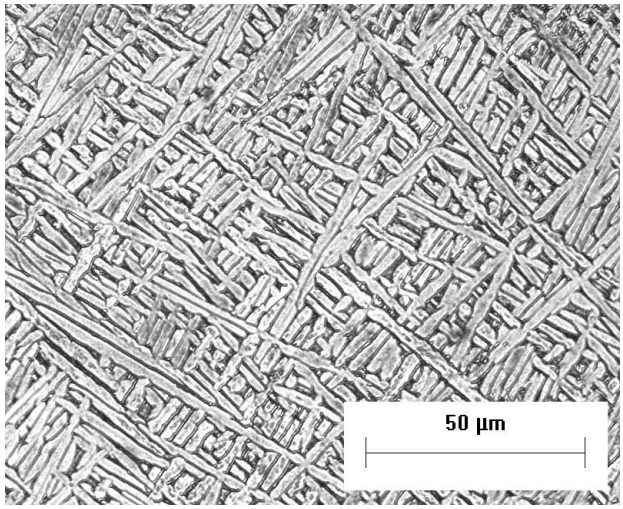

Figure 64: Nominal microstructure of sample cooled at a rate of 200°C/min showing a random distribution of α grains outlined in β. Average α grain width is 2.2 ± 0.4µm (~500x).

The heat treatment cooling rate had little effect on the microstructure other than changing the α grain width as shown in Figure 67. The α grain width measurements were made from a single micrograph of each heat treated sample with approximately 30 measurements per sample. The heat treatment doubles the width of the α grains and produces a more homogenous basketweave structure than observed in the as deposited material. The α grain width decreased slightly with an increase in the cooling rate up to 10°C/min; however, at cooling rates above 10°C/min, the α grain width remained relatively constant. The heat-treated sample cooled at a rate of 100°C/min has a larger grain width because it received two solution treatments.

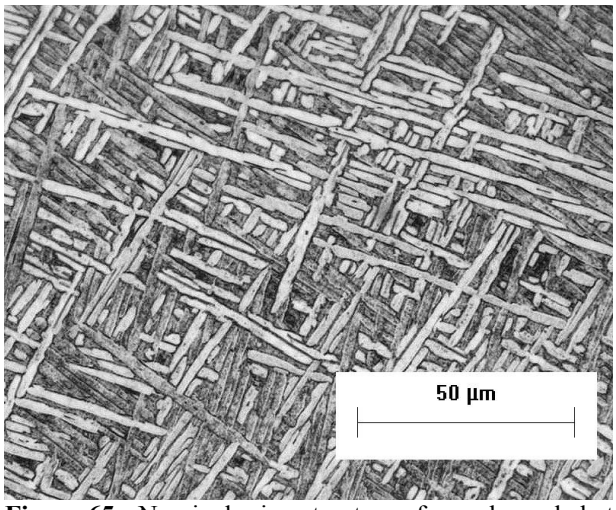

Figure 65: Nominal microstructure of sample cooled at a rate of 487°C/min showing a random distribution of a grains outlined in β . Average α grain width is 2.1 ± 0.4 µm (~500x).

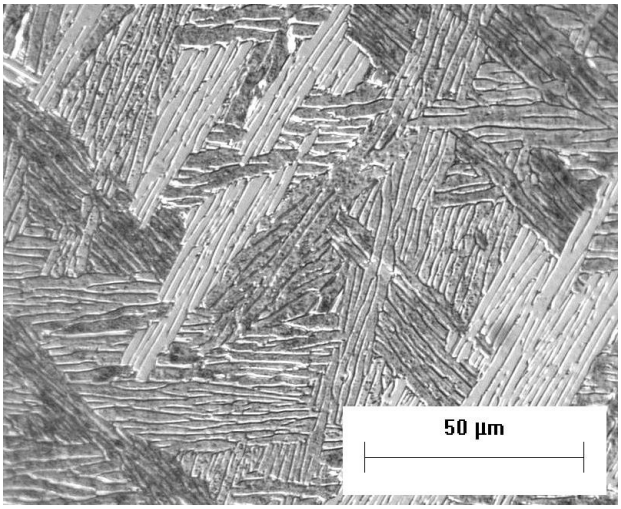

Figure 66: Layer Band microstructure of the sample cooled at 10°C/min. The layer band structure is retained during heat treatment (~500x).

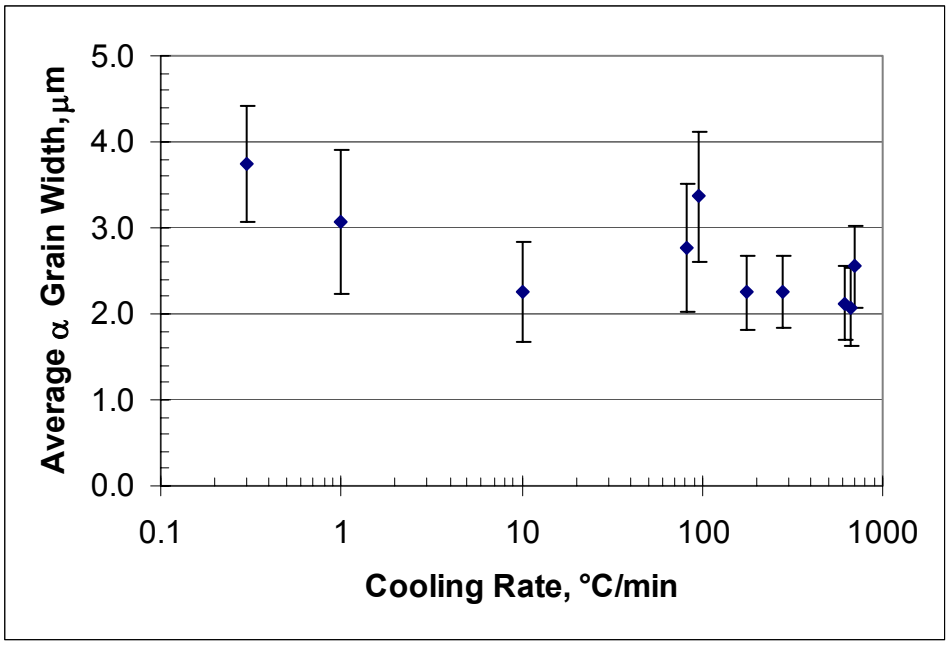

Figure 67: Change in the α grain width vs. cooling rate for the heat-treated samples. The datum point at 100°C/min received two solution treatments, which is why it has a higher grain width. Cooling rate was taken over the temperature range 900°C to 600°C.

Discussion: Heat Treatment

The heat treatment performed was a solution treat and age (STA). The solution treatment is designed to increase the volume fraction of β present at the solution treatment temperature so that upon aging the retained β will transform to fine α particles upon aging.[107] Cooling rate from the solution treatment temperature is important in the overall strengthening effect as it controls the size of the α grains and how retained β transforms to α. Faster cooling rates will result in thinner α grains and possibly transformation of retained β to α′. The aging temperature controls the size and volume fraction of the aged precipitates and ultimately, the tensile strength due to aging. Higher aging temperatures will produce coarser α precipitates and reduce the strengthening effect of the heat treatment.

The only variable in the heat treatment was the cooling rate. All samples were held at a solution treatment temperature of 913°C (70°C below the beta transus) for two hours before cooling at a rate between 0.3°C/min and 500°C/min. The aging treatment (4 hours at 538°C) was also constant for all heat-treated samples. Since the solution treatment temperature was constant, each sample is assumed to have the same microstructural morphology at 913°C just before the quenching procedure. At this temperature for a time of 2 hours, retained β would begin transforming into α, leading to α grain growth. The resulting microstructural morphology would be basketweave Widmanstätten α as was observed in the heat-treated samples.

The only microstructure-processing dependence was observed in the α grain size decreasing with cooling rate. Alpha grain growth was observed for cooling rates less than 10°C/min. For cooling rates less than 10°C/min the sample spent a sufficient amount of time high in the α+β phase during the cooling phase to allow further decomposition of any remaining retained β into α, resulting in more α grain growth. For the faster cooling rates, the α grain width did not vary in the heat-treated state, signifying that little or no decomposition of the β phase into α (further grain growth) occurred during cooling.

Martensitic transformation products were not observed in the solution treated and aged samples. It is possible that for the fastest cooling rates the retained β transformed to α′ upon quenching, but the aging treatment would have decomposed any α′ to α.

Since the heat treated microstructure was not examined between the solution and aging treatments, no quantitative conclusion can be made about the α grain growth during the solution treatment; however, some α grain growth must have occurred since the post heat treatment α grain width was essentially constant between layer bands. Recall that in the as-deposited material, a gradient in the microstructure was observed between layer bands.

Also of interest regarding the heat treatment microstructure was the presence of layer bands. The layer bands before and after heat treatment had similar α grain sizes and morphologies. Since the layer bands remained after a solution treatment in the α+β phase field, it can be concluded that they are a result of super beta transus heating.

Results: Thermal Model

The thermal model generates temperature data that is both a function of time and position; therefore, it is prudent to look at the effect that time and position have on temperature separately. In the following sections, temperature as a function of time at a fixed position in the build and temperature as a function of build height (z) at an instant in time will be examined. The results to be presented are themselves functions of the process parameter sets imposed. It would be useful for the reader to refer to the Thermal Model section, in particular Table X to review the parameter sets that are being used. In summary, Parameter Set A (PS-A) refers to a low mass deposition rate and longer dwell time, PS-B refers to a moderate mass deposition and dwell time, while PS-C refers to a high mass deposition rate and a short dwell time.

Temperature vs. Time

The temperature versus time data can be thought of as a substitute for the following experiment. If one desires to know the temperature of a fixed point in the build, a thermocouple would be inserted into the build as the laser scans overhead. The thermocouple will deliver temperature versus time data as the part is being built. When the laser is above the thermocouple, heating will occur and when the laser moves away, cooling will occur. One would observe the heating and cooling as spikes in the temperature versus time data.

Figure 68 shows the location of a node in the center of the part near the bottom of the first deposited layer (node 65: y = 0, z = 8 mm). Temperature versus time data for node 65 is plotted in Figure 69. The vertical grid lines in Figure 69 indicate the interpass time (time at which a new layer is deposited) while horizontal gridlines represent equilibrium phase change temperatures ($\alpha+\beta \leftrightarrow \beta$ = *1253 K*, $\beta \leftrightarrow \beta+L$ *=1810 K*, $\beta+L \leftrightarrow L$*=1922 K*). For reference, the thermal excursion due to the deposition of each layer (e.g., L1, L2 refer to the first and second layers deposited) and the equilibrium phases are labeled.

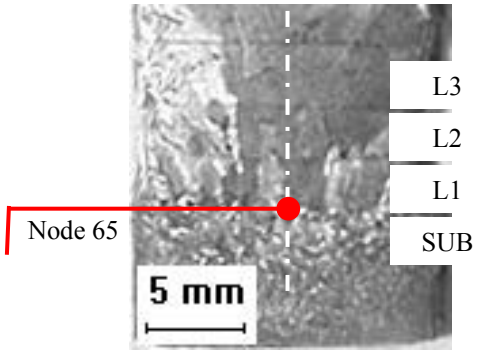

Figure 68: Macrostructure showing the location of 65 along the build centerline. Specifically, it is just above the substrate (SUB) in layer 1 (L1), having coordinates (y = 0, z = 8mm).

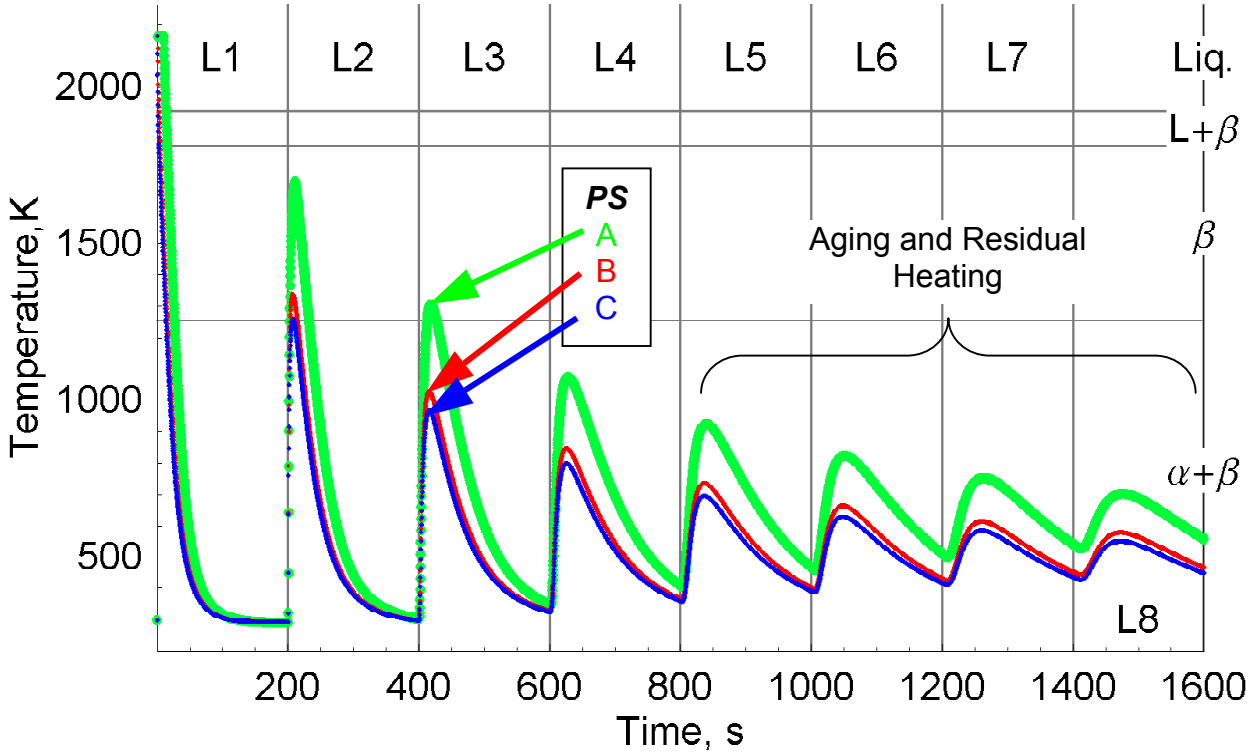

Figure 69: Thermal history of node 65 (*y=0, z=8 mm*), located at the bottom of the first layer deposited, for different parameter sets. PS-A represents a long laser dwell time and a low mass deposition rate, while PS-C represents a short laser dwell time and a high mass deposition rate. Horizontal gridlines indicate equilibrium phase transformation temperatures, while vertical gridlines indicate times corresponding to the deposition of a new layer. "Lx" refers to the thermal excursion due to the deposition layer "x."

Figure 69 illustrates the thermal history of a fixed point (hereafter referred to as node 65) as a result of applying different processing parameters. Examining PS-A at $t = 0$, the temperature is $T_{base} = 298K$ as was prescribed in the initial boundary conditions. Immediately, the laser is "switched" on, depositing a new layer (L1) having a temperature of $T_{laser} = 2162K$. Node 65, along with the rest of the nodes in L1, is held at T_{laser} for a time $t_{dwell} = 10$ s. After t_{dwell} has expired, the entire part is allowed to cool. Cooling is initially rapid (30 K / s) for node 65; however, after approximately 100 seconds of cooling, the part has attained a steady state temperature of $T_{base} = 298K$. After 200 seconds have expired the laser has returned to the same x position in the build, and the laser deposits the second layer (L2) on top of L1, thereby heating the underlying material. As a result, node 65 reaches temperatures high in the β phase field as shown in Figure 69. Node 65 experiences a cooling rate around (20 K/s) upon cooling from this β excursion. Also note that it takes the full 190 seconds ($t_{pass} - t_{dwell} = 190$s) for node 65 to cool to room temperature. After a total running time of 400 seconds, the laser deposits the third layer (L3) of material on top of L1 and L2, causing node 65 to again be heated into the β phase field

but to a lesser extent than was experienced during the deposition of L2. The cooling rate is also reduced to approximately 10 K/s. After being allowed to cool for 190 seconds, node 65 has only cooled to approximately 350 K, indicating that residual heating is occurring in the part. During the deposition of layers 4, 5, 6, 7, and 8, node 65 sees heating into the α+β phase field; the maximum temperature of this heat and the cooling rate from the peak temperature is reduced with the deposition of subsequent layers. Also, residual heat continues to build-up in the part reaching nearly 600K after the deposition of the eighth layer.

Similar trends in the temperature versus time data are observed for PS-B and PS-C, with the peak temperatures and residual heating being the least for PS-C (short dwell time, high mass deposition rate). Qualitatively it appears that the cooling rate from the peak temperature is independent of parameter set. PS-A experienced three excursions into the β phase field while PS-B and PS-C only experienced two excursions into the β phase field.

Temperature vs. Build Height

Temperature as a function of position is analogous to looking at a snapshot at an instant in time of the temperature profile recorded by many thermocouples placed along the build height. Temperature as a function of build height (z) is useful in determining the depth of heating either into the beta, liquid plus beta, or liquid phase fields as well as an understanding of the thermal gradients and residual thermal stresses that arise as a result of the thermal cycling. Figure 70 shows the temperature dependence on build height and different parameter sets for a fixed y-position (y = 0mm) and two different times during the deposition of the 8th layer (L8). Again, horizontal gridlines represent the equilibrium phase transformation boundaries while the vertical gridlines in Figure 70 represent the position of each layer. For comparison with Figure 69, Node 65 is labeled.

From Figure 69 we see that L8 is deposited at a time t = 1400 s. Figure 70 plots data for t = 1405 seconds and t = 1445 seconds. In Figure 70 at a total build time of t = 1405 seconds, each parameter set is at a different stage of the build. For PS-A, the laser is still heating the build as indicated by the constant temperature (T_{laser} = 2162 K) and will continue to heat for another 5 seconds. For PS-B and PS-C, the part has been cooling for 4 and 4.75 seconds, respectively. For PS-A at t = 1405 s a steep thermal gradient (≈110 $°C \cdot mm^{-1}$) is present as a result of the laser heating; the thermal gradients for PS-B and PS-C are still quite high, but not as severe as in PS-A. It is also interesting that at t = 1405s, the top half of L8 is still molten for PS-B, while the same region for PS-C is in the mushy zone. For PS-A, most of L7 is either in the mushy zone or molten.

After the PS-A build is allowed to cool for 35 seconds (t = 1445s) the thermal gradient is reduced to (≈40 $°C \cdot mm^{-1}$). The build using PS-A achieves a maximum β heating depth of 22 mm, or about 4 layers of after cooling for 35 seconds. The β heating depth in the PS-B results after cooling for 44 seconds is approximately two layers. For PS-C, the entire build is at a temperature less than the β transus after 44.75 seconds of cooling.

Examining Figure 70 at the bottom of L7 (z ≈ 36mm), the temperatures at both plotted

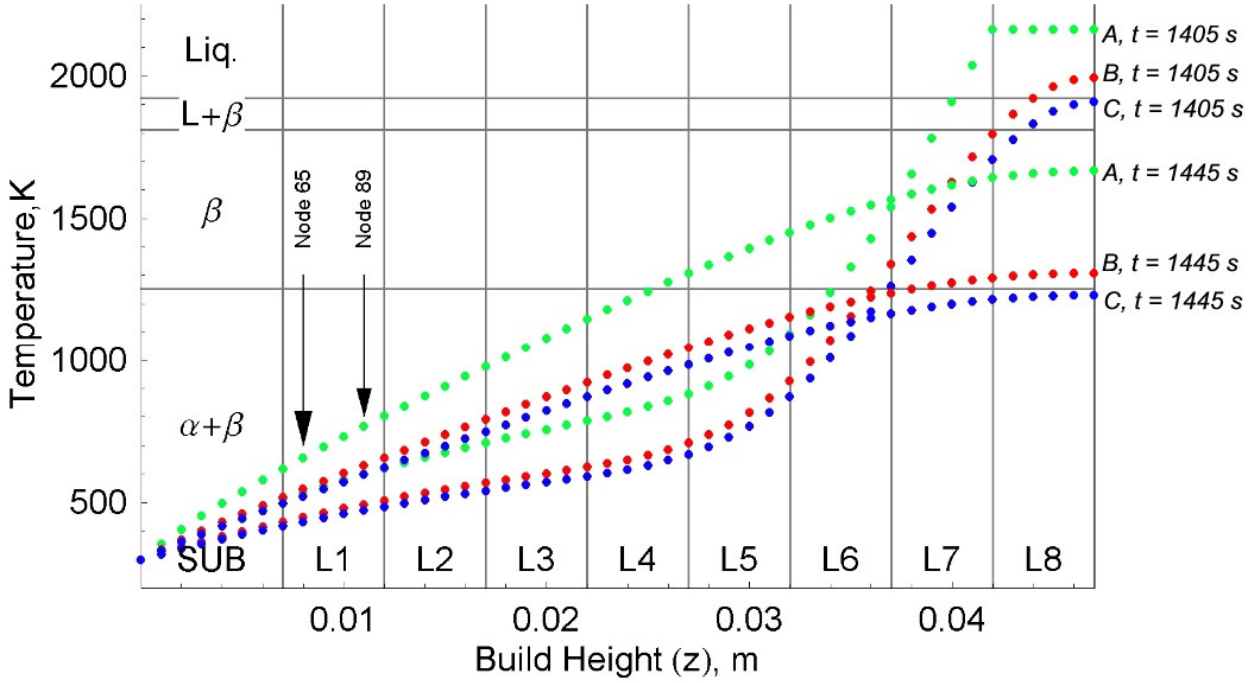

Figure 70: Temperature as a function of build height (z-direction) and different parameter sets for a fixed y-position (y = 0mm) and two different times during the deposition of the eight layer (L8). The total build time for this part is 1600 s. The labels SUB, L1, L2, etc., serve to label each layer.

times are equivalent for each parameter set. The position $z \approx 36$ mm represents the crossover point for heating and cooling at the two plotted times. For $z > 36$ mm, the build is cooling, while for $z < 36$ mm, the build is heating. The temperature and not the z-position of the crossover point appears to be dependent on the parameter set.

Discussion: Thermal Model

Temperature vs. Time

The most important features from Figure 69 are the number and extent of the excursions into the β phase field, residual heating of the part as more layers are deposited, and cooling rate from the peak temperature of each thermal excursion. Excursions into the β phase field (L2-L3) that are of sufficient time and temperature will lead to a transformation from α+β to the β phase. Ultimately this will result in a change in the microstructural morphology. It is evident from Figure 69 that increasing the dwell time increases the amount of heat input to the build, thereby increasing the peak temperatures observed at a given location and the number of times that location experiences excursions into the β phase field. Increasing the dwell time also widens the thermal excursion peaks, resulting in more time for the phase transformation to occur.

Thermal excursions into the α+β phase field (L4-L8) will result in aging of the material as indicated in Figure 69. Aging will result in decomposition of any martensitic transformation products and possible relief of residual thermal stresses that may have evolved as a result of the rapid cooling rate experienced during initial deposition. Residual heating aids in the aging process allowing a region of the part to remain in the temperature range where aging may take place.

Temperature vs. Build Height

It is apparent from Figure 69 and Figure 70 that the thermal behavior in this process is quite complex. A fixed point in the build experiences a thermal excursion for each new layer that is deposited with the severity of the thermal excursion decreasing for this fixed point as more layers are added (i.e. the heat source moves further away). When a new layer is deposited, high thermal gradients on the order of 100 K/mm develop in the build and decrease with time. The dynamic nature of this process becomes apparent when one examines temperature in Figure 69 and Figure 70 for node 65 at times of 1405 and 1445 seconds. The temperature of node 65 is greater at t = 1445 seconds than at t = 1405 seconds, while at the same times for a *z*-position greater than L7 ($z > 37$mm), cooling is occurring. Figure 69 shows that node 65 will continue to heat for an addition 30 seconds past t = 1445 seconds. Hence there exists a region low in the

build that is still heating while a region at the top of the build is cooling. The crossover point can be illustrated as a thermal wave moving in the negative z direction (top to bottom), where ahead of the thermal wave heating occurs and behind the wave cooling occurs. The speed of the wave is determined by the thermal conductivity of the deposited material.

Thermal Model and Microstructural Evolution

A possible path for the microstructural evolution in DMD Ti-6Al-4V was discussed for the as-deposited microstructure. The thermal model tells us quantitatively the temperature the build experiences as a function of time and position. This information can be used to check the theory based on microstructural observations that the gradient microstructure observed in layer *n* is a result of the deposition of layer *n+2*, and the layer band for layer *n* forms as a result of the deposition of layer *n+3*.

It will be intuitive to first look at a node closer to the top of a deposited layer as shown in Figure 71. Node 89 is located 1mm from the top of L1 at a position of y = 0, z = 11mm. In

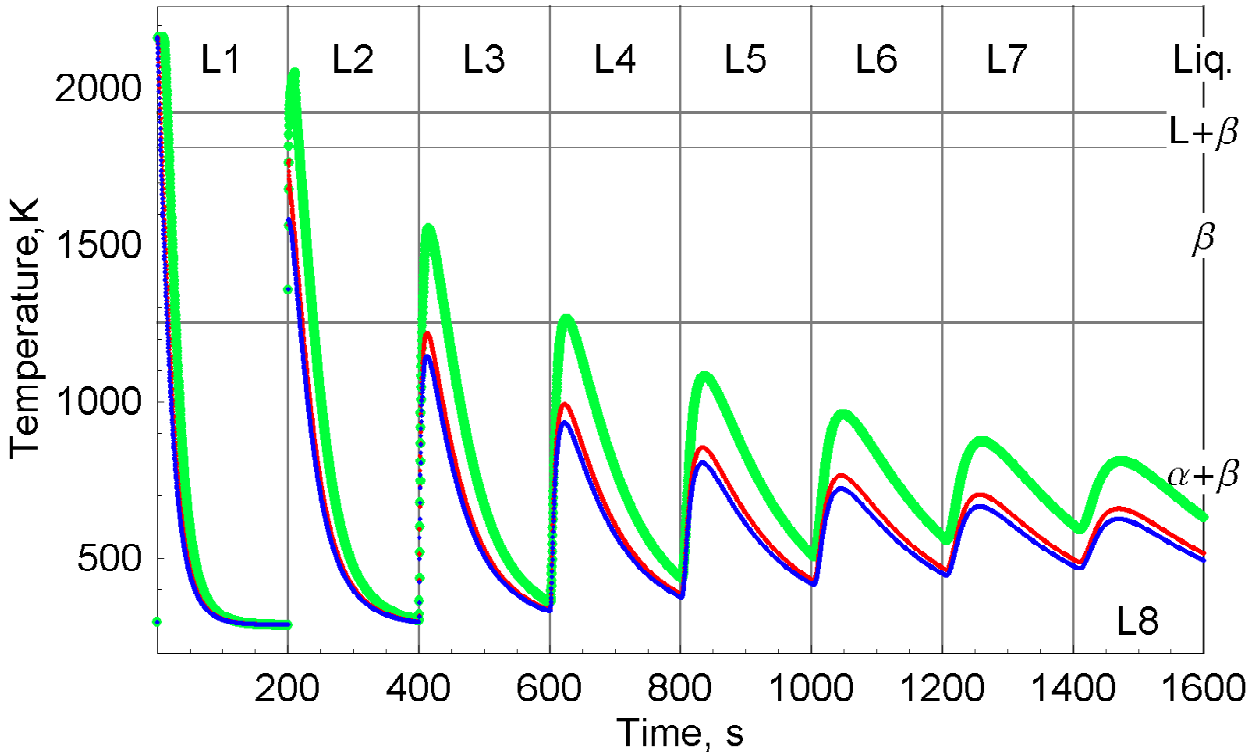

Figure 71: Thermal history of node 89 (*y=0, z=11 mm*), located at the top of the first layer deposited, for different parameter sets. PS-A represents a long laser dwell time and a low mass deposition rate, while PS-A represents a short laser dwell time and a high mass deposition rate. Horizontal gridlines indicate equilibrium phase transformation temperatures, while vertical gridlines indicate times corresponding to the deposition of a new layer. "Lx" refers to the thermal excursion due to the deposition layer "x."

Figure 71 we only need for this analysis to focus on the first four layers deposited (L1-L4) because it is theorized that over a four layer span is where the relevant phase transformations are taking place. The discussion will also be limited to PS-A, the long dwell time, high mass deposition rate build.

When L1 is deposited, it is initially molten, cooling very rapidly to room temperature within 1 minute, resulting in a colony α morphology having very fine α grains. Next, L2 is deposited raising the temperature of node 89 to about 2100 K, or about 200 K above the melting point. It is also seen in Figure 70 that the depth of melting in L7 due to the deposition of L8 is approximately half of L7 or 3 mm for PS-A. As a result of a good portion of L1 being remelted, the colony morphology that initially formed (most likely due to segregation) will be erased. The final morphology in L1 after the deposition of L2 will be a fine basketweave α due to the rapid cooling rate. Continuing with the deposition of L3, node 89 sees an excursion into the β phase field of about 1500K (250K above the beta transus) that lasts for about 50 seconds. It was proposed that the deposition of L3 (*n+2*) should lead to the gradient α morphology in L1 (*n*); however, it is known[31] that increasing the β excursion temperature and time and decreasing cooling rate from the β phase field will favor formation of the colony morphology. Therefore, because the excursion into the beta phase field is so strong, the colony morphology would be expected in the vicinity of node 89. Examining Figure 69 we see that node 65 experiences a much weaker excursion into the β phase field during the deposition of L3, consequently, we would expect and in fact observe the basketweave morphology to be present. An argument can also be made for the transition from a fine basketweave α near node 65 to a colony morphology near node 89 by seeing that as we increase the z position the β excursions will continuously become stronger until a point is reached where the time and temperature of the β excursion are sufficient to form the colony morphology. If the β excursion is not strong enough to form the colony morphology an increase in α grain size will occur. When L4 is deposited, node 89 will be the only node in L1 to see an excursion into the β phase field. Since this excursion is weak, a colony morphology will not be formed, instead the α grains present will coarsen.

What has been described thus far using the thermal model data is that the layer band and gradient α morphologies form in layer *n* due to the deposition of layer *n+2*. Following this logic, there will be a gradient morphology in L16, but there should also be a layer band present at

the top of L16, which was not observed in the deposit. Currently, the only explanation for this shortcoming in the analysis of microstructural evolution using the thermal model are that the parameter set used in the thermal model was not the same as the one used to build the part. The parameter set for the build examined in this work is proprietary and therefore unknown.

Chapter 5:

Conclusion

As Deposited Macro and Microstructure

Optical microscopy was used to reveal the macro and microstructure of the as-deposited material. Table XIV summarizes some of the important measurements made of the macro and microstructural features. The as-deposited macrostructural features consisted of large prior columnar beta grains, a well defined heat affected zone in the substrate, and the presence of a macroscopic bands (termed layer bands) observed at every deposited layer except for the last three layers to be deposited. The prior beta grains are columnar in nature, oriented nearly perpendicular to the substrate with a slight bias in the direction of laser motion, grow across multiple deposited layers, and are outlined in continuous α phase. During solidification of the melt, the prior beta grains grow epitaxially from grains in the base metal or previously deposited layers.

The nominal deposit microstructure located between each layer band consisted of a basketweave Widmanstätten α morphology that exhibited a gradient in the α grain size with finer α grains at the bottom of a layer and coarser grains near the top of a layer. The layer band structure consisted of colonies of coarse acicular Widmanstätten α. In both morphologies, the α grains were acicular in nature and outlined in untransformed β.

Compositional analyses were made in regions containing the layer band and nominal microstructural morphologies and it was determined that they were not a result of segregation (i.e., there was no systematic variation in composition). It was also determined through hardness measurements that the layer band was not a result of oxidation (i.e., oxygen stabilizing the α phase, which results in a harder region). The observed variations in the as-deposited microstructure are a result of the complex thermal cycling experienced in different regions as a part is built.

The microstructure observed in the deposition of the last four layers contains clues to the evolution of the gradient α and the layer bands morphologies. The last layer to be deposited also exhibited a colony morphology containing fine α grains. The second to last layer deposited exhibited a fine basketweave morphology, while the third to last layer deposited exhibited the nominal morphology. The fourth to last layer deposited exhibited the nominal microstructure culminating in a layer band. Using an argument based on microstructural observations, it was

concluded that the gradient α and layer band morphologies form in layer *n* due to the deposition of layer *n+2* and *n+3*, respectively.

Table XIV: Summary of As-Deposited Measurements

	Measurement	***Average***	***Standard Deviation***		***Count***	***Samples***
Macro Features	Prior Beta Grain Width (Deposit)	1.39	0.81	mm	222	4
	Fusion Zone Depth	1.05	0.22	mm	13	3
	HAZ Depth	4.48	1.43	mm	7	3
Layer Band	Spacing	2.94	0.49	mm	141	4
	Width	165.75	28.52	µm	295	4
	Colony Width	13.19	7.17	µm	872	4
Alpha Grain Width	All	1.12	0.52	µm	1415	4
	Bottom of Layer	0.92	0.38	µm	389	4
	Middle of Layer	1.01	0.33	µm	411	4
	Top of Layer	1.57	0.59	µm	397	4
	Top of Part	0.90	0.38	µm	218	3
Vickers Micro Hardness	Layer Band	347	13	HV_{300gf}	17	1
	Between Layer Band	351	21	HV_{300gf}	17	1
Vickers Macro Hardness	All Data	344	7	HV_{20kgf}	40	1
	All Data, No HAZ	345	6	HV_{20kgf}	35	1
	Layer Band	346	4	HV_{20kgf}	13	1
	Between Layer Band	346	6	HV_{20kgf}	16	1

Heat Treatment

The as-deposited material was solution treated at 913°C for 2 hours followed variable quench to 315°C at cooling rates ranging from 0.3°C/min to 500°C/min. An aging treatment at 538°C for 4 hours followed by a furnace cool to room temperature followed the solution treatment. The resulting microstructure was basketweave acicular α having a constant grain size and uniform morphology throughout the deposit, with the exception of the presence of layer bands. The gradient in α grain size between the layer bands was eliminated after the heat treatment; however, the layer band morphology remained suggesting that their formation is a result of super beta transus heating. For heat treatments having cooling rates less than 10°C/min slightly higher α grain widths between 3 and 4 μm were observed. For cooling rates faster than 10°C/min, a relatively constant α grain width of 2.4μm was observed. The larger grain widths at slower cooling rates is attributed to extended time high in the α+β phase field where retained β can transform to α. No metastable transformation products such as α′ were observed in the heat treated material.

Thermal Model

The thermal behavior experienced during the deposition is very complex. For example local regions of the part are heated into different phase fields at different temperatures and for different amounts of time, cooling rates and thermal gradients are ever-present, and heating and cooling of the part can be occurring simultaneously. Thus in order to understand the microstructure that has evolved, an understanding of the thermal behavior must be obtained. The thermal behavior is dominated by the processing parameters and to some extent the material properties. The analysis of the thermal model data that has been presented is by no means exhaustive; however, it does provide insight into what is actually happening with regards to temperature as a function of position, time, and processing parameters during the direct metal deposition process.

The extent of the temperature excursions and residual heating were found to increase with dwell time. This would be expected since longer dwell times lead to increased heating of the part. It appears as though the cooling rate and thermal gradients are not highly dependent upon dwell time.

A hypothesis for the microstructural evolution in the PS-A deposit was made using temperature versus time and position plots for nodes near the bottom and top of the first deposited layer. It was observed in the temperature versus position plots that remelting of a layer *n* by deposition of layer *n+1* was sufficient to eliminate the initial fine colony-like microstructure that was likely caused by melt pool segregation. It was concluded that the gradient basketweave Widmanstätten α morphology and the colony Widmanstätten α morphology form in layer *n* as a result of the deposition of layer *n+2*. This is a result of the lower regions of layer *n* seeing weaker excursions into the β phase field producing a graded basketweave morphology while the top of layer *n* sees a strong beta excursion. Subsequent beta excursions are not sufficient to change the colony morphology. This logic does not agree completely with what was observed in the deposit for the last four layers to be deposited. A gradient morphology and a layer band would be expected in L16; however, this is not observed in the deposit microstructure. The lack of agreement for evolution theories based on microstructural observations and thermal model results is most likely due to the fact that certain processing parameters such as dwell time and

superheat temperature are best-guess estimates as to the parameters used to build the deposit examined in this work.

Future Work

Future directions to be explored with this research deal with the evolution of microstructure and thermal modeling in DMD processes (not necessarily Laser Forming). First, a better understanding of the layer band phenomena is needed in DMD of Ti-6Al-4V. To this end, experimental work must be done to simulate the thermal cycles experienced in the build. A simple experiment to simulate the thermal cycling would be to heat a bar of titanium to different temperatures and for different times to see if the layer band and gradient α morphologies can be obtained. Similarly, it would be extremely useful to know temperatures and times above the beta transus where the layer band morphology will form. This can easily be done using the vacuum heat treatment furnace. Even more useful data would be determination of the phase transformations that take place *in situ* using spatially and time resolved x-ray diffraction techniques. Elmer, et. al.[108] have used this technique to determine phase transformations in titanium and steel welds. If time-temperature-transformation data for DMD processes were coupled with process thermal model data, an extremely useful tool would be at the disposal of those interested in the DMD process.

The thermal model is a work in progress. The first step is to validate the model with published experimental data for the LENS process. Second, improvements need to be made in the efficiency of the model, including variable time step methods for builds that attain a steady state temperature, where larger time steps can be used. Also, solidification (change of phase) needs to be considered in the thermal model in order to better model DMD process. The final step in the evolution of the model will be to couple the thermal data generated with a phase transformation model so that microstructural features based on composition and thermal cycling can be determined given a set of processing conditions. This will make the model applicable for use in determining process conditions for functionally gradient materials – components that have tailored properties in different regions to suit the application. For any future study using the thermal model, process parameters must be known before one can begin to fully analyze the thermal model results.

Appendices

Appendix A: Thermal Model Flow Chart

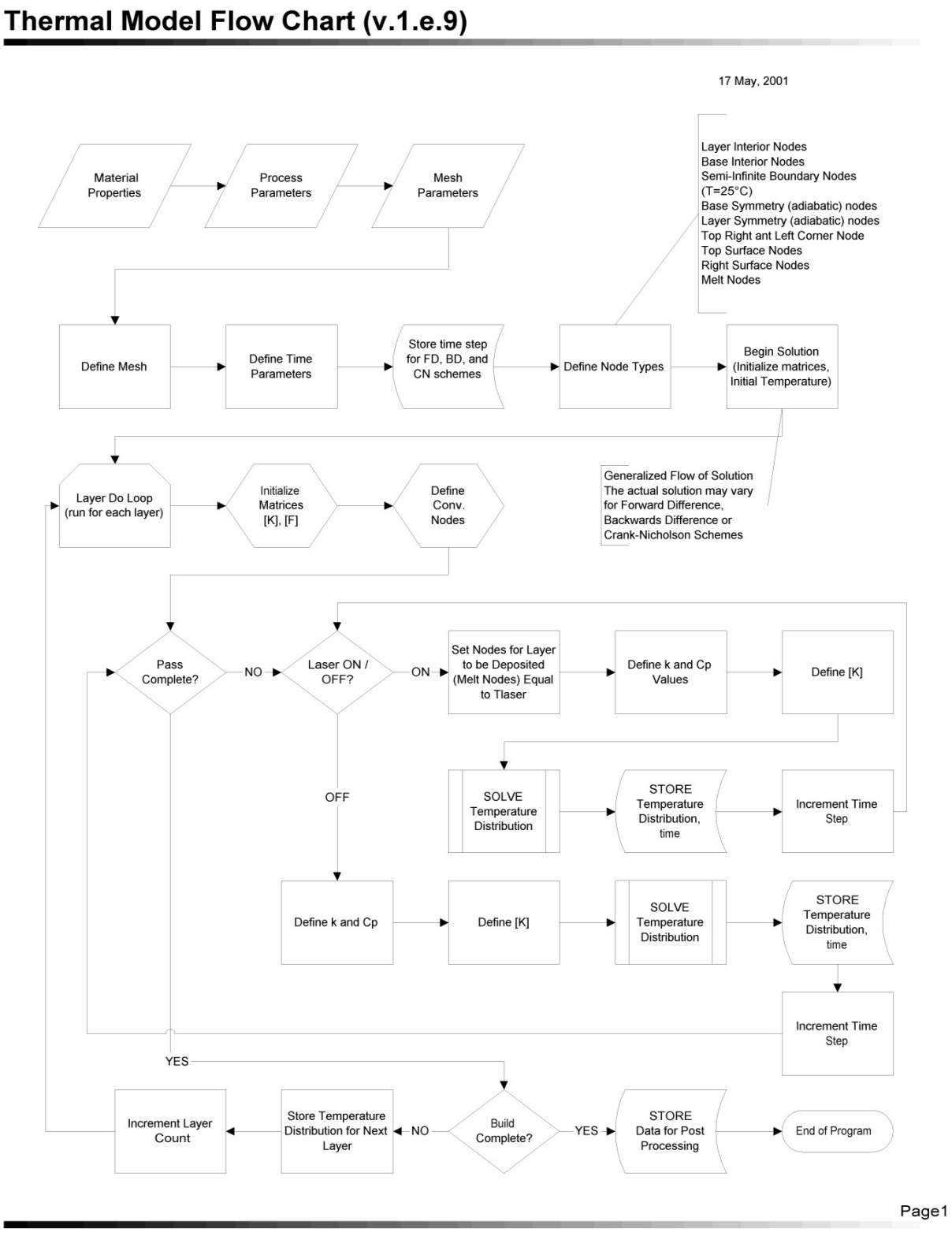

Figure 72: Thermal Model Flow Chart

Appendix B: Statistics

Anova: Single Factor 0.05

SUMMARY

Groups	*Count*	*Sum*	*Average*	*Variance*
Bottom	389	356.3404	0.916042	0.14553
Middle	389	389.1288	1.000331	0.09923
Top	389	615.3947	1.581992	0.343694

ANOVA

Source of Variation	*SS*	*df*	*MS*	*F*	*P-value*	*F crit*
Between Groups	102.2969	2	51.14845	260.7601	2.66E-94	3.00345
Within Groups	228.3202	1164	0.196151			
Total	330.6171	1166				

Conclusion: Reject Ho, Means Unequal

Figure 73: ANOVA to test the null hypothesis that the alpha grain width measurements made at the bottom, middle, and top of a layer have equal means using a confidence level of 0.05. The null hypothesis is rejected because F > Fcrit. There is statistical difference between the alpha grain size at the bottom, middle and top of a layer.

t-Test: Two-Sample Assuming Unequal Variances		0.01
	Bottom	*Middle*
Mean	0.916042232	1.000331153
Variance	0.145530185	0.099230429
Observations	389	389
Hypothesized Mean Difference	0	
df	749	
	-	
t Stat	3.360272733	
P(T<=t) one-tail	0.000409053	
t Critical one-tail	2.331335054	
P(T<=t) two-tail	0.000818106	
t Critical two-tail	2.582419256	
Conclusion:	**Reject Ho, Means Unequal**	

t-Test: Two-Sample Assuming Unequal Variances		0.01
	Middle	*Top*
Mean	1.000331153	1.58199159
Variance	0.099230429	0.343693539
Observations	389	389
Hypothesized Mean Difference	0	
df	595	
	-	
t Stat	17.23771654	
P(T<=t) one-tail	1.30587E-54	
t Critical one-tail	2.332635631	
P(T<=t) two-tail	2.61174E-54	
t Critical two-tail	2.584110916	
Conclusion:	**Reject Ho, Means Unequal**	

Figure 74: Student t-tests to test the null hypothesis that the alpha grain width measurements made at the bottom, middle, and middle and top of a layer have equal means using a confidence level of 0.05. The null hypothesis is rejected in both instances because t stat < - tcritical two-tail. There is statistical difference between the alpha grain size at the bottom and middle and middle and top of a layer.

Anova: Single Factor 0.01

SUMMARY

Groups	*Count*	*Sum*	*Average*	*Variance*
LB	39	13390.111	343.336	38.748
OFF	66	22835.765	345.996	32.628

ANOVA

Source of Variation	*SS*	*df*	*MS*	*F*	*P-value*	*F crit*
Between Groups	173.487	1	173.487	4.973	0.028	6.887
Within Groups	3593.218	103	34.886			
Total	3766.705	104				

Conclusion: Accept Ho, Means Similar

Figure 75: ANOVA to test the null hypothesis that the hardness on and off a layer band is the same for a confidence interval of 0.01. The null hypothesis is accepted because F < Fcrit. There is no statistical difference in the hardness on or off a layer band.

t-Test: Two-Sample Assuming Unequal Variances

		0.01
	LB	*OFF*
Mean	343.336	345.996
Variance	38.748	32.628
Observations	39	66
Hypothesized Mean Difference	0.000	
df	74	
t Stat	-2.181	
P(T<=t) one-tail	0.016	
t Critical one-tail	2.378	
P(T<=t) two-tail	0.032	
t Critical two-tail	2.644	
Conclusion:	**Accept Ho, Means Similar**	

t-Test: Two-Sample Assuming Equal Variances

		0.01
	LB	*OFF*
Mean	343.336	345.996
Variance	38.748	32.628
Observations	39	66
Pooled Variance	34.886	
Hypothesized Mean Difference	0	
df	103	
t Stat	-2.230	
P(T<=t) one-tail	0.014	
t Critical one-tail	2.363	
P(T<=t) two-tail	0.028	
t Critical two-tail	2.624	
Conclusion:	**Accept Ho, Means Similar**	

Figure 76: Student's t-tests to test the null hypothesis that the hardness on and off a layer band is the same for a confidence interval of 0.01. The null hypothesis is accepted because t stat > - t crit. There is no statistical difference in the hardness on or off a layer band.

Appendix C: Finite Difference Equations

Transient- Implicit Finite Difference Schemes

■ Temperature Independent Properties

In the backward-difference or implicit scheme, the new temperature of any node depends on the new temperature of it's neighbors, which are generally unknown. The implicit method is unconditionally stable, i.e., the solution remains stable for all space and time intervals. This scheme is first order accurate in time and second order accurate in space, i.e $O[\Delta t, (\Delta x)^2]$.

▪ Interior Node

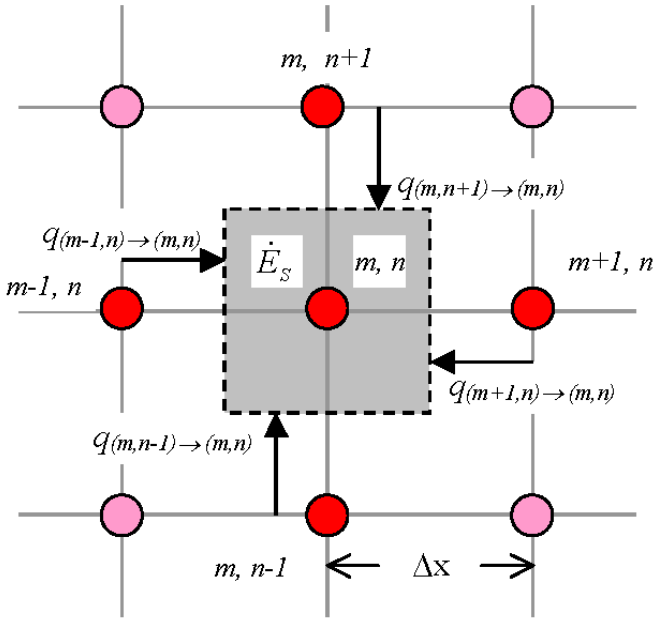

We begin by using the energy balance method to balance the energy entering ($\dot{E}_{\text{in}}$) plus the energy generated in control volume ($\dot{E}_g$) with the energy stored in the control volume ($\dot{E}_{\text{st}}$).

$\dot{E}_{\text{in}} + \dot{E}_g = \dot{E}_{\text{st}}$

Heat enters the control volume from each of the surrounding red nodes and the contribution from each of the surrounding nodes is taken into acount in the $\dot{E}_{\text{in}}$ term. In general, $\dot{E}_{\text{in}} = \sum_{i=1}^{4} q_{(i \to m,n)}$

(1) $q_{(m,n+1)\to(m,n)} = k\,A\,\frac{(T_{m,n+1}-T_{m,n})}{\Delta y}, \quad A = \Delta x \cdot 1$

(2) $q_{(m+1,n)\to(m,n)} = k\,A\,\frac{(T_{m+1,n}-T_{m,n})}{\Delta x}, \quad A = \Delta y \cdot 1$

(3) $q_{(m,n-1)\to(m,n)} = k\,A\,\frac{(T_{m,n-1}-T_{m,n})}{\Delta y}, \quad A = \Delta x \cdot 1$

(4) $q_{(m-1,n)\to(m,n)} = k\,A\,\frac{(T_{m-1,n}-T_{m,n})}{\Delta x}, \quad A = \Delta y \cdot 1$

The area term is the area of control volume surface normal to the direction of heat flow, and the denominator is the direction in which heat is flowing. Also note that the local node numbering system begins with *m, n+1* and proceeds clockwise.

The energy generation term is $\dot{q}(A \cdot \Delta x)$, where $A = 1 \cdot \Delta y$.

Now we consider the storage term:

$\dot{E}_{\text{st}} = \rho\, C\, V\, \frac{T_{m,n}^{p+1} - T_{m,n}^{p}}{\Delta t}$,

where,

$V = A \cdot \Delta x$.

In the implicit method the storage term has been discretized in time such that we are intersted in finding the $T_{m,n}^{p}$ term, which corresponds to the temperature of node m, n at the current time step, p. The temperature of all nodes at the next time step will be solved for simultaneously. The temperature of node $T_{m,n}^{p}$ is either known from the initial temperature distribution or was calculated at the previos time step.

We are now ready to derive the finite difference equation for an interior node. We assume a uniform mesh, i.e. $\Delta x = \Delta y$.

$\dot{E}_{\text{in}} + \dot{E}_g = \dot{E}_{\text{st}}$

such that :

$$k\,A\,\frac{(T_{m,n+1}^{p+1}-T_{m,n}^{p+1})}{\Delta y} + k\,A\,\frac{(T_{m+1,n}^{p+1}-T_{m,n}^{p+1})}{\Delta x} + k\,A\,\frac{(T_{m,n-1}^{p+1}-T_{m,n}^{p+1})}{\Delta y} + k\,A\,\frac{(T_{m-1,n}^{p+1}-T_{m,n}^{p+1})}{\Delta x} + \dot{q}\,\Delta x \cdot A = \rho\, C A \cdot \Delta x\,\frac{T_{m,n}^{p+1} - T_{m,n}^{p}}{\Delta t}$$

Divide by k and A, multiply by Δx, and introduce $\alpha = \frac{k}{\rho C}$:

$$\left(T_{m,n+1}^{p+1} - T_{m,n}^{p+1}\right) + \left(T_{m+1,n}^{p+1} - T_{m,n}^{p+1}\right) + \left(T_{m,n-1}^{p+1} - T_{m,n}^{p}\right) + \left(T_{m-1,n}^{p+1} - T_{m,n}^{p+1}\right) + \frac{\dot{q}\,\Delta x^2}{k} = \frac{1}{\alpha}\,\frac{\Delta x^2}{\Delta t}\,\left(T_{m,n}^{p+1} - T_{m,n}^{p}\right)$$

Recognize that $\text{Fo} = \frac{\alpha \Delta t}{\Delta x^2}$:

$$T_{m,n+1}^{p+1} + T_{m+1,n}^{p+1} + T_{m,n-1}^{p+1} + T_{m-1,n}^{p+1} - 4\,T_{m,n}^{p+1} + \frac{\dot{q}\,\Delta x^2}{k} = \frac{1}{\text{Fo}}\,\left(T_{m,n}^{p+1} - T_{m,n}^{p}\right)$$

Rearranging, we have the final form :

$$(1 + 4\,\text{Fo})\,T_{m,n}^{p+1} - \text{Fo}\left(T_{m,n+1}^{p+1} + T_{m+1,n}^{p+1} + T_{m,n-1}^{p+1} + T_{m-1,n}^{p+1}\right) - \frac{\dot{q}\,\text{Fo}\,\Delta x^2}{k} = T_{m,n}^{p}$$

If there is no internal heat generation, set $\dot{q} = 0$.

■ Surface Node with Convection or Constant Heat Flux

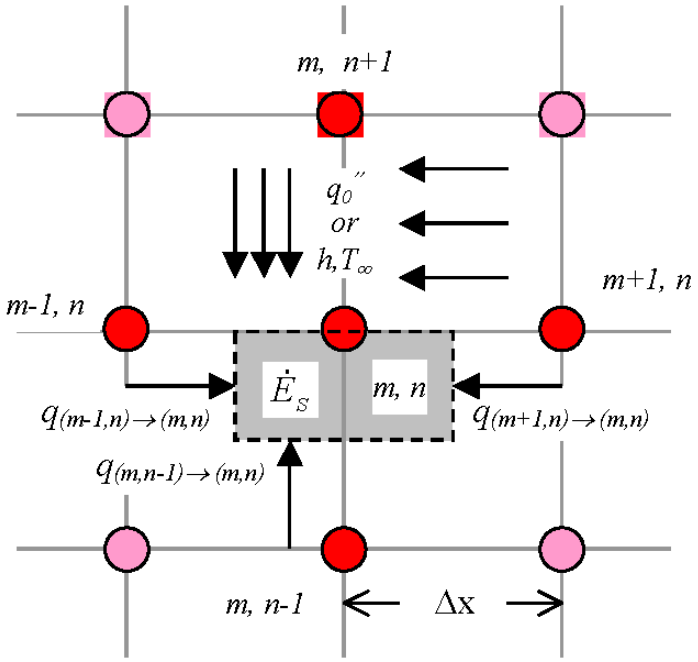

■ *Constant Heat Flux*

The energy method will be used to derive the finite difference equation for the surface node. First we consider a constant heat flux, q_0'' ($\frac{W}{m^2}$), acting upon node m, n, no internal heat generation, and a uniform mesh.

$\dot{E}_{in} = \dot{E}_{st}$, where

$\dot{E}_{st} = \rho\, C\, V\, \frac{T_{m,n}^{p+1} - T_{m,n}^{p}}{\Delta t}$, $V = \Delta x \cdot \frac{\Delta x}{2} \cdot 1 = \frac{\Delta x^2}{2} \cdot 1$ (m^3)

and,

$\dot{E}_{in} = \sum_{i=1}^{4} q''_{(i\to m,\,n)} \cdot A$.

The heat flux terms are as follows:

(1) $q_{(m,n+1)\to(m,n)} = q_0'' \cdot A$, $A = \Delta x \cdot 1$

(2) $q_{(m+1,n)\to(m,n)} = k\, A\, \frac{(T_{m+1,n} - T_{m,n})}{\Delta x}$, $A = \frac{\Delta y}{2} \cdot 1$

(3) $q_{(m,n-1)\to(m,n)} = k\, A\, \frac{(T_{m,n-1} - T_{m,n})}{\Delta y}$, $A = \Delta x \cdot 1$

(4) $q_{(m-1,n)\to(m,n)} = k\, A\, \frac{(T_{m-1,n} - T_{m,n})}{\Delta x}$, $A = \frac{\Delta y}{2} \cdot 1$

Summing and equating appropriate terms

$$q''_0\,(\Delta x\cdot 1)+k\,\frac{\Delta x}{2}\,\frac{\left(T^{p+1}_{m+1,n}-T^{p+1}_{m,n}\right)}{\Delta x}+k\,\Delta x\,\frac{\left(T^{p+1}_{m,n-1}-T^{p+1}_{m,n}\right)}{\Delta y}+k\,\frac{\Delta x}{2}\,\frac{\left(T^{p+1}_{m-1,n}-T^{p+1}_{m,n}\right)}{\Delta x}=\rho\,C\,\frac{\Delta x^2}{2}\,\frac{T^{p+1}_{m,n}-T^{p}_{m,n}}{\Delta t}$$

Divide by k, multiply by 2, cancel like terms (Δx and Δy), and introduce $\alpha=\frac{k}{\rho C}$:

$$\frac{2\,q''_0\,\Delta x}{k}+\left(T^{p+1}_{m+1,n}-T^{p+1}_{m,n}\right)+2\left(T^{p+1}_{m,n-1}-T^{p}_{m,n}\right)+\left(T^{p+1}_{m-1,n}-T^{p+1}_{m,n}\right)=\frac{1}{\alpha}\,\frac{\Delta x^2}{\Delta t}\,(T^{p+1}_{m,n}-T^{p}_{m,n})$$

Recognize that $\mathrm{Fo}=\frac{\alpha\,\Delta t}{\Delta x^2}$:

$$\frac{2\,q''_0\,\Delta x}{k}+T^{p+1}_{m+1,n}+2\,T^{p+1}_{m,n-1}+T^{p+1}_{m-1,n}-4\,T^{p+1}_{m,n}=\frac{1}{\mathrm{Fo}}\,(T^{p+1}_{m,n}-T^{p}_{m,n})$$

Rearranging, we have the final form :

$$(1+4\,\mathrm{Fo})\,T^{p+1}_{m,n}-\mathrm{Fo}\left(T^{p+1}_{m+1,n}+2\,T^{p+1}_{m,n-1}+T^{p+1}_{m-1,n}\right)-\frac{2\,q''_0\,\mathrm{Fo}\,\Delta x}{k}=T^{p}_{m,n}$$

For an adiabatic surface, set $q''_0=0$

■ *Convection*

Now consider the same type of node with heat convection at the free surface. All terms remain the same, with the exception of the heat flux coming from node $(m, n+1)$ where:

(1) $q_{(m,n+1)\to(m,n)}=h\,A\,(T_\infty-T^{p+1}_{m,n}),\ A=\Delta x\cdot 1$

Summing and equating appropriate terms

$$h\,(T_\infty-T^{p+1}_{m,n})\,(\Delta x\cdot 1)+k\,\frac{\Delta x}{2}\,\frac{\left(T^{p+1}_{m+1,n}-T^{p+1}_{m,n}\right)}{\Delta x}+k\,\Delta x\,\frac{\left(T^{p+1}_{m,n-1}-T^{p+1}_{m,n}\right)}{\Delta y}+k\,\frac{\Delta x}{2}\,\frac{\left(T^{p+1}_{m-1,n}-T^{p+1}_{m,n}\right)}{\Delta x}=\rho\,C\,\frac{\Delta x^2}{2}\,\frac{T^{p+1}_{m,n}-T^{p}_{m,n}}{\Delta t}$$

Divide by k, multiply by 2, cancel like terms (Δx and Δy), and introduce $\alpha=\frac{k}{\rho C}$:

$$\frac{2\,h\,(T_\infty-T^{p+1}_{m,n})\,\Delta x}{k}+\left(T^{p+1}_{m+1,n}-T^{p+1}_{m,n}\right)+2\left(T^{p+1}_{m,n-1}-T^{p+1}_{m,n}\right)+\left(T^{p+1}_{m-1,n}-T^{p+1}_{m,n}\right)=\frac{1}{\alpha}\,\frac{\Delta x^2}{\Delta t}\,(T^{p+1}_{m,n}-T^{p}_{m,n})$$

Recognize that $\mathrm{Fo}=\frac{\alpha\,\Delta t}{\Delta x^2}$ and $\mathrm{Bi}=\frac{h\,\Delta x}{k}$:

$$2\,\mathrm{Bi}\,(T_\infty-T^{p+1}_{m,n})+T^{p+1}_{m+1,n}+2\,T^{p+1}_{m,n-1}+T^{p+1}_{m-1,n}-4\,T^{p+1}_{m,n}=\frac{1}{\mathrm{Fo}}\,(T^{p+1}_{m,n}-T^{p}_{m,n})$$

$$2\,\mathrm{Bi}\,T_\infty+T^{p+1}_{m+1,n}+2\,T^{p+1}_{m,n-1}+T^{p+1}_{m-1,n}-2\,T^{p+1}_{m,n}(\mathrm{Bi}+2)=\frac{1}{\mathrm{Fo}}\,(T^{p+1}_{m,n}-T^{p}_{m,n})$$

Rearranging, we have the final form :

$$(1+4\,\mathrm{Fo}+2\,\mathrm{Bi}\cdot\mathrm{Fo})\,T^{p+1}_{m,n}-\mathrm{Fo}\left(T^{p+1}_{m+1,n}+2\,T^{p+1}_{m,n-1}+T^{p+1}_{m-1,n}\right)-2\,\mathrm{Bi}\cdot\mathrm{Fo}\,T_\infty=T^{p}_{m,n}$$

For an adiabatic surface, set Bi or $h=0$

■ Inside Corner with Constant Heat Flux or Convection

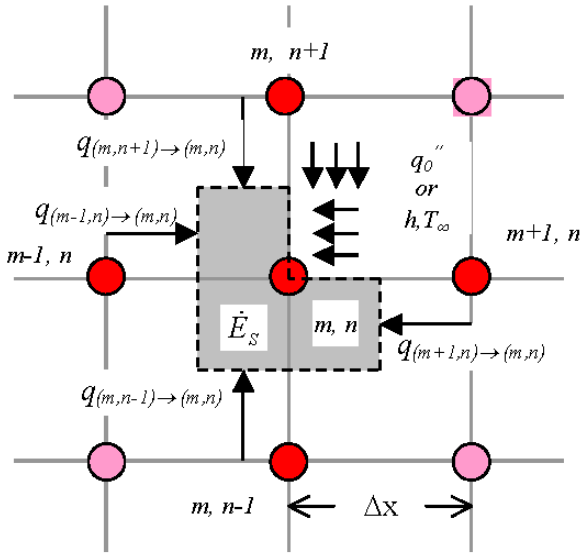

■ *Constant Heat Flux*

We begin with the inside corner having a constant heat flux on two surfaces.

$\dot{E}_{in} = \dot{E}_{st}$, where

$\dot{E}_{st} = \rho\, C\, V\, \frac{T^{p+1}_{m,n} - T^{p}_{m,n}}{\Delta t}$, $V = \frac{3}{4}\,\Delta x \cdot \Delta x \cdot 1 = \frac{3}{4}\,\Delta x^2 \cdot 1\ (m^3)$

and,

$\dot{E}_{in} = \sum_{i=1}^{4} q''_{(i \to m,n)} \cdot A + q''_0\, A$

The heat flux terms are as follows:

(1) $q_{(m,n+1)\to(m,n)} = k\,A\,\frac{(T_{m,n+1} - T_{m,n})}{\Delta y}$, $A = \frac{\Delta x}{2} \cdot 1$

(2) $q_{(m+1,n)\to(m,n)} = k\,A\,\frac{(T_{m+1,n} - T_{m,n})}{\Delta x}$, $A = \frac{\Delta y}{2} \cdot 1$

(3) $q_{(m,n-1)\to(m,n)} = k\,A\,\frac{(T_{m,n-1} - T_{m,n})}{\Delta y}$, $A = \Delta x \cdot 1$

(4) $q_{(m-1,n)\to(m,n)} = k\,A\,\frac{(T_{m-1,n} - T_{m,n})}{\Delta x}$, $A = \Delta y \cdot 1$

(5) $q_0 = q''_{0,x}\,A_x + q''_{0,y}\,A_y$, $A_x = \frac{\Delta y}{2} \cdot 1$, $A_y = \frac{\Delta x}{2} \cdot 1$

Since $q''_{0,x} = q''_{0,y}$, $q_0 = q''_0\,\Delta x \cdot 1$

Summing and equating appropriate terms

$$q''_0\,(\Delta x\cdot 1)+k\,\frac{\Delta x}{2}\,\frac{\left(T^{p+1}_{m,n+1}-T^{p+1}_{m,n}\right)}{\Delta y}+k\,\frac{\Delta x}{2}\,\frac{\left(T^{p+1}_{m+1,n}-T^{p+1}_{m,n}\right)}{\Delta y}+k\,\Delta x\,\frac{\left(T^{p+1}_{m,n-1}-T^{p+1}_{m,n}\right)}{\Delta y}+k\,\Delta x\,\frac{\left(T^{p+1}_{m-1,n}-T^{p+1}_{m,n}\right)}{\Delta x}=\rho\,C\,\frac{3\,\Delta x^2}{4}\,\frac{T^{p+1}_{m,n}-T^{p}_{m,n}}{\Delta t}$$

Divide by k, multiply by 2, cancel like terms (Δx and Δy), and introduce $\alpha=\frac{k}{\rho\,C}$:

$$\frac{2\,q''_0\,\Delta x}{k}+\left(T^{p+1}_{m,n+1}-T^{p+1}_{m,n}\right)+\left(T^{p+1}_{m+1,n}-T^{p+1}_{m,n}\right)+2\left(T^{p+1}_{m,n-1}-T^{p+1}_{m,n}\right)+2\left(T^{p+1}_{m-1,n}-T^{p+1}_{m,n}\right)=\frac{1}{\alpha}\,\frac{3\,\Delta x^2}{2\,\Delta t}\,(T^{p+1}_{m,n}-T^{p}_{m,n})$$

Recognize that $\mathrm{Fo}=\frac{\alpha\,\Delta t}{\Delta x^2}$:

$$\frac{2\,q''_0\,\Delta x}{k}+T^{p+1}_{m,n+1}+T^{p+1}_{m+1,n}+2\,T^{p+1}_{m,n-1}+2\,T^{p+1}_{m-1,n}-6\,T^{p+1}_{m,n}=\frac{3}{2\,\mathrm{Fo}}\,(T^{p+1}_{m,n}-T^{p}_{m,n})$$

Rearranging, we have the final form :

$$(1+4\,\mathrm{Fo})\,T^{p+1}_{m,n}-\frac{2}{3}\,\mathrm{Fo}\left(T^{p+1}_{m,n+1}+T^{p+1}_{m+1,n}+2\,T^{p+1}_{m,n-1}+2\,T^{p+1}_{m-1,n}\right)-\frac{4\,q''_0\,\mathrm{Fo}\,\Delta x}{3\,k}=T^{p}_{m,n}$$

■ *Convection*

Now consider the same type of node with heat convection at the free surface. The only term that changes is the $q_{(\infty)\to(m,n)}$ term which becomes:

$q_{(\infty)\to(m,n)}=q_{\infty,x}\cdot A_x+q_{\infty,y}\cdot A_y$, wher $A_x=A_y=\frac{\Delta x}{2}\cdot 1$ for a uniform mesh.

$q_{(\infty)\to(m,n)}=h\,\Delta x\,(T_\infty-T^{p+1}_{m,n})$

Summing and equating appropriate terms

$$h\,(T_\infty-T^{p+1}_{m,n})\,(\Delta x\cdot 1)+k\,\frac{\Delta x}{2}\,\frac{\left(T^{p+1}_{m,n+1}-T^{p+1}_{m,n}\right)}{\Delta y}+k\,\frac{\Delta x}{2}\,\frac{\left(T^{p+1}_{m+1,n}-T^{p+1}_{m,n}\right)}{\Delta y}+k\,\Delta x\,\frac{\left(T^{p+1}_{m,n-1}-T^{p+1}_{m,n}\right)}{\Delta y}+k\,\Delta x\,\frac{\left(T^{p+1}_{m-1,n}-T^{p+1}_{m,n}\right)}{\Delta x}=\rho\,C\,\frac{3\,\Delta x^2}{4}\,\frac{T^{p+1}_{m,n}-T^{p}_{m,n}}{\Delta t}$$

Divide by k, multiply by 2, cancel like terms (Δx and Δy), and introduce $\alpha=\frac{k}{\rho\,C}$:

$$\frac{2\,h\,(T_\infty-T^{p+1}_{m,n})\,\Delta x}{k}+\left(T^{p+1}_{m,n+1}-T^{p+1}_{m,n}\right)+\left(T^{p+1}_{m+1,n}-T^{p+1}_{m,n}\right)+2\left(T^{p+1}_{m,n-1}-T^{p+1}_{m,n}\right)+2\left(T^{p+1}_{m-1,n}-T^{p+1}_{m,n}\right)=\frac{1}{\alpha}\,\frac{3\,\Delta x^2}{2\,\Delta t}\,(T^{p+1}_{m,n}-T^{p}_{m,n})$$

Recognize that $\mathrm{Fo}=\frac{\alpha\,\Delta t}{\Delta x^2}$ and $\mathrm{Bi}=\frac{h\,\Delta x}{k}$:

$$2\,\mathrm{Bi}\,(T_\infty-T^{p+1}_{m,n})+T^{p+1}_{m,n+1}+T^{p+1}_{m+1,n}+2\,T^{p+1}_{m,n-1}+2\,T^{p+1}_{m-1,n}-6\,T^{p+1}_{m,n}=\frac{3}{2\,\mathrm{Fo}}\,(T^{p+1}_{m,n}-T^{p}_{m,n})$$

$$2\,\mathrm{Bi}\,T_\infty+T^{p+1}_{m,n+1}+T^{p+1}_{m+1,n}+2\,T^{p+1}_{m,n-1}+2\,T^{p+1}_{m-1,n}-2\,T^{p+1}_{m,n}(\mathrm{Bi}+3)=\frac{3}{2\,\mathrm{Fo}}\,(T^{p+1}_{m,n}-T^{p}_{m,n})$$

Rearranging, we have the final form :

$$(1+4\,\mathrm{Fo}+\tfrac{4}{3}\,\mathrm{Bi}\cdot\mathrm{Fo})\,T^{p+1}_{m,n}-\frac{2}{3}\,\mathrm{Fo}\left(T^{p+1}_{m,n+1}+T^{p+1}_{m+1,n}+2\,T^{p+1}_{m,n-1}+2\,T^{p+1}_{m-1,n}\right)-\frac{4}{3}\,\mathrm{Bi}\cdot\mathrm{Fo}\,T_\infty=T^{p}_{m,n}$$

■ Outside Corner with Constant Heat Flux or Convection

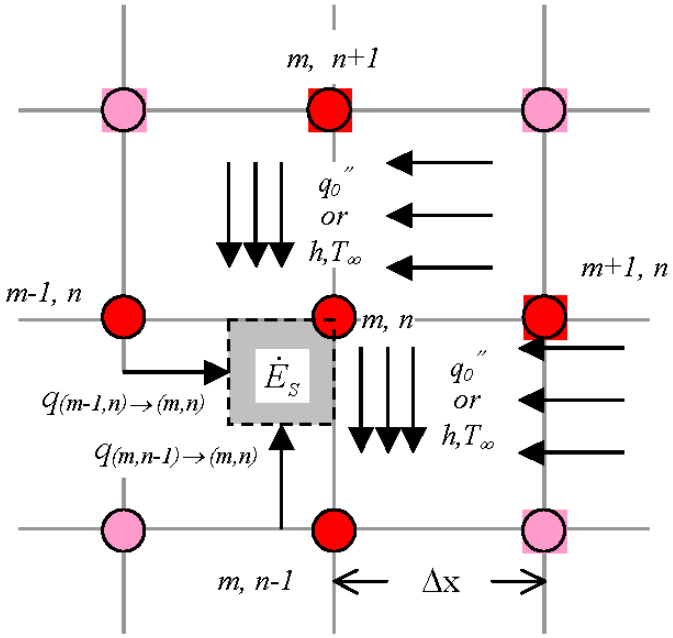

■ *Constant Heat Flux*

We begin with the outside corner having a constant heat flux on two surfaces.

$\dot{E}_{in} = \dot{E}_{st}$, where

$\dot{E}_{st} = \rho\, C\, V\, \frac{T_{m,n}^{p+1} - T_{m,n}^{p}}{\Delta t}$, $V = \frac{1}{4}\,\Delta x \cdot \Delta x \cdot 1 = \frac{1}{4}\,\Delta x^2 \cdot 1\ (m^3)$

and,

$\dot{E}_{in} = \sum_{i=1}^{4} q''_{(i\to m,\,n)} \cdot A + q_0'' A$

The heat flux terms are as follows:

(1) $q_{(m,n+1)\to(m,n)} = 0$

(2) $q_{(m+1,n)\to(m,n)} = 0$

(3) $q_{(m,n-1)\to(m,n)} = k A \frac{(T_{m,n-1} - T_{m,n})}{\Delta y}$, $A = \frac{\Delta x}{2} \cdot 1$

(4) $q_{(m-1,n)\to(m,n)} = k A \frac{(T_{m-1,n} - T_{m,n})}{\Delta x}$, $A = \frac{\Delta y}{2} \cdot 1$

(5) $q_0 = q''_{0,x} A_x + q''_{0,y} A_y$, $A_x = \frac{\Delta y}{2} \cdot 1$, $A_y = \frac{\Delta x}{2} \cdot 1$

Since $q''_{0,x} = q''_{0,y}$, $q_0 = q_0'' \,\Delta x \cdot 1$

Summing and equating appropriate terms

$q''_0\,(\Delta x \cdot 1) + k\,\frac{\Delta x}{2}\,\frac{\left(T^{p+1}_{m,n-1} - T^{p+1}_{m,n}\right)}{\Delta y} + k\,\frac{\Delta x}{2}\,\frac{\left(T^{p+1}_{m-1,n} - T^{p+1}_{m,n}\right)}{\Delta x} = \rho\, C\,\frac{1\,\Delta x^2}{4}\,\frac{T^{p+1}_{m,n} - T^{p}_{m,n}}{\Delta t}$

Divide by k, multiply by 2, cancel like terms (Δx and Δy), and introduce $\alpha = \frac{k}{\rho\, C}$:

$$\frac{2\,q''_0\,\Delta x}{k} + \left(T^{p+1}_{m,n-1} - T^{p+1}_{m,n}\right) + \left(T^{p+1}_{m-1,n} - T^{p+1}_{m,n}\right) = \frac{1}{\alpha}\,\frac{1\,\Delta x^2}{2\,\Delta t}\,\left(T^{p+1}_{m,n} - T^{p}_{m,n}\right)$$

Recognize that $\mathrm{Fo} = \frac{\alpha\,\Delta t}{\Delta x^2}$:

$$\frac{2\,q''_0\,\Delta x}{k} + T^{p+1}_{m,n-1} + T^{p+1}_{m-1,n} - 2\,T^{p+1}_{m,n} = \frac{1}{2\,\mathrm{Fo}}\,\left(T^{p+1}_{m,n} - T^{p}_{m,n}\right)$$

Rearranging, we have the final form :

$$(1 + 4\,\mathrm{Fo})\,T^{p+1}_{m,n} - 2\,\mathrm{Fo}\left(T^{p+1}_{m,n-1} + T^{p+1}_{m-1,n}\right) - \frac{4\,q''_0\,\mathrm{Fo}\,\Delta x}{k} = T^{p}_{m,n}$$

■ *Convection*

Now consider the same type of node with heat convection at the free surface. The only term that changes is the $q_{(\infty)\to(m,n)}$ term which becomes:

$q_{(\infty)\to(m,n)} = q_{\infty,x}\cdot A_x + q_{\infty,y}\cdot A_y$, wher $A_x = A_y = \frac{\Delta x}{2}\cdot 1$ for a uniform mesh.

$q_{(\infty)\to(m,n)} = h\,\Delta x\,(T_\infty - T^{p+1}_{m,n})$

Summing and equating appropriate terms

$h\,\left(T_\infty - T^{p+1}_{m,n}\right)(\Delta x\cdot 1) + k\,\frac{\Delta x}{2}\,\frac{\left(T^{p+1}_{m,n-1} - T^{p+1}_{m,n}\right)}{\Delta y} + k\,\frac{\Delta x}{2}\,\frac{\left(T^{p+1}_{m-1,n} - T^{p+1}_{m,n}\right)}{\Delta x} = \rho\, C\,\frac{1\,\Delta x^2}{4}\,\frac{T^{p+1}_{m,n} - T^{p}_{m,n}}{\Delta t}$

Divide by k, multiply by 2, cancel like terms (Δx and Δy), and introduce $\alpha = \frac{k}{\rho\, C}$:

$$\frac{2\,h\,\left(T_\infty - T^{p+1}_{m,n}\right)\Delta x}{k} + \left(T^{p+1}_{m,n-1} - T^{p+1}_{m,n}\right) + \left(T^{p+1}_{m-1,n} - T^{p+1}_{m,n}\right) = \frac{1}{\alpha}\,\frac{1\,\Delta x^2}{2\,\Delta t}\,\left(T^{p+1}_{m,n} - T^{p}_{m,n}\right)$$

Recognize that $\mathrm{Fo} = \frac{\alpha\,\Delta t}{\Delta x^2}$ and $\mathrm{Bi} = \frac{h\,\Delta x}{k}$:

$$2\,\mathrm{Bi}\,(T_\infty - T^{p+1}_{m,n}) + T^{p+1}_{m,n-1} + T^{p+1}_{m-1,n} - 2\,T^{p+1}_{m,n} = \frac{1}{2\,\mathrm{Fo}}\,\left(T^{p+1}_{m,n} - T^{p}_{m,n}\right)$$

$$2\,\mathrm{Bi}\,T_\infty + T^{p+1}_{m,n-1} + T^{p+1}_{m-1,n} - 2\,T^{p+1}_{m,n}(\mathrm{Bi} + 1) = \frac{3}{2\,\mathrm{Fo}}\,\left(T^{p+1}_{m,n} - T^{p}_{m,n}\right)$$

Rearranging, we have the final form :

$$(1 + 4\,\mathrm{Fo} + 4\,\mathrm{Bi}\cdot\mathrm{Fo})\,T^{p+1}_{m,n} - 2\,\mathrm{Fo}\left(T^{p+1}_{m,n-1} + T^{p+1}_{m-1,n}\right) - 4\,\mathrm{Bi}\cdot\mathrm{Fo}\,T_\infty = T^{p}_{m,n}$$

■ Left Corner with 1 Adiabatic and 1 Convection Surface

This particular node is a symmetry node that has a surface exposed to convective heat transfer. As before, we begin our energy balance with the energy input and storage terms:

$\dot{E}_{\mathrm{in}} = \dot{E}_{\mathrm{st}}$, where

$\dot{E}_{\mathrm{st}} = \rho\, C\, V\,\frac{T^{p+1}_{m,n} - T^{p}_{m,n}}{\Delta t}$, $V = \frac{1}{4}\,\Delta x\cdot\Delta x\cdot 1 = \frac{1}{4}\,\Delta x^2\cdot 1\,(m^3)$

and,

$\dot{E}_{\mathrm{in}} = \sum_{i=1}^{4} q''_{(i\to m,n)}\cdot A + q''_\infty\, A$

The heat flux terms are as follows:

(1) $q_{(m,n+1)\to(m,n)} = 0$

(2) $q_{(m+1,n)\to(m,n)} = k A \frac{(T_{m+1,n}-T_{m,n})}{\Delta y}, \; A = \frac{\Delta x}{2}\cdot 1$

(3) $q_{(m,n-1)\to(m,n)} = k A \frac{(T_{m,n-1}-T_{m,n})}{\Delta y}, \; A = \frac{\Delta x}{2}\cdot 1$

(4) $q_{(m-1,n)\to(m,n)} = 0$ (adiabatic)

(5) $q_{(\infty)\to(m,n)} = q_{\infty,y}\cdot A_y$, where $A_y = \frac{\Delta x}{2}\cdot 1$

$q_{(\infty)\to(m,n)} = h \frac{\Delta x}{2}(T_\infty - T^{p+1}_{m,n})$

Summing and equating appropriate terms

$h\,(T_\infty - T^{p+1}_{m,n})(\frac{\Delta x}{2}\cdot 1) + k\frac{\Delta x}{2}\frac{(T^{p+1}_{m+1,n}-T^{p+1}_{m,n})}{\Delta x} + k\frac{\Delta x}{2}\frac{(T^{p+1}_{m,n-1}-T^{p+1}_{m,n})}{\Delta y} += \rho C \frac{\Delta x^2}{4}\frac{T^{p+1}_{m,n}-T^{p}_{m,n}}{\Delta t}$

Divide by k, multiply by 2, cancel like terms (Δx and Δy), and introduce $\alpha = \frac{k}{\rho C}$:

$$\frac{h\,(T_\infty - T^{p}_{m,n})\Delta x}{k} + \left(T^{p+1}_{m,n-1} - T^{p+1}_{m,n}\right) + \left(T^{p+1}_{m+1,n} - T^{p+1}_{m,n}\right) = \frac{1}{\alpha}\frac{\Delta x^2}{2\Delta t}\,(T^{p+1}_{m,n} - T^{p}_{m,n})$$

Recognize that $\mathrm{Fo} = \frac{\alpha\Delta t}{\Delta x^2}$ and $\mathrm{Bi} = \frac{h\Delta x}{k}$:

$$\mathrm{Bi}\,(T_\infty - T^{p+1}_{m,n}) + T^{p+1}_{m,n-1} + T^{p+1}_{m+1,n} - 2\,T^{p+1}_{m,n} = \frac{1}{2\,\mathrm{Fo}}\,(T^{p+1}_{m,n} - T^{p}_{m,n})$$

$$\mathrm{Bi}\,T_\infty + T^{p+1}_{m,n-1} + T^{p+1}_{m+1,n} - T^{p+1}_{m,n}(\mathrm{Bi}+2) = \frac{1}{2\,\mathrm{Fo}}\,(T^{p+1}_{m,n} - T^{p}_{m,n})$$

Multiply by 2 Fo :

$$2\,\mathrm{Bi}\cdot\mathrm{Fo}\,T_\infty + 2\,\mathrm{Fo}\left(T^{p+1}_{m,n-1} + T^{p+1}_{m+1,n}\right) - T^{p+1}_{m,n}(2\,\mathrm{Bi}\cdot\mathrm{Fo} + 4\,\mathrm{Fo}) = T^{p+1}_{m,n} - T^{p}_{m,n}$$

Collecting p and $p+1$ terms, we have the final form :

$$(1 + 4\,\mathrm{Fo} + 2\,\mathrm{Bi}\cdot\mathrm{Fo})\,T^{p+1}_{m,n} - 2\,\mathrm{Bi}\cdot\mathrm{Fo}\,T_\infty - 2\,\mathrm{Fo}\left(T^{p+1}_{m,n-1} + T^{p+1}_{m-1,n}\right) = T^{p}_{m,n}$$

■ Temperature Dependent Properties

Adding the temperature dependent properties, namely thermal conductivity and specific heat, is a fairly easy task provided we make some assumptions concerning how we calculate the thermal conductivity for the next time step given that the temperature is unknown at the next time step. Ozisik proposes two methods to accomplish this task. In the first method, the thermal property is calculated at the temperature T^p and used in the calculation of the temperature T^{p+1}, in other words the properties are lagging by one time step. An extrapolation method can be used to estimate the thermal property using the thermal property at time step p, the slope of the thermal property vs. Temperature data at the time step p, and the temperature change between time steps p and p-1 in the following manner using thermal conductivity as an example:

$k^{p+1} \cong k^p + (\frac{\partial k}{\partial T})^p (T^p - T^{p-1})$

The extrapolation method generally is more accurate.

What we are concerned with now is incorporating temperature dependence into our finite difference equations. In order to accomplish this task, a method of determining the thermal property, specifically thermal conductivity, must be determined as well as a labeling convention to keep the equations organized. First we must assume that the thermal conductivity term in Fourier's law is taken at the average temperture of the two nodes, that is:

$q = A\,k(T)\,\frac{T_i - T}{\Delta x} \propto k(\frac{T_i - T}{2})\,(T_i - T)$, where

i is the local node number. This is a reasonable approximation if the thermal conductivity data is linear, which in our case, is true. We could also take the average of the thermal conductivities at each node temperature.

An example of the labeling convention to be used from here on is as follows:

$k_1^p = \frac{k_{m,n+1}^p + k_{m,n}^p}{2} = \frac{k(T_{m,n+1}^p) - k(T_{m,n}^p)}{2}$

$k_2^p = \frac{k_{m+1,n}^p + k_{m,n}^p}{2} = \frac{k(T_{m+1,n}^p) - k(T_{m,n}^p)}{2}$ ...

$k_1^{p+1} = \frac{k_{m,n+1}^{p+1} + k_{m,n}^{p+1}}{2} = \frac{k(T_{m,n+1}^{p+1}) - k(T_{m,n}^{p+1})}{2}$ $k_2^{p+1} = \frac{k_{m+1,n}^{p+1} + k_{m,n}^{p+1}}{2} = \frac{k(T_{m+1,n}^{p+1}) - k(T_{m,n}^{p+1})}{2}$ ...etc

The specific heat is also temperature dependent and should be calculated for the central node.

Another labeling convention concerns the Fourier number. It depends on the thermal conductivty between the surrounding local node i and the central node as well as the specific heat of the central node such that:

$\text{Fo}_i = \frac{k_i}{\rho C} \frac{\Delta t}{\Delta x^2}$.

In general, each of the equations may be modified from the final version of the existing temperature independent finite difference equations. Thus, there is no need to re-derive each equation.

■ Interior Node

The existing form of the interior node backwards difference equation is:

$$\left(T_{m,n+1}^{p+1} - T_{m,n}^{p+1}\right) + \left(T_{m+1,n}^{p+1} - T_{m,n}^{p+1}\right) + \left(T_{m,n-1}^{p+1} - T_{m,n}^{p+1}\right) + \left(T_{m-1,n}^{p+1} - T_{m,n}^{p+1}\right) + \frac{\dot{q}\,\Delta x^2}{k} = \frac{1}{\alpha}\frac{\Delta x^2}{\Delta t}\left(T_{m,n}^{p+1} - T_{m,n}^{p}\right)$$

Modifying for temperature dependent properties (multiply by k_i):

$$k_1^{p+1}\left(T_{m,n+1}^{p+1} - T_{m,n}^{p+1}\right) + k_2^{p+1}\left(T_{m+1,n}^{p+1} - T_{m,n}^{p+1}\right) + k_3^{p+1}\left(T_{m,n-1}^{p+1} - T_{m,n}^{p+1}\right) + k_4^{p+1}\left(T_{m-1,n}^{p+1} - T_{m,n}^{p+1}\right) + \dot{q}\,\Delta x^2 = \rho\, C\, \frac{\Delta x^2}{\Delta t}\left(T_{m,n}^{p+1} - T_{m,n}^{p}\right)$$

Divide by $\rho\, C\, \frac{\Delta x^2}{\Delta t}$ and assume the Fo_i convention:

$$-\text{Fo}_1^{p+1}\left(T_{m,n+1}^{p+1} - T_{m,n}^{p+1}\right) - \text{Fo}_2^{p+1}\left(T_{m+1,n}^{p+1} - T_{m,n}^{p+1}\right) - \text{Fo}_3^{p+1}\left(T_{m,n-1}^{p+1} - T_{m,n}^{p+1}\right) - \text{Fo}_4^{p+1}\left(T_{m-1,n}^{p+1} - T_{m,n}^{p+1}\right) - \frac{\dot{q}\,\Delta t}{\rho C} + T_{m,n}^{p+1} = T_{m,n}^{p}$$

$$-\left(\text{Fo}_1^{p+1}\, T_{m,n+1}^{p+1} + \text{Fo}_2^{p+1}\, T_{m+1,n}^{p+1} + \text{Fo}_3^{p+1}\, T_{m,n-1}^{p+1} + \text{Fo}_4^{p+1}\, T_{m-1,n}^{p+1}\right) + \left(\text{Fo}_1^{p+1} + \text{Fo}_2^{p+1} + \text{Fo}_3^{p+1} + \text{Fo}_4^{p+1} + 1\right) T_{m,n}^{p+1} - \frac{\dot{q}\,\Delta t}{\rho C} = T_{m,n}^{p}$$

If there is no internal heat generation, set $\dot{q} = 0$.

■ Surface Node with Convection or Constant Heat Flux

■ *Constant Heat Flux*

The existing form of the surface node backwards difference equation is:

$$2\, q_0''\,(\Delta x \cdot 1) + k\left(T_{m+1,n}^{p+1} - T_{m,n}^{p+1}\right) + 2\,k\,\left(T_{m,n-1}^{p+1} - T_{m,n}^{p+1}\right) + k\left(T_{m-1,n}^{p+1} - T_{m,n}^{p+1}\right) = \rho\, C\, \Delta x^2\, \frac{T_{m,n}^{p+1} - T_{m,n}^{p}}{\Delta t}$$

Modifying for temperature dependent properties (add k_i):

$$2\,q_0''\,\Delta x + k_2^{p+1}\left(T_{m+1,n}^{p+1} - T_{m,n}^{p+1}\right) + 2\,k_3^{p+1}\left(T_{m,n-1}^{p+1} - T_{m,n}^{p+1}\right) + k_4^{p+1}\left(T_{m-1,n}^{p+1} - T_{m,n}^{p+1}\right) = \rho\,C\,\frac{\Delta x^2}{\Delta t}\left(T_{m,n}^{p+1} - T_{m,n}^{p}\right)$$

Divide by $\rho\,C\,\frac{\Delta x^2}{\Delta t}$ and assume the Fo_i convention:

$$-\frac{2q_0''\,\Delta t}{\rho\,C\,\Delta x} - \mathrm{Fo}_2^{p+1}\left(T_{m+1,n}^{p+1} - T_{m,n}^{p+1}\right) - 2\,\mathrm{Fo}_3^{p+1}\left(T_{m,n-1}^{p+1} - T_{m,n}^{p+1}\right) - \mathrm{Fo}_4^{p+1}\left(T_{m-1,n}^{p+1} - T_{m,n}^{p+1}\right) + T_{m,n}^{p+1} = T_{m,n}^{p}$$

$$-\left(\mathrm{Fo}_2^{p+1}\,T_{m+1,n}^{p+1} + 2\,\mathrm{Fo}_3^{p+1}\,T_{m,n-1}^{p+1} + \mathrm{Fo}_4^{p+1}\,T_{m-1,n}^{p+1}\right) + \left(\mathrm{Fo}_2^{p+1} + 2\,\mathrm{Fo}_3^{p+1} + \mathrm{Fo}_4^{p+1} + 1\right)T_{m,n}^{p} - \frac{2q_0''\,\Delta t}{\rho\,C\,\Delta x} = T_{m,n}^{p+1}$$

For an adiabatic surface, set $q_0'' = 0$

■ *Convection*

The existing form of the surface node backwards difference equation is:

$$2\,h\,\left(T_\infty - T_{m,n}^{p+1}\right)(\Delta x \cdot 1) + k\left(T_{m+1,n}^{p+1} - T_{m,n}^{p+1}\right) + 2\,k\left(T_{m,n-1}^{p+1} - T_{m,n}^{p+1}\right) + k\left(T_{m-1,n}^{p+1} - T_{m,n}^{p+1}\right) = \rho\,C\,\frac{\Delta x^2}{\Delta t}\left(T_{m,n}^{p+1} - T_{m,n}^{p}\right)$$

Modifying for temperature dependent properties (add k_i):

$$2\,h\,\Delta x\,(T_\infty - T_{m,n}^{p+1}) + k_2^{p+1}\left(T_{m+1,n}^{p+1} - T_{m,n}^{p+1}\right) + 2\,k_3^{p+1}\left(T_{m,n-1}^{p+1} - T_{m,n}^{p+1}\right) + k_4^{p+1}\left(T_{m-1,n}^{p+1} - T_{m,n}^{p+1}\right) = \rho\,C\,\frac{\Delta x^2}{\Delta t}\left(T_{m,n}^{p+1} - T_{m,n}^{p}\right)$$

Divide by $\rho\,C\,\frac{\Delta x^2}{\Delta t}$ and assume the Fo_i convention:

$$-\frac{2h\,\Delta t}{\rho\,C\,\Delta x}\left(T_\infty - T_{m,n}^{p+1}\right) - \mathrm{Fo}_2^{p+1}\left(T_{m+1,n}^{p+1} - T_{m,n}^{+1}\right) - 2\,\mathrm{Fo}_3^{p+1}\left(T_{m,n-1}^{p+1} - T_{m,n}^{p+1}\right) - \mathrm{Fo}_4^{p+1}\left(T_{m-1,n}^{p+1} - T_{m,n}^{p+1}\right) + T_{m,n}^{p+1} = T_{m,n}^{p}$$

$$-\left(\mathrm{Fo}_2^{p+1}\,T_{m+1,n}^{p+1} + 2\,\mathrm{Fo}_3^{p+1}\,T_{m,n-1}^{p+1} + \mathrm{Fo}_4^{p+1}\,T_{m-1,n}^{p+1} + \frac{2h\,\Delta t}{\rho\,C\,\Delta x}\,T_\infty\right) + \left(\mathrm{Fo}_2^{p+1} + 2\,\mathrm{Fo}_3^{p+1} + \mathrm{Fo}_4^{p+1} + \frac{2h\,\Delta t}{\rho\,C\,\Delta x} + 1\right)T_{m,n}^{p+1} = T_{m,n}^{p}$$

For an adiabatic surface, set $h = 0$

■ Inside Corner with Constant Heat Flux or Convection

■ *Constant Heat Flux*

The existing form of the surface node backwards difference equation is:

$$2\,q_0''\,(\Delta x \cdot 1) + k\left(T_{m,n+1}^{p+1} - T_{m,n}^{p+1}\right) + k\left(T_{m+1,n}^{p+1} - T_{m,n}^{p+1}\right) + 2\,k\left(T_{m,n-1}^{p+1} - T_{m,n}^{p+1}\right) + 2\,k\left(T_{m-1,n}^{p+1} - T_{m,n}^{p+1}\right) = \rho\,C\,\frac{\frac{3\Delta x^2}{2}}{\Delta t}\,\frac{T_{m,n}^{p+1} - T_{m,n}^{p}}{}$$

Modifying for temperature dependent properties (add k_i):

$$2\,q_0''\,\Delta x + k_1^{p+1}\left(T_{m,n+1}^{p+1} - T_{m,n}^{p+1}\right) + k_2^{p+1}\left(T_{m+1,n}^{p+1} - T_{m,n}^{p+1}\right) + 2\,k_3^{p+1}\left(T_{m,n-1}^{p+1} - T_{m,n}^{p+1}\right) + 2\,k_4^{p+1}\left(T_{m-1,n}^{p+1} - T_{m,n}^{p+1}\right) = \rho\,C\,\frac{3\Delta x^2}{2\Delta t}\left(T_{m,n}^{p+1} - T_{m,n}^{p}\right)$$

Divide by $\rho\, C\, \frac{3\,\Delta x^2}{2\,\Delta t}$ and assume the Fo_i convention:

$$-\frac{4\,q_0''\,\Delta t}{3\,\rho\, C\,\Delta x} - \frac{2}{3}\,\mathrm{Fo}_1^{p+1}\left(T_{m,n+1}^{p+1} - T_{m,n}^{p+1}\right) - \frac{2}{3}\,\mathrm{Fo}_2^{p+1}\left(T_{m+1,n}^{p+1} - T_{m,n}^{p+1}\right) - \frac{4}{3}\,\mathrm{Fo}_3^{p+1}\left(T_{m,n-1}^{p+1} - T_{m,n}^{p+1}\right) - \frac{4}{3}\,\mathrm{Fo}_4^{p+1}\left(T_{m-1,n}^{p+1} - T_{m,n}^{p+1}\right) + T_{m,n}^{p+1} = T_{m,n}^{p}$$

$$-\frac{2}{3}\left(\mathrm{Fo}_1^{p+1}\,T_{m,n+1}^{p} + \mathrm{Fo}_2^{p+1}\,T_{m+1,n}^{p} + 2\,\mathrm{Fo}_3^{p+1}\,T_{m,n-1}^{p} + 2\,\mathrm{Fo}_4^{p+1}\,T_{m-1,n}^{p} + \frac{2\,q_0''\,\Delta t}{\rho\, C\,\Delta x}\right) + \frac{2}{3}\left(\mathrm{Fo}_1^{p+1} + \mathrm{Fo}_2^{p+1} + 2\,\mathrm{Fo}_3^{p+1} + 2\,\mathrm{Fo}_4^{p+1} + \frac{3}{2}\right)T_{m,n}^{p+1} = T_{m,n}^{p}$$

For an adiabatic surface, set $q_0'' = 0$

■ *Convection*

The existing form of the surface node backwards difference equation is:

$$2\,h\,\left(T_\infty - T_{m,n}^{p+1}\right)(\Delta x) + k\left(T_{m,n+1}^{p+1} - T_{m,n}^{p+1}\right) + k\left(T_{m+1,n}^{p+1} - T_{m,n}^{p+1}\right) + 2\,k\left(T_{m,n-1}^{p+1} - T_{m,n}^{p+1}\right) + 2\,k\left(T_{m-1,n}^{p+1} - T_{m,n}^{p+1}\right) = \rho\, C\,\frac{3\,\Delta x^2}{2}\,\frac{T_{m,n}^{p+1} - T_{m,n}^{p}}{\Delta t}$$

Modifying for temperature dependent properties (add k_i):

$$2\,h\,\Delta x\left(T_\infty - T_{m,n}^{p+1}\right) + k_1^{p+1}\left(T_{m,n+1}^{p+1} - T_{m,n}^{p+1}\right) + k_2^{p+1}\left(T_{m+1,n}^{p+1} - T_{m,n}^{p+1}\right) + 2\,k_3^{p+1}\left(T_{m,n-1}^{p+1} - T_{m,n}^{p+1}\right) + 2\,k_4^{p+1}\left(T_{m-1,n}^{p+1} - T_{m,n}^{p+1}\right) = \rho\, C\,\frac{3\,\Delta x^2}{2\,\Delta t}\left(T_{m,n}^{p+1} - T_{m,n}^{p}\right)$$

Divide by $\rho\, C\, \frac{3\,\Delta x^2}{2\,\Delta t}$ and assume the Fo_i convention:

$$-\frac{4\,h\,\Delta t}{3\,\rho\, C\,\Delta x}\left(T_\infty - T_{m,n}^{p+1}\right) - \frac{2}{3}\,\mathrm{Fo}_1^{p+1}\left(T_{m,n+1}^{p+1} - T_{m,n}^{p+1}\right) - \frac{2}{3}\,\mathrm{Fo}_2^{p+1}\left(T_{m+1,n}^{p+1} - T_{m,n}^{p+1}\right) - \frac{4}{3}\,\mathrm{Fo}_3^{p+1}\left(T_{m,n-1}^{p+1} - T_{m,n}^{p+1}\right) - \frac{4}{3}\,\mathrm{Fo}_4^{p+1}\left(T_{m-1,n}^{p+1} - T_{m,n}^{p+1}\right) + T_{m,n}^{p+1} = T_{m,n}^{p}$$

$$-\frac{2}{3}\left(\mathrm{Fo}_1^{p+1}\,T_{m,n+1}^{p+1} + \mathrm{Fo}_2^{p+1}\,T_{m+1,n}^{p+1} + 2\,\mathrm{Fo}_3^{p+1}\,T_{m,n-1}^{p+1} + 2\,\mathrm{Fo}_4^{p+1}\,T_{m-1,n}^{p+1} + \frac{2\,h\,\Delta t}{\rho\, C\,\Delta x}\,T_\infty\right) + \frac{2}{3}\left(\mathrm{Fo}_1^{p+1} + \mathrm{Fo}_2^{p+1} + 2\,\mathrm{Fo}_3^{p+1} + 2\,\mathrm{Fo}_4^{p+1} + \frac{2\,h\,\Delta t}{\rho\, C\,\Delta x} + \frac{3}{2}\right)T_{m,n}^{p+1} = T_{m,n}^{p}$$

For an adiabatic surface, set $h = 0$

■ Outside Corner with Constant Heat Flux or Convection

■ *Constant Heat Flux*

The existing form of the surface node backswards difference equation is:

$$2\,q_0''\,(\Delta x\cdot 1) + k\left(T_{m,n-1}^{p+1} - T_{m,n}^{p+1}\right) + k\left(T_{m-1,n}^{p+1} - T_{m,n}^{p+1}\right) = \rho\, C\,\frac{\Delta x^2}{2}\,\frac{T_{m,n}^{p+1} - T_{m,n}^{p}}{\Delta t}$$

Modifying for temperature dependent properties (add k_i):

$$2\,q_0''\,(\Delta x) + k_3^{p+1}\left(T_{m,n-1}^{p+1} - T_{m,n}^{p+1}\right) + k_4^{p+1}\left(T_{m-1,n}^{p+1} - T_{m,n}^{p+1}\right) = \rho\, C\,\frac{\Delta x^2}{2\,\Delta t}\left(T_{m,n}^{p+1} - T_{m,n}^{p}\right)$$

Divide by $\rho\, C\, \frac{\Delta x^2}{2\,\Delta t}$ and assume the Fo_i convention:

$$-\frac{4 q_0'' \Delta t}{\rho\, C\, \Delta x} - 2\,\mathrm{Fo}_3^{p+1}\left(T_{m,n-1}^{p+1} - T_{m,n}^{p+1}\right) - 2\,\mathrm{Fo}_4^{p+1}\left(T_{m-1,n}^{p+1} - T_{m,n}^{p+1}\right) + T_{m,n}^{p+1} = T_{m,n}^{p}$$

$$-2\left(\mathrm{Fo}_3^{p+1}\, T_{m,n-1}^{p+1} + \mathrm{Fo}_4^{p+1}\, T_{m-1,n}^{p+1} + \frac{2 q_0'' \Delta t}{\rho\, C\, \Delta x}\right) + 2\left(\mathrm{Fo}_3^{p+1} + \mathrm{Fo}_4^{p+1} + \frac{1}{2}\right) T_{m,n}^{p+1} = T_{m,n}^{p}$$

For an adiabatic surface, set $q_0'' = 0$

■ *Convection*

The existing form of the surface node backwards difference equation is:

$$2\,h\,(T_\infty - T_{m,n}^{p+1})\,\Delta x + k\left(T_{m,n-1}^{p+1} - T_{m,n}^{p+1}\right) + k\left(T_{m-1,n}^{p+1} - T_{m,n}^{p+1}\right) = \rho\, C\, \frac{\Delta x^2}{2\,\Delta t}\,(T_{m,n}^{p+1} - T_{m,n}^{p})$$

Modifying for temperature dependent properties (add k_i):

$$2\,h\,(T_\infty - T_{m,n}^{p+1})\,\Delta x + k_3^{p+1}\left(T_{m,n-1}^{p+1} - T_{m,n}^{p+1}\right) + k_4^{p+1}\left(T_{m-1,n}^{p+1} - T_{m,n}^{p+1}\right) = \rho\, C\, \frac{\Delta x^2}{2\,\Delta t}\,(T_{m,n}^{p+1} - T_{m,n}^{p})$$

Divide by $\rho\, C\, \frac{\Delta x^2}{2\,\Delta t}$ and assume the Fo_i convention:

$$-\frac{4\,h\,\Delta t}{\rho\, C\, \Delta x}\,(T_\infty - T_{m,n}^{p+1}) - 2\,\mathrm{Fo}_3^{p+1}\left(T_{m,n-1}^{p+1} - T_{m,n}^{p+1}\right) - 2\,\mathrm{Fo}_4^{p+1}\left(T_{m-1,n}^{p+1} - T_{m,n}^{p+1}\right) + T_{m,n}^{p+1} = T_{m,n}^{p}$$

$$-2\left(\mathrm{Fo}_3^{p+1}\, T_{m,n-1}^{p+1} + \mathrm{Fo}_4^{p+1}\, T_{m-1,n}^{p+1} + \frac{2\,h\,\Delta t}{\rho\, C\, \Delta x}\, T_\infty\right) + 2\left(\mathrm{Fo}_3^{p+1} + \mathrm{Fo}_4^{p+1} + \frac{2\,h\,\Delta t}{\rho\, C\, \Delta x} + \frac{1}{2}\right) T_{m,n}^{p+1} = T_{m,n}^{p}$$

■ Left Corner with 1 Adiabatic and 1 Convection Surface

The existing form of the surface node backwards difference equation is:

$$h\,(T_\infty - T_{m,n}^{p+1})\,\Delta x + k\left(T_{m+1,n}^{p+1} - T_{m,n}^{p+1}\right) + k\left(T_{m,n-1}^{p+1} - T_{m,n}^{p+1}\right) = \rho\, C\, \frac{\Delta x^2}{2\,\Delta t}\,(T_{m,n}^{p+1} - T_{m,n}^{p})$$

Modifying for temperature dependent properties (add k_i):

$$h\,(T_\infty - T_{m,n}^{p+1})\,\Delta x + k_2^{p+1}\left(T_{m+1,n}^{p+1} - T_{m,n}^{p+1}\right) + k_3^{p+1}\left(T_{m,n-1}^{p+1} - T_{m,n}^{p+1}\right) = \rho\, C\, \frac{\Delta x^2}{2\,\Delta t}\,(T_{m,n}^{p+1} - T_{m,n}^{p})$$

Divide by $\rho\, C\, \frac{\Delta x^2}{2\,\Delta t}$ and assume the Fo_i convention:

$$-\frac{2\,h\,\Delta t}{\rho\, C\, \Delta x}\,(T_\infty - T_{m,n}^{p+1}) - 2\,\mathrm{Fo}_2^{p+1}\left(T_{m+1,n}^{p+1} - T_{m,n}^{p+1}\right) - 2\,\mathrm{Fo}_3^{p+1}\left(T_{m,n-1}^{p+1} - T_{m,n}^{p+1}\right) + T_{m,n}^{p+1} = T_{m,n}^{p}$$

$$-2\left(\mathrm{Fo}_2^{p+1}\, T_{m+1,n}^{p+1} + \mathrm{Fo}_3^{p+1}\, T_{m,n-1}^{p+1} + \frac{h\,\Delta t}{\rho\, C\, \Delta x}\, T_\infty\right) + 2\left(\mathrm{Fo}_2^{p+1} + \mathrm{Fo}_3^{p+1} + \frac{h\,\Delta t}{\rho\, C\, \Delta x} + \frac{1}{2}\right) T_{m,n}^{p+1} = T_{m,n}^{p}$$

Reference

[1] J. Barksdale. *Titanium: Its Occurrence, Chemistry, and Technology*, 2nd ed. (Ronald Press Company, New York, 1966) p. 3.

[2] Dunnington, E. P. Am. J. Sci. v. 42. p. 491 (1892).

[3] J. Barksdale, *ibid*. pp. 16-7.

[4] E.W. Collings. *The Physical Metallurgy of Titanium Alloys*. (ASM International, Materials Park, OH, 1984)

[5] E.W. Collings, in *Materials Properties Handbook: Titanium Alloys*, edited by R. Boyer, G. Welsch, and E.W. Collings. (ASM International, Materials Park, OH, 1994) pp. 3-122.

[6] C.R. Brooks. *Heat Treatment, Structure and Properties of Nonferrous Alloys*. (ASM International, Materials Park OH, 1982). pp. 329-87.

[7] W.F. Smith. *Structure and Properties of Engineering Alloys*. (McGraw-Hill, New York, 1993), pp.433-486.

[8] S. Lapman, in *ASM Handbook Volume 2, Properties and Selection: Nonferrous Alloys and Special-Purpose Materials*. (ASM International, Materials Park, OH, 1990) pp. 592-633.

[9] C. Hammond and J. Nutting, "Physical Metallurgy of Superalloys and Titanium Alloys," Metal Science, **11**, pp. 474-490 (1977).

[10] E.W. Collings. *The Physical Metallurgy of Titanium Alloys*, *ibid*. p. 2.

[11] W.F. Smith. *Structure and Properties of Engineering Alloys*, *ibid*. pp.440-4.

[12] E.W. Collings, *Materials Properties Handbook: Titanium Alloys*, *ibid*. pp. 5-6.

[13] E.W. Collings, *Materials Properties Handbook: Titanium Alloys*, *ibid*. p.9.

[14] E.K. Molchanova. *Phase Diagrams of Titanium Alloys* [Translation of *Atlas Diagram Sostoyaniya Titanovyk Splavov*], (Israel Program for Scientific Translations, Jerusalem, 1965).

[15] H.M. Flower, Materials Science and Technology, **6** (11), pp. 1082-1092 (1990)

[16] E.W. Collings, *Materials Properties Handbook: Titanium Alloys*, *ibid*. p.10.

[17] T. Nishimura, T. Mizoguchi, and Y. Itoh. "Titanium Materials for Cryogenic Service," *Kobe Steel Engineering Reports*. **34**, pp. 63-6 (1984).

[18] R. Boyer, G. Welsch, and E.W. Collings, eds. *Materials Properties Handbook: Titanium Alloys*, (ASM International, Materials Park, OH, 1994).

[19] W.F. Smith, *ibid*. pp. 445-9.

[20] E.W. Collings. *The Physical Metallurgy of Titanium Alloys*, *ibid*. pp. 132-3.

[21] M.K. McQuillan, "Phase Transformations in Titanium and its Alloys," Metallurgical Reviews, **8** pp. 41-104, 1963.

[22] M.J. Blackburn, "Some Aspects of Phase Transformations in Titanium Alloys," in *The Science, Technology and Application of Titanium*, edited by R.I. Jaffee, N.E. Promisel, (Pergamon, New York, 1970) pp. 633-43.

[23] J.C. Williams, "Critical Review – Kinetics and Phase Transformations," in *Titanium Science and Technology*, Vol. 3, edited by R.I. Jaffee and H.M. Burte, (Plenum, New York, 1973) pp. 1433-94.

[24] J.C. Williams, "Precipitation in Titanium-Base Alloys," in Precipitation Processes In Solids, edited by K.C. Russell and H.I. Aaronson, (The Metallurgical Society of AIME, Warrendale, PA, 1978), pp. 191-221.

[25] J.C. Williams, "Phase Transformations in Ti Alloys – A Review of Recent Developments," in *Titanium and Titanium Alloys: Scientific and Technological Aspects*, edited by J.C. Williams and A.F. Belov (Plenum, New York, 1982) pp. 1477-98.

[26] Y. Murakami, "Critical Review: Phase Transformation and Heat Treatment," Titanium '80 Science and Technology, edited by H. Kimura and O. Izumi (The Metallurgical Society of AIME, New York, 1980) pp.153-67.

[27] G. Welsch and R. Boyer, "Technical Note 1: Metallography and Microstructure," in *Materials Properties Handbook: Titanium Alloys*, edited by R. Boyer, G. Welsch, and E.W. Collings. (ASM International, Materials Park, OH, 1994) pp. 1051-1060.

[28] W.A. Reinsch, "Terminology for Titanium Microstructures," Metal Progress, February 1982, pp. 51-3; reprinted in *Titanium and Titanium Alloys*, edited by M.J. Donachie (American Society for Metals, Materials Park, OH, 1982) pp. 47-9.

[29] D. Eylon, "Faceted Fracture in Beta Annealed Titanium Alloys," Metallurgical Transactions **10A**, pp. 311-7, 1979.

[30] W.G. Burgers, "On the Process of Transition of the Cubic-Body-Centered Modification Into the Hexagonal Close-Packed Modification of Zirconium," Physica, **1** p. 651-86, 1934.

[31] J.C. Chesnutt, C.G. Rhodes, and J.C. Williams, "Relationship Between Mechanical Properties, Microstructure, and Fracture Topography in α+β Titanium Alloys," *Fractography—Microscopic Cracking Processes, STP No. 600*, (American Society for Testing and Materials), pp. 99-138 (1976); reprinted in *Titanium and Titanium Alloys*, edited by M.J. Donachie (American Society for Metals, Materials Park, OH, 1982) pp. 100-39.

[32] D. Shechtman and D. Eylon, "On the Unstable Shear in Fatigued β-Annealed Ti-11 and IMI-685 Alloys," Met. Trans. A, **9A**, pp. 1018-20, 1978.

[33] G.R. Yoder and D. Eylon, "On the Effect of Colony Size on Fatigue Crack Growth in Widmanstätten Structure α+β Alloys," Met. Trans. A, **10A**, pp. 1808-10, 1979.

[34] M.J. Blackburn, "The Ordering Transformation in Titanium:Aluminum Alloys Containing up to 25 at. Pct. Aluminum," Trans. of the Metallurgical Society of AIME, **239** (August), pp. 1200-8, 1967.

[35] E.W. Collings, *Materials Properties Handbook: Titanium Alloys*, *ibid*. p.27.

[36] P.A. Blenkinsop, W.J. Evans, and H.M. Flowers, editors, "Titanium `95: Science and Technology," Proceedings of the 8th World Conference on Titanium, (Institute of Materials, London, 1996).

[37] P. Gaunt and J.W. Christian, "The Crystallography of the β-α Transformation in Zirconiumand in Two Titanium-Molybdenum Alloys," Acta Metallurgica, **7**, pp. 534-43, 1959.

[38] C. Hammond and P.M. Kelly, "," Acta Metallurgica, **17** pp.869-, 1969.

[39] J.C. Williams, B.S. Hickman, and H.L. Marcus, "The Effect of Omega Phase on Mechanical Properties of Titanium Alloys," Metallurgical Transactions, **2**(7) pp. 1913-9, 1971.

[40] B.S. Hickman, "The Formation of Omega Phase in Titanium and Zirconium Alloys: A Review," Journal of Materials Science **4**, pp. 554-63, 1969.

[41] E.W. Collings. *The Physical Metallurgy of Titanium Alloys*, *ibid*. pp. 75-85.

[42] M.J. Blackburn and J.C. Williams, "Phase Transformations in Ti-Mo and Ti-V," Transactions of TMS-AIME, **242**, pp. 2461-9, 1968.

[43] Y.A. Bagariatskii, G.I. Nosova, T.V. Tagunova, "Factors in the Formation of Metastable Phases in Titanium-Base Alloys," Soviet Physics Doklady, **3**, pp. 1014-8, 1959.

[44] B.S. Hickman, "Omega Phase Precipitation in Alloys of Titanium with Transition Metals," Transactions of TMS-AIME, **245**, pp. 1329-36, 1969.

[45] D. De Fontaine, N.E. Paton, and J.C. Williams, "The Omega Phase Transformation in Titanium Alloys as an Example of A Displaccement Controlled Reaction," Acta Metallurgica, **19**, pp. 1153-62, 1971.

[46] C.G. Rhodes and J.C. Williams, "Observations of an Interface Phase in the α/β Boundaries in Titanium Alloys," Met. Trans. A, **6A**, pp. 1670-1, 1975.

[47] C.G. Rhodes and N.E. Paton, "The Effect of Heat Treatment on the Nature of the α/β Interface Layer in α+β Titanium Alloys," in *Titanium and Titanium Alloys: Scientific and technological Aspects*, edited by J.C. Williams and A.F. Belov, (ASM/Plenum, 1982) pp. 1437-50.

[48] D. Banerjee and V.S. Arunachalam, "On the α/β Interface Phase in Ti Alloys," Acta Metallurgica, **29**, pp. 1685-94, 1981.

[49] D. Banerjee and J.C. Williams, "The Effect of Foil Preparation Technique on Interface Phase Formation in Ti Alloys," Scripta Metallurgica **17** pp. 1125-8, 1983.

[50] D. Banerjee, C.G. Rhodes, J.C. Williams, "On the Nature of the α/β interfaces in Titanium Alloys," in Titanium Science and Technology, Proceedings of the 5th International Conference on Titanium, edited by G. Lütjering, U. Zwicker, and W. Bunk (Duetsche Gesellschaft für Metallkunde E.V., Germany, 1985), pp. 1597-1604.

[51] D. Banerjee, "A Resolution of the Interface Phase Problem in Titanium Alloys," Acta Metall., **36**(1), pp. 125-41, 1988.

[52] C.G. Rhodes and J.C. Williams, "The Precipitation of α-Phase in Metastable β-Phase Ti Alloys," Metallurgical Transactions, **6A**, pp. 2103-14, 1975.

[53] G.H. Isaac and C. Hammond, "The Formation of Type 2α Phase in Ti-3Al-8V-6Cr-4Zr-4Mo," in Titanium Science and Technology, Proceedings of the 5th International Conference on Titanium, edited by G. Lütjering, U. Zwicker, and W. Bunk (Duetsche Gesellschaft für Metallkunde E.V., Germany, 1985), pp. 1605-12.

[54] G. Lütjering, "Influence of Processing on Microstructure and Mechanical Properties of (α+β) Titanium Alloys," Materials Science and Engineering A, 243, pp. 32-45, 1998.

[55] G. Lütjering, J. Albrecht, and O.M. Ivasishin, "Microstructure and Mechanical Properties of Conventional Titanium Alloys," in Microstructure/Property Relationships in Titanium Alloys, eds. S. Ankem, and J. A. Hall, (The Minerals, Metals & Materials Society, Warrendale, PA, 1994). pp. 65-74

[56] H. Margolin, P.A. Farrar, M.A. Greenfield, "Thermo-Mechanical Strengthening of High Strength Titanium Alloys," in The Science Technology and Application of Titanium, eds. R.I. Jaffee and N.E. Promisel (Pergamon, NY, 1970) pp. 795-808.

[57] M.A. Greenfield, N. Kuhlken, and H. Margolin, "Fracture Stress and Microstructure of an Alpha-Beta Titanium Alloy," Metallurgical Transactions, **2**(2) pp. 610-2, 1971.

[58] G. Lütjering, A. Gysler, and L. Wagner, "Crack Propagation in Ti-Alloys," in Proceedings of the Sixth World Conference on Titanium, eds. P. Lacombe, R. Tricot, and G. Béranger, (Les Editions de Physique, Paris, 1989), pp. 71-80. 1988.

[59] N.D.R. Goddard, H.M. Flower, and M. Cope, in Proceedings of the Sixth World Conference on Titanium, eds. P. Lacombe, R. Tricot, and G. Béranger, (Les Editions de Physique, Paris, 1989), pp. 2323-38

[60] *Solid Freeform Fabrication Symposia* (University of Texas at Austin), 1990-2001.

[61] P.F. Jacobs, Stereolithography and other RP&M Technologies (Society of Manufacturing Engineers, Dearborn Michigan, 1996)

[62] J.J. Beaman, J.W. Barlow, D.L. Bourell, R.H. Crawford, H.L. Marcus, and K.P. McAlea, Solid Freeform Fabrication: A New Direction in Manufacturing, (Kluwer, Boston, 1997).

[63] D.T. Pham and S.S. Dimov, Rapid Manufacturing: The Technologies and Applications of Rapid Prototyping and Rapid Tooling (Springer, London, 2001).

[64] J. Brooks, C. Robino, T. Headly, S. Goods, and M. Griffith, "Microstructure and Property Optimization of LENS Deposited H13 Tool Steel," in Solid Freeform Fabrication Symposium, eds. D. Bourell, J. Beaman, R. Crawford, H. Marcus, and J. Barlow, (University of Texas, Austin, TX, 1999) pp. 375-82.

[65] K.P. Cooper, "Building Components by Laser Additive Processing," JOM, Sept. 2001, p. 29.

[66] F.G. Arcella, D.H. Abbott, and M.A. House, "Rapid Laser Forming of Titanium Structures," in Proceedings of the Powder Metallurgy World Conference and Exposition, (MPIF, Princeton, NJ, 1998) pp.

[67] F.G. Arcella, D.H. Abbott, and M.A. House, "Titanium Alloy Structures for Airframe Application, by the Laser Forming Process," AIAA pp. 1-10, 2000.

[68] F.G. Arcella and F.H. Froes, "Producing Titanium Aerospace Components from Powder Using Laser Forming," JOM, **52**(5), pp. 28-30, 2000.

[69] AeroMet Corporation website: http://www.aerometcorp.com

[70] J. Laeng, J.G. Stewart, and F.W. Liou, "Laser Metal Forming Processes for Rapid Prototyping - A Review," International Journal of Production Research, **38**(16), pp. 3973-96, 2000.

[71] G.K. Lewis and E. Schlienger, "Practical Considerations and Capabilities for Laser Assisted Direct Metal Deposition," Materials and Design, **21**, pp. 417-23, 2000.

[72] W.M. Steen, Laser Material Processing, 2nd Ed. (Springer, London, 1998).

[73] W.M Steen, *ibid* pp. 11-20.

[74] K.S. Krane, Modern Physics, 2nd Ed. (Wiley, New York, 1996), pp. 257-61.

[75] V.M. Weerasinghe and W.M. Steen, "Laser Cladding with Pneumatic Powder Delivery," Applied Laser Tooling, pp. 183-211, 1987.

[76] W.M. Steen, *ibid* p. 68.

[77] M.L. Griffith, M.E. Schlienger, L.D. Harwell, M.S. Oliver, M.D. Baldwin. M.T. Ensz, M. Essien, J. Brooks, C.V. Robino, J.E. Smugeresky, W.H. Hofmeister, M.J. Wert, and D.V. Nelson. "Understanding the Thermal Behavior in the LENS Process," Materials and Design, **20**, pp. 107-113, 1999.

[78] W. Hofmeister, M. Wert, J. Smugeresky, J.A. Philliber, M. Griffith, and M. Ensz, "Investigating Solidification with the Laser Engineered Net Shaping (LENS™) Process," JOM-e (JOM **51**(7) 1999), http://www.tms.org/pubs/journals/JOM/9907/Hofmeister/Hofmeister-9907.html.

[79] W.H. Hofmeister, M.L. Griffith, M.T.Ensz, and J.E. Smugeresky, "Solidification in Direct Metal Deposition by LENS Processing," JOM, **53**(9), pp. 30-34, 2001.

[80] M. N. Özişik, Finite Difference Methods in Heat Transfer, (CRC, Ann Arbor, 1994).

[81] C. D. Desai and J. F. Abel, Introduction to the Finite Element Method, (Van Nostrand Reinhold, New York, 1972).

[82] R.W. Lewis, K. Morgan, H.R. Thomas and K.N. Seetharamu, The Finite Element Method in Heat Transfer Analysis, (Wiley, New York, 1996).

[83] G.E. Forsythe and W.R. Wasow, Finite Difference Methods for Partial Differential Equations, 4th Printing (Wiley, New York, 1967). *Referenced in 80, page 2*.

[84] R.C. Batra, *Class Notes:* ESM 5734: Introduction to the Finite Element Method, (University Printing Services, Virginia Tech, 2000) p. 88.

[85] F.P. Incopera and D.P. DeWitt, Introduction to Heat Transfer, 3rd Ed. (Wiley, Hew York, 1996).

[86] M. N. Özişik, Heat Conduction, 2nd Ed. (Wiley, New York, 1993).

[87] V. Voller and M. Cross, "Accurate Solutions of Moving Boundary Problems Using the Enthalpy Method," International Journal of Heat and Mass Transfer, **24**, pp. 545-56, 1981.

[88] E. Kreyszig, Advanced Engineering Mathematics, 7th Ed. (Wiley, New York, 1993), p. 929.

[89] F.G. Arcella, E.J. Whitney, M.A. House, P.H. Cohen, and H.B. Bomberger, "Materials Characterization of LaserCast Titanium," Advances in Powder Metallurgy and Particulate Materials – 1996. eds. T.M. Cadle and K.S. Narasimhan. Vol. 4, Part 15. (Metal Powder Industries Federation, Princeton, NJ, 1996). pp. 151 -65.

[90] J.T. Schriempf, E.J. Whitney, H.B. Bomberger, and F.G. Arcella, "Properties of Some Laser Clad and Laser Formed Materials," Advances in Powder Metallurgy and Particulate Materials – 1997. eds. R.A. McKotch and R. Webb. Vol. 3, Part 21. (Metal Powder Industries Federation, Princeton, NJ, 1997). pp. 51-9.

[91] P.A. Kobryn and S.L. Semiatin, "Laser Forming of Ti-6Al-4V: Research Overview," Solid Freeform Fabrication Proceedings, eds. D. Bourell, J. Beaman, R. Crawford, H. Marcus, and J. Barlow, (University of Texas, Austin, TX, 2000) pp. 58-65.

[92] P.A. Kobryn, E.H. Moore, and S.L. Semiatin, "The Effect of Laser Power and Traverse Speed on Microstructure, Porosity, and Build Height in Laser Deposited Ti-6Al-4V," Scripta Materialia, **43** pp. 299-305, 2000.

[93] P.A. Kobryn and S.L. Semiatin, "The Laser Additive Manufacture of Ti-6Al-4V," JOM **53**(9) pp. 40-2, 2001.

[94] D.M. Keicher, J.A. Romero, C.L. Atwood, J.E. Smugeresky, M.L. Griffith, F.P. Jeantette, L.D. Harwell, and D.L. Greene, "Free Form Fabrication Using the Laser Engineered Net Shaping (LENS™) Process," Advances in Powder Metallurgy and Particulate Materials – 1996. eds. T.M. Cadle and K.S. Narasimhan. Vol. 4, Part 15. (Metal Powder Industries Federation, Princeton, NJ, 1996). pp. 119-27.

[95] J.E. Smugeresky, D.M. Keicher, J.A. Romero, M.L. Griffith, and L.D. Harwell, "Laser Engineered Net Shaping (LENS™) Process: Optimization of Surface Finish and Microstructural Properties," Advances in Powder Metallurgy and Particulate Materials – 1997. eds. R.A. McKotch and R. Webb. Vol. 3, Part 21. (Metal Powder Industries Federation, Princeton, NJ, 1997). pp. 33-42.

[96] M.L. Griffith, M.T. Ensz, J.D. Puskar, C.V. Robino, J.A. Brooks, J.A. Philliber, J.E. Smugeresky, and W.H. Hofmeister, "Understanding the Microstructure and Properties of Components Fabricated by Laser Engineered Net Shaping (LENS)," Solid Freeform and Additive Fabrication - 2000, MRS Symposium Proc. **625**, eds. S.C. Danforth, D. Dimos, and F.B. Prinz, (MRS, Warrendale PA, 2000) pp. 9-20.

[97] A. Vasinota, J. Beuth, M. Griffith, "Process Maps for Laser Deposition of Thin Walled Structures," Solid Freeform Fabrication Proceedings, eds. D. Bourell, J. Beaman, R. Crawford, H. Marcus, and J. Barlow, (University of Texas, Austin, TX, 1999) pp. 383-91.

[98] J. Beuth and N. Klingbeil, "The Role of Process Variables in Laser-Based Direct Metal Solid Freeform Fabrication," JOM **53**(9) pp. 36-9, 2001.

[99] *Mathematica v*. 4.1.0.0. http://www.wolfram.com Copyright 1988-2000 Wolfram Research, Inc.

[100] K.E. Easterling, Introduction to the Physical Metallurgy of Welding, 1st ed. (Butterworths, Boston, 1983), pp. 52-59.

[101] Boyer, Rodney R., in Metals Handbook: Metallography and Microstructures, 9th ed., vol.9, (American Society for Materials, Materials Park, OH, 1985) pp. 458-475.

[102] W.A. Baeslack III, Mat. Sci. Letters. **1**, pp. 229-231 (1982).

[103] A.T. D'Annessa, Weld. J. **45**, pp. 569s-576s (1966).

[104] G.J. Davies, J.G. Garland, Int. Metallurgical Reviews **20**, pp. 83-106 (1975).

[105] W.A. Baeslack III, D.W. Becker, and F.H. Froes, JOM **36** (5), pp. 46-58 (1984).

[106] W.A. Baeslack III, J.R. Davis, and C.E. Cross, in *ASM Handbook: Welding, Brazing, and Soldering* 9th ed., vol. 6, (ASM Intl., Materials Park, OH, 1993) pp. 507-523.

[107] Boyer, R.R. and G. Lutjering, "Heat Treatment of Titanium Alloys: Overview," in Advances in the Science and Technology of Titanium Alloy Processing, eds. I. Weiss, R. Srinivasan, P.J. Banja, D. Eylon, and S.L. Semiatin, (TMS, Warrendale, PA, 1997). pp. 349-67.

[108] J.W. Elmer, J. Wong, and T. Ressler, "Spatially Resoved X-Ray Diffraction Phase Mapping and αβα Transformation Kinetics in the Heat Affected Zone of Commercially Pure Titanium Arc Welds," Met. Mat. Trans A. **29A**(11) pp. 2761-73. (1998).

Vita

The author was born on September 12, 1977 in Baltimore, Maryland. He was raised in Perry Hall, a suburb of Baltimore. He attended Perry Hall High School, where he was a member and captain of the Cross Country and Track teams, and where he first stumbled across the field of Materials Science though a physics assignment on polymer matrix composite bicycle frames. Upon graduating high school in 1995, he traveled to Blacksburg, Virginia home of Virginia Tech to pursue a degree in Materials Science and Engineering. In the summers of 1997 and 1998, the author co-op'ed at NASA's Goddard Space Flight Center located in Greenbelt Maryland under the leadership of Michael Viens, Michael Barthelmy, and Brad Parker in the Materials Engineering Branch. It was through this experience that the author decided to attend graduate school. Upon graduating from Virginia Tech with a B.S. in Materials Science and Engineering, the author began working on the project documented here under Dr. Stephen Kampe. In the summer of 2000, the author married his then fiancée Nancy Chandale Hart. During his graduate studies, the author was the recipient of the Gary Clevinger Scholarship for his participation in departmental activities and role as the Materials Engineering Professional Societies (MEPS) president. He also wrote and presented papers at the Spring 2000 MRS, Fall 2001 MRS, and the MPIF 2002 International Conference on Metal Powder Deposition for Rapid Manufacturing Conferences.

Upon completion of the requirements for the Master's of Science degree in May 2002, the author will spend 6 weeks at Oak Ridge National Laboratories in Oak Ridge, Tennessee under the direction of Dr. S.S. Babu to further improve the thermal model that was described in this document and to work on computational modeling of Laser Surface Alloying. The author will apply the knowledge gained from this summer experience to his pursuit of a PhD in Materials Science and Engineering, to be completed within the next 2 years.